Characterization of the Electrical Properties of Polycrystalline Diamond Films

a Dissertation
Presented in Partial Fulfillment of the Requirements
For the Degree Doctor of Philosophy
in the Graduate School of the Ohio State University

By
Shulai Zhao, B.S., M.S.

1994

Characterization of the Electrical Properties of Polycrystalline Diamond Films

A Dissertation

Presented in Partial Fulfillment of the Requirements
for the Degree Doctor of Philosophy
in the Graduate School of The Ohio State University

By

Shulai Zhao, B.S., M.S.

◇ ◇ ◇ ◇ ◇ ◇ ◇ ◇ ◇ ◇ ◇

The Ohio State University

1994

Dissertation Committee:

Harris P. Kagan

Richard D. Kass

William F. Palmer

Approved By:

Harris Kagan

Advisor

Department of Physics

Abstract

The electrical properties of chemical vapor deposited (CVD) diamond films have been measured using charged particle-induced conductivity (CPIC). The collection distance, d, that a carrier drifts under the influence of an applied electric field was measured. In terms of the electrical properties, $d = \mu E \tau$ where μ is the carrier mobility and τ is the excess carrier lifetime. It was found that there is a constant gradient of collection distance along the film growth direction for the CVD diamond films produced by various techniques. Material characterizations were performed on the CVD diamond films. Visual observation, scanning electron microscopy, x-ray diffraction, Raman spectroscopy and photoluminescence were used to investigate the limitations of the electrical properties. Correlations were found between electrical property studies and the material characterizations. Crystal structural defects were found to be the factor limiting the electrical properties in CVD diamond.

For All my Beloved People

List of Tables

List of Figures

CHAPTER I

INTRODUCTION

1.1 CHARACTERISTICS OF DIAMOND

Diamond is composed of carbon atoms arranged tetrahedrally with a uniform spacing of 1.54 Å between nearest neighbors (Figure 1). The bonds between the carbon atoms in diamond are strong sp^3 σ-type bonds, which gives rise to many of its properties. As a result, its atomic number density is 1.77×10^{23} cm^{-3}, the highest of any material at normal pressure, and its mass density is 3.52 g cm^{-3}. The cohesive energy of diamond, the energy required to disassemble a solid into its constituent parts, is almost twice as large as that of silicon and germanium. This dense structure and strong bonding give diamond extreme hardness and wear resistance.

Diamond's thermoconductivity is extremely high, surpassing most metals and semiconductors. At room temperature, it is five times that of copper. It is able to dissipate its own heat or the heat generated elsewhere and can tolerate high temperature. It is one of the rare materials that naturally conducts heat yet electrically insulates.

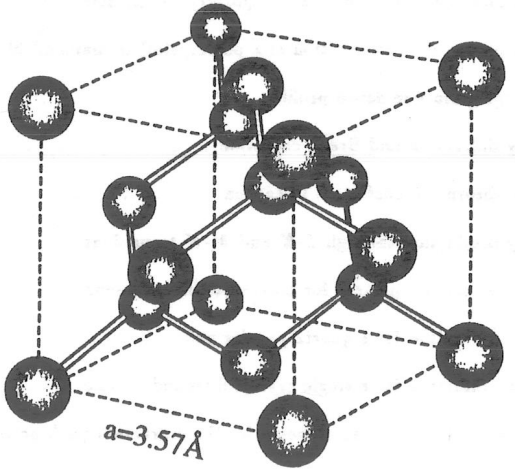

Figure 1: Crystallographic unit cell of a diamond crystal. The distance between the nearest carbon atoms is 1.54 Å. The lattice constant, a, is 3.57 Å.

Electronically, diamond is an insulator with the capability of being a semiconductor [1]. Like silicon, diamond has an *indirect band gap* [2]. The maximum of the valance band lies at the center of the Brillouin zone in reciprocal space (symmetry Γ); the lowest point of the conduction band is near the zone boundary in $\vec{k} = \langle 111 \rangle$ direction (symmetry X), where the band gap, E_g, is defined [1] (Figure 2). For diamond, $E_g = 5.470 \pm 0.005$ eV at 295°K [2] and the temperature dependence of E_g at 300°K is:

$$\frac{dE_g}{dT} = -(5.4 \pm 0.5) \times 10^{-5} \text{ eV } ^\circ\text{K}^{-1} \tag{1.1}$$

The direct edge E_g^{direct}, the energy difference of the valance band and the conduction band at the zone center (Γ), is approximately equal to 7.2 eV [2, 3] and its temperature dependence at 300°K is:

$$\frac{dE_g^{\text{direct}}}{dT} = -(6.3 \pm 1.8) \times 10^{-4} \text{ eV } ^\circ\text{K}^{-1} \tag{1.2}$$

A detailed band structure can be found in Ref. [3, 4].

Diamond has a large breakdown electric field ($\sim 10^7$ V cm^{-1}) and its saturation velocity is approximately 10^7 cm sec^{-1}. The electron and hole mobilities are 1800 cm^{2}V^{-1}sec^{-1} and 1200 cm^{2}V^{-1}sec^{-1} respectively. Table 1 lists some of the important material parameters of diamond and compares them with silicon and germanium. The different sections in Table 1 cover the atomic, crystal, thermal and electrical properties. Also included are the typical operating parameters for devices made of diamond, silicon and germanium. One interesting property of the devices constructed in diamond is that they attain the saturation properties of the material at a high electric field.

[1] The classification of diamond will be introduced in Appendix A

[2] In a direct band gap material, the lowest point of the conduction band in reciprocal space occurs at the same wave vector $\vec{k}$ as the highest point of the valance band; in an indirect band gap material, the lowest point of the conduction band does not occur at the same wave vector $\vec{k}$ as the highest point of the valance band.

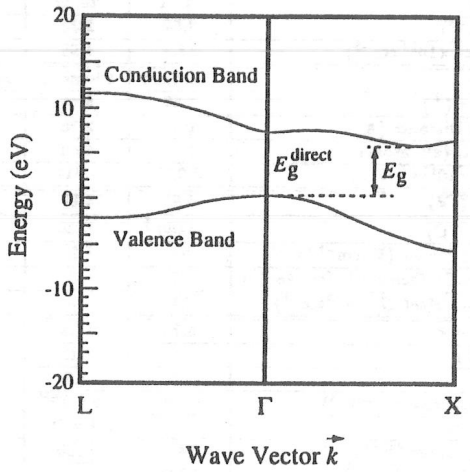

Figure 2: Energy band structure of diamond (R. A. Roberts and W. C. Walker, Physical Review, 161, 730, 1967).

Table 1: Basic Properties of Intrinsic Diamond, Silicon and Germanium at 300°K

Quantity	Diamond	Si	Ge
Atomic Number Z	6	14	32
Atomic Weight A	12.01	28.09	72.60
Density ρ_m (g cm^{-3})	3.52	2.33	5.33
Number of Atoms ($\times 10^{22}$ cm^{-3})	17.7	4.96	4.41
Crystal Structure	Diamond	Diamond	Diamond
Lattice Constant a (Å)	3.57	5.43	5.66
Nearest Neighbor Distance (Å)	1.54	2.35	2.45
Cohesive Energy U (eV/atom)	7.37	4.63	3.85
Compressibility ($\times 10^{11}$ m^{2}N^{-1})	0.226	1.012	1.29
Work Function ϕ (eV)	4.81	4.58	4.52
Melting Point T_m (°C)	$\sim$ 4100 †	1420	936
Thermal Conductivity σ_T (W cm^{-1} °K^{-1})	20	1.27	0.653
Electron Diffusion Coefficient D_n (cm^{2}sec^{-1})	47	38	90
Hole Diffusion Coefficient D_p (cm^{2}sec^{-1})	31	13	45
Dielectric Constant ϵ	5.70	11.9	16
Band Gap E_g (eV)	5.5	1.12	0.665
E_{pair} (eV)	13	3.6	3.0
Intrinsic Carrier Density n_i (cm^{-3})	$< 10^3$	1.5×10^{10}	2.4×10^{13}
Resistivity ρ_e (Ω cm)	$> 10^{13}$	2.3×10^5	47
Electron Mobility μ_n (cm^{2}V^{-1}sec^{-1})	1800	1350	3900
Hole Mobility μ_p (cm^{2}V^{-1}sec^{-1})	1200	480	1900
$E_{breakdown}$ (V cm^{-1})	10^7	3×10^5	$\sim 10^5$
$E_{saturation}$ (V cm^{-1})	$> 4 \times 10^4$	2×10^4	2×10^3
$v_{saturation}$ ($\times 10^7$ cm sec^{-1})	2.2	0.82	0.59
$E_{operation}$ (V cm^{-1})	4×10^4	10^3	10^3
$v_{operation}$ ($\times 10^7$ cm sec^{-1})	2.0	0.2	0.3

† Graphitisation occurs at 700°C in present of oxygen.

1.2 Electrical Properties of Diamond

1.2.1 Electrical Conduction

When an electric field, $\vec{E}$, is applied across a material, charge carriers (free electrons with a density n) are accelerated. The charge carriers, however, constantly suffer *scattering* which reduces their velocity. In the scattering process, some of the energy obtained from the electric field is transferred to the solid. When the energy gained from the electric field is balanced by the energy lost in the scattering, the charge carrier drift velocity, $\vec{v}_d$, reaches a constant value.

The drift motion of charge carriers constitutes a current density $\vec{J}$. Figure 3 illustrates the movement of a sample column of charge carriers. At $t = 0$, the column occupies the space AB. If dx is the length of the column, it takes a time $dt = dx/v_d$ to move the entire column AB to a new position BC. The total number of carriers passing through B is $dN = nSdx$, where S is the cross-sectional area. Then the current density, J, is equal to:

$$J = \frac{dQ}{Sdt} = -\frac{edN}{Sdt} = -env_d$$

or

$$\vec{J} = -ne\vec{v}_d \tag{1.3}$$

1.2.2 Carrier Mobility

The relationship between carrier drift velocity $\vec{v}_d$ and the electric field $\vec{E}$ can be written as:

$$\vec{v}_d = -\mu(\vec{E})\vec{E} \tag{1.4}$$

where $\mu(\vec{E})$ is defined as *carrier mobility*. The mobility μ is a tensor in general. If a charge carrier is moving in an isotropic material, μ is reduced to a scalar.

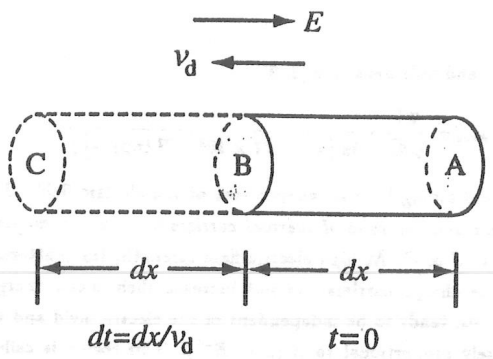

Figure 3: The motion of electrons driven by an electric field $\vec{E}$. At time $t = 0$, the column of electrons occupies the space AB. At time dt, the whole column drifts to a new space BC.

Using Ohm's law, $\vec{J} = \sigma\vec{E}$, the electrical conductivity, σ, can be expressed as a function of charge carrier density n and carrier mobility μ:

$$\sigma = ne\mu \tag{1.5}$$

Mobility is determined by the scattering processes in a crystal. If τ_R is the average charge carrier relaxation time between two successive scatters, then in the Drude model [5] for free electron conduction, carrier mobility is given by:

$$\mu = \frac{e\tau_R}{m^*} \tag{1.6}$$

where m^* is the effective mass [3].

In the Drude model, the carrier mobility is directly proportional to the scattering

[3]Instead of having been treated with a free electron mass m_e, experiencing both the periodic potential of the lattice and the external potential, a carrier can be treated as a "particle" with an effective mass m^*, experiencing the external potential only.

relaxation time [4]. In the other words, the more frequently the scattering occurs, the lower the carrier mobility. Usually, there are three major scattering mechanisms in a crystal. These are *phonon scattering*, *charged center scattering*, and *carrier-carrier scattering*.

Phonon scattering is the interaction of a charged carrier with the crystal as a whole. At finite temperature, the vibration of the atom around a particular lattice site distorts the periodic structure of the crystal. The energy of a lattice vibration is quantized. The quantization of the thermal vibration in a crystal is called a *phonon* [1]. The interaction between charge carriers and lattice vibrations can change the momentum and energy of the charge carriers. Two branches of phonons exist: an optical branch and an acoustical branch, depending upon the frequency range. Both the optical branch and the acoustical branch contribute to phonon-electron scattering.

Charge center scattering is the interaction of a charged carrier with imperfections in the lattice. These imperfections, such as chemical impurities, both substitutional and interstitial, and crystal structural defects, can alter the course of the charge carriers. These types of scattering are usually caused by Coulomb interactions between the charge carriers and charged centers such as ionized impurities, dangling bonds due to dislocations, and crystal boundaries.

Carrier-carrier scattering is the electric interaction between two carriers. When the

[4]A more complicated model should be used when the simple free electron approximation fails. The drift velocity of the carriers can be described by:

$$\vec{v}_d = \frac{\int \vec{v}_d(\vec{k}) f(\vec{k}) d^3\vec{k}}{\int f(\vec{k}) d^3\vec{k}} \tag{1.7}$$

where the integral is covered by all the possible values of $\vec{k}$; $\vec{k}$ is the wave vector associated with a carrier in Brillouin zone; $\vec{v}_d(\vec{k})$ is the group velocity of a single carrier with its wave vector center at $\vec{k}$ and $f(\vec{k})$ is the distribution function of the carrier wave vectors. $f(\vec{k})$ is determined by the Boltzmann equation [5]:

$$\left(\frac{\partial f}{\partial t}\right)_{\mathcal{E}} + \left(\frac{\partial f}{\partial t}\right)_{\text{scatt.}} = 0 \tag{1.8}$$

where all the possible scattering mechanisms are considered in the second term.

charge carrier population is higher than 10^{18} cm^{-3}, the scattering between carriers due to their Coulomb interaction becomes important. This effect is negligible at low carrier density.

Each scattering mechanism described above has a particular temperature dependent behavior. If μ_i represents the carrier mobility when only the i^{th} mechanism is present, the effective mobility, μ, can be expressed by the Mattiessen rule [1, 5]:

$$\frac{1}{\mu} = \sum_i \frac{1}{\mu_i} \tag{1.9}$$

The temperature dependence of the carrier mobility indicates which scattering process is dominant in a crystal.

A simple argument from the relaxation time approximation [5] may be used to deduce the temperature dependence of the mobility. For phonon scattering, the scattering rate, $\mathcal{R}$, is proportional to the phonon energy ($\sim k_B T$) and the density of states. If ϵ is the average kinetic energy of the charge carriers, the density of states, D, is proportional to $\sqrt{\epsilon} \sim \sqrt{k_B T}$ [1]. Then the temperature dependence of the relaxation time is given by:

$$\tau_R \propto \frac{1}{\mathcal{R}} \propto \frac{1}{\epsilon^{\frac{1}{2}} (k_B T)} \propto T^{-\frac{3}{2}} \tag{1.10}$$

Using Eq. 1.6, the temperature dependence of mobility due to phonon scattering behaves as:

$$\mu_{ps} \sim T^{-\frac{3}{2}} \tag{1.11}$$

For ionized impurity scattering, as the temperature is raised, the charge carriers have larger average kinetic energy, hence they are deflected less. Application of Rutherford's law [6] shows that τ_R is proportional to $\epsilon^{\frac{3}{2}}$ [7]. Since $\epsilon^{\frac{3}{2}} \sim (k_B T)^{\frac{3}{2}}$, the temperature dependence of mobility due to ionized impurity scattering has the form of:

$$\mu_{iis} \sim T^{+\frac{3}{2}} \tag{1.12}$$

For carrier-carrier scattering, the mobility, μ_{ccs}, is a function of temperature and

electron density n and hole density p [8, 9]:

$$\mu_{ccs} \propto \frac{T^{\frac{3}{2}}}{\sqrt{np}} \times \frac{1}{\ln\left\{1 + 1.77 \times 10^{8} \left[T^2 (np)^{-\frac{1}{3}}\right]\right\}} \tag{1.13}$$

At low electric field strength, μ is independent of the electric field. This region is called the *ohmic zone* or *zone of thermal carriers* because the current density follows Ohm's law: $J \propto E$. At high electric field strength, the scattering process dominates and the charge carriers can not increase their mean energy. Then, the drift velocity, v_d, tends to be independent of the electric field and the carrier mobility is inversely proportional to E ($\mu \propto E^{-1}$). This region is called *zone of hot carriers* and the drift velocity attained is called the *carrier saturation velocity*: $v_{\text{saturation}}$. Figure 4 illustrates the electric field dependence of electron drift velocity in diamond [10].

1.2.3 Charge Carrier Density

As a crystal is formed, the distinct electron atomic orbitals overlap causing a reorganization of the electron system. Instead of a set of isolated orbitals in the atomic state for individual atoms, energy bands are formed [11] (Figure 5).

The highest energy band occupied by electrons is called the *conduction band*; the energy band lower than the conduction band is called the *valance band*. The separation of highest point of the valance band and the lowest point of the conduction band is called *band gap* E_g. In metals, the conduction band is partially filled with electrons. This gives a metal its large conductivity. In semiconductors, the conduction band is empty at zero absolute temperature; at a finite temperature, some electrons in the valance band are excited thermally. They cross the band gap into the conduction band, leaving vacant orbitals or "holes" in the valance band. The charge carriers in semiconductors are the electrons in the conduction band and the holes in the valance band. In an intrinsic semiconductor [5], the electrons in the conduction band can only come from formerly occupied states in the valence

[5] An *intrinsic semiconductor* refers to a highly purified material.

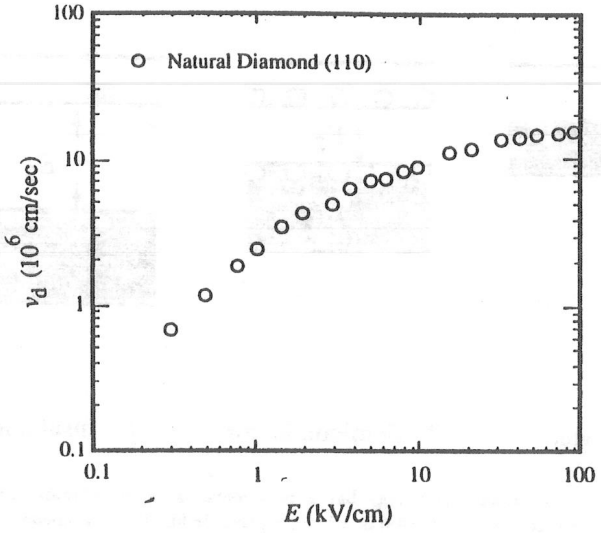

Figure 4: Electric field dependence of electron drift velocity in diamond (F. Nava *et al.* Solid State Communication, **33**, 475, 1980).

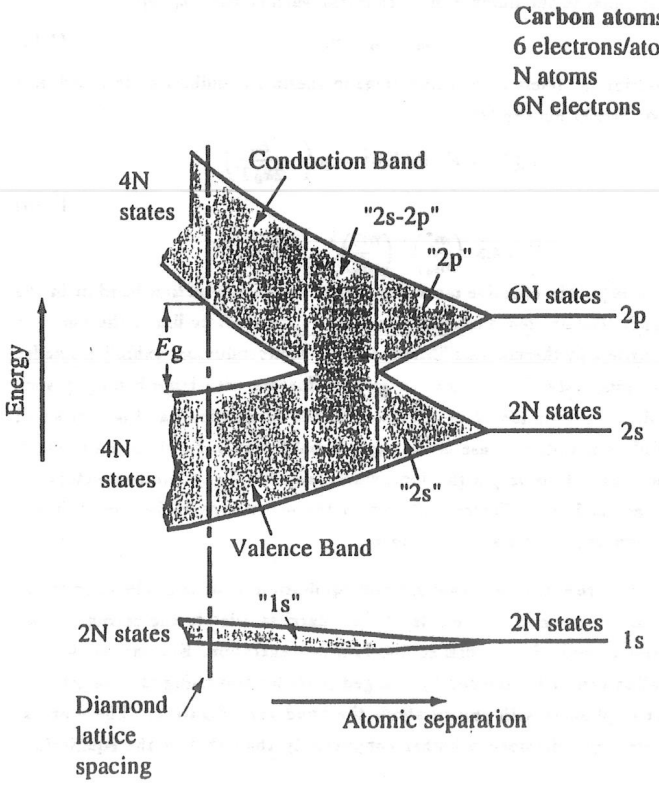

Figure 5: Formation of energy bands.

band. In the thermal equilibrium state, the number of electrons in the conduction band, n_0, is equal to the number of holes in the valence band p_0 [5]:

$$n_0 = p_0 \equiv n_i \tag{1.14}$$

where subscript "$_0$" refers to concentrations in thermal equilibrium state and n_i is the *intrinsic carrier density* [7]:

$$n_i(T) = K\,[T(^\circ\mathrm{K})]^{\frac{3}{2}}\,\exp\left(-\frac{E_g}{2k_BT}\right) \tag{1.15}$$

$$K = 4.8\left(\frac{m_c^*}{m_e}\right)^{\frac{3}{4}}\left(\frac{m_v^*}{m_e}\right)^{\frac{3}{4}} \times 10^{15}\ \mathrm{cm}^{-3}$$

where m_c^* or m_v^* is the effective mass of a carrier in the conduction band or in the valance band. The existence of energy gap in semiconductors limits the numbers of charge carriers at thermal equilibrium so that semiconductors exhibit a smaller electrical conductivity than metals. In semiconductors with large band gap such as diamond, the population of the electrons in the conduction band is very small in the equilibrium state because of the exponential factor in Eq. 1.15. As a result, the electric resistivity is very high. Sometimes, large band gap semiconductors are referred to as insulators. Figure 6 illustrates the occupancy of the energy bands for metals, semiconductors and insulators.

When electrons are excited externally, a non-equilibrium state is produced in which an *excess carrier concentration* exists. Excess carriers refer to the carriers whose concentration exceeds the thermal equilibrium concentration. External excess carrier generation can be introduced by charged particles traversing the material, or by incident of photons with energy above the band gap (Figure 7). These excess charge carriers give diamond a higher conductivity than that in the equilibrium state.

1.2.4 Excess Carrier Lifetime

In an intrinsic semiconductor, electrons and holes are constantly generated by thermal excitation of electrons from the valance band to the conduction band. In

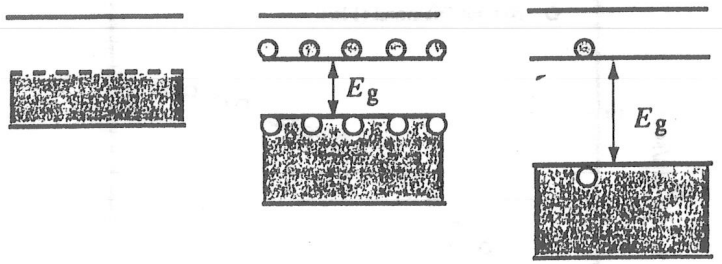

Figure 6: The occupancy of energy bands in a metal, a semiconductor and an insulator. In a metal (a), the conduction band is partially filled. In a semiconductor (b), the intrinsic carrier density is proportional to exp $(-\frac{E_g}{2k_BT})$ and there are a few occupied states (dots) in the conduction band and a few unoccupied states (open circles) in the valence band. In an insulator (c), the large band gap E_g and exponential factor exp $(-\frac{E_g}{2k_BT})$ cause the conduction band to be nearly empty.

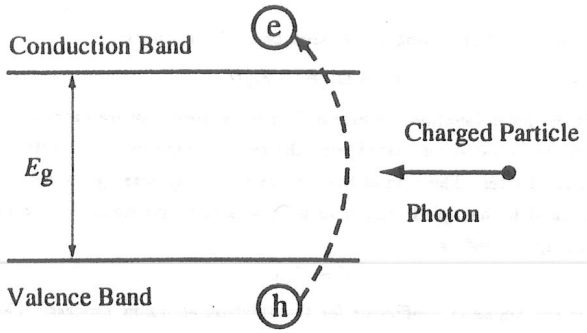

Figure 7: Charged particle-induced and photo-induced excess carrier generation: electrons are excited by energetic charged particles or photons with energy above the band gap. They jump into the conduction band and leave the holes in the valence band.

a state of thermal equilibrium, the generation process is counter-balanced by the recombination process in which electrons and holes annihilate each other. The recombination rate, R, is equal to the generation rate G.

$$R = G = r n_0 p_0 \tag{1.16}$$

where r is the recombination coefficient. In a non-equilibrium state, when an excess electron density (n) and an excess hole density (p) are present, the recombination rate becomes:

$$R = r(n_0 + n)(p_0 + p) \tag{1.17}$$

The thermal generation rate still keeps the form of $G = r n_0 p_0$. That $R > G$ indicates that the recombination process outweighs the generation process. More free charge carriers are lost through the recombination process than are gained through the generation process. The material relaxes towards the equilibrium state and the concentrations of charge carriers decay to their equilibrium values. The recombination processes give excess carriers a finite lifetime, τ, their average existence time.

Two basic processes are involved by which electrons and holes may recombine with each other. In the first process, electrons in the conduction band make direct transitions to the vacant states in the valance band. This is called the *intrinsic recombination process*. In the second process, electrons and holes recombine through intermediate states in the band gap. Those states, called *recombination centers*, exist because of structural defects or chemical impurities. This process is called the *extrinsic recombination process*. Because the two recombination processes are independent, using Mattiessen's rule, the effective lifetime is given by [1, 5]:

$$\frac{1}{\tau} = \frac{1}{\tau_{\text{intrinsic}}} + \frac{1}{\tau_{\text{extrinsic}}} \tag{1.18}$$

The lifetime $\tau_{\text{extrinsic}}$ in diamond results from recombination centers. It is observed to be of the order of $10^{-8} \sim 10^{-10}$ sec from transient photo-induced conductivity measurements [9]. Therefore, the band-to-band intrinsic lifetime, $\tau_{\text{intrinsic}}$, which ranges from $10^{-6} \sim 1$ sec [12, 14] does not play an important role in the recombination process of excess carriers when the material contains a considerable amount of defects and impurities.

A recombination center can be in either one of two possible states: occupied or unoccupied. In its unoccupied state, a recombination center is ready to receive an electron from either the conduction band (process 1 in Figure 8) or the valence band (process 4); in its occupied state, a recombination center can give its electron to either the conduction band (process 2) or the valence band (process 3).

For process 1, the rate of capturing an electron is proportional to (a) the concentration of the unoccupied recombination center states; and (b) the concentration of the occupied conduction band states. If N_t is the concentration of recombination centers, and n_t is the concentration of occupied centers, the concentration of unoccupied recombination centers is given by $(N_t - n_t)$. The occupied conduction band states can be expressed by the sum of the carrier concentrations at thermal equilibrium state and the excess carrier concentration:

$$\mathcal{N} = n_0 + n \tag{1.19}$$

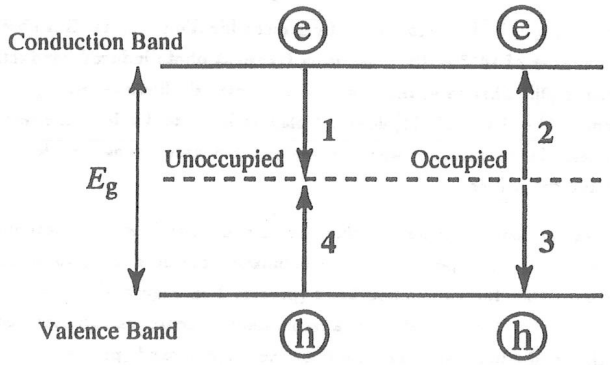

Figure 8: Extrinsic recombination processes through recombination centers. Electrons are captured from the conduction band (process 1) and the valence band (process 4) by unoccupied centers. Electrons are released to the conduction band (process 2) and the valence band (process 3) by occupied centers.

Therefore, the rate of capturing an electron can be written as:

$$U_1 = C_n(N_t - n_t)\mathcal{N} \tag{1.20}$$

where C_n is the recombination coefficient for the electron-capture process. The recombination coefficient is associated with the electron capture cross section which will be discussed later. The rate of the reverse process (releasing electrons to the conduction band by occupied centers in process 2 is proportional to the concentration of occupied centers n_t:

$$U_1' = R_n n_t \tag{1.21}$$

where R_n is the emission coefficient for the electron-emission process. Thus the net rate of capturing electrons from the conduction band is equal to:

$$-\frac{dn}{dt} = U_1 - U_1' = C_n(N_t - n_t)\mathcal{N} - R_n n_t \tag{1.22}$$

The minus sign indicates the carrier concentration is decreasing. In thermal equilibrium, $\mathcal{N} = n_0$ and $\frac{dn}{dt} = 0$. Thus:

$$R_n = C_n n_0 \left(\frac{N_t - n_t}{n_t}\right)_0 \tag{1.23}$$

When excess carriers are present, $\frac{dn}{dt}$ is no longer zero. Substituting the expression for R_n, we have:

$$-\frac{dn}{dt} = C_n[(N_t - n_t)\mathcal{N} - n_t n'] \tag{1.24}$$

where n' is defined as:

$$n' = n_0 \left(\frac{N_t - n_t}{n_t}\right)_0 \tag{1.25}$$

For a low level excitation, for example, $n \sim 10^{13}$ cm^{-3}, the number of capture sites is usually much larger than the number of excess carriers. Thus, the number of occupied sites is small, $N_t \gg n_t$. On the other hand, the density of excess carriers is much larger than the equilibrium intrinsic carrier density, $n \gg n_0$. Therefore, Eq. 1.24 reduces to:

$$\begin{aligned} \frac{dn}{dt} &\approx -C_n(N_t\mathcal{N} - n_t n') \\ &\approx -C_n N_t n \\ &= -\frac{n}{\tau_n} \end{aligned} \tag{1.26}$$

where $\tau_n = 1/C_n N_t$ is the excess electron lifetime.

A similar expression exists for the recombination of excess holes:

$$\frac{dp}{dt} = -\frac{p}{\tau_p} \tag{1.27}$$

where $\tau_p = 1/C_p N_t$ is the excess hole lifetime. These two quantities can be expressed in terms of capture cross sections σ_n and σ_p:

$$\tau_n = \frac{1}{N_t \sigma_n v_{th}} \tag{1.28}$$

$$\tau_p = \frac{1}{N_t \sigma_p v_{th}} \tag{1.29}$$

where $v_{th} = \sqrt{3k_B T/m^*}$ is the thermal velocity which is about 10^7 cm sec^{-1} at 300°K. The capture cross sections for electrons and holes determine the kinetics of the process.

1.2.5 Collection Distance

When an external excitation occurs, excess electron-hole pairs (e-h pairs) are produced. If an external electric field, $\vec{E}$, is applied, the excess carriers separate. The distance which the excess carriers are able to drift is determined by the carrier drift velocity v_d and the excess carrier lifetime τ. Since the charge collection process is of interest in the development of radiation detectors, the average drift distance is denoted as COLLECTION DISTANCE. The collection distance is defined as:

$$d = v_d \tau = \mu E \tau \tag{1.30}$$

Since there are two types of carriers, the collection distance is the average distance which the electron and hole depart under the electric field $\vec{E}$. Because electrons and holes have different effective masses (m_c^*, m_v^*) and exist in different energy bands, the values of electron mobility (μ_n) and hole mobility (μ_p) may be different. In addition, the electron lifetime (τ_n) and hole lifetime (τ_p) may not be equal. Therefore, the collection distance, d, is equal to:

$$\begin{aligned} d &= (\mu_n \tau_n + \mu_p \tau_p)\, E \\ &\equiv \mu E \tau \end{aligned} \tag{1.31}$$

where

$$\mu \equiv \frac{\mu_n \tau_n + \mu_p \tau_p}{\tau} \tag{1.32}$$

and τ is the mobility weighted lifetime.

1.2.6 Experimental Techniques

The collection distance may be determined by charged particle-induced conductivity (CPIC) and photo-induced conductivity (PIC) measurements. In both experiments, electric contacts are applied on the diamond by metallization. The motion of excess carriers under an electric field created by a voltage applied to the electric contacts produces a current pulse. The collected charge, $Q_{\text{collected}}$, can be measured by integrating the current pulse. The collection distance, d, can be derived from $Q_{\text{collected}}$. As a result, the product of carrier mobility and lifetime can be evaluated.

The configuration of the electric contacts is determined by the excitation source used to create the excess carriers. The excitation sources include energetic charged particles and photons with an energy above the band gap. The various structures are summarized below:

- ◇ Metal-Insulator-Metal Structure.

  Since charged particles such as high energy electrons from a radioactive source or accelerator test beam are able to fully traverse the diamond film,

a metal-insulator-metal (MIM) structure is used (Figure 9). The incident particle direction is nearly parallel to the electric field, the excitation occurs along the particle track throughout the diamond film. In this case, information about the bulk of the material can be obtained.

◇ Planar Contact Structure.

When the excitation source is a photon (ultra-violet, x-ray and γ-ray) or charged particle such as α particle, the penetration range in diamond is small [6]. The electron-hole pair generation takes place near the surface of the material. In this case, a planar contact configuration is used (Figure 9). Since the excitation region is just beneath the diamond surface, this method carries the information of the electrical properties near the surface.

The information from both measurements compliment each other. Using both measurements, the relationship between the properties in the bulk and the surface can be investigated. Also, the relationship between the drift perpendicular to the film surface and parallel to the surface can be compared.

1.3 Diamond Detectors

1.3.1 Chemical Vapor Deposition Technology

Chemical vapor deposition (CVD) technology has been used in the growth of most of the diamond films studied in this dissertation. In the CVD processes, a hydrocarbon gas, such as methane, is mixed with a large concentration of molecular hydrogen gas. The gas mixture is excited by a power source and the atomic state carbon atoms link together onto a substrate, forming σ-type bonds which lead to a diamond lattice and eventually a polycrystalline film. In various CVD processes, it is common [15] to start from a reactive gas phase which is composed of carbon and hydrogen. Oxygen is frequently added, either directly or as a part of the carbon carriers (CO or CO_2). The presence of oxygen can have a marked influence

[6] More details will be introduced in Chapter II.

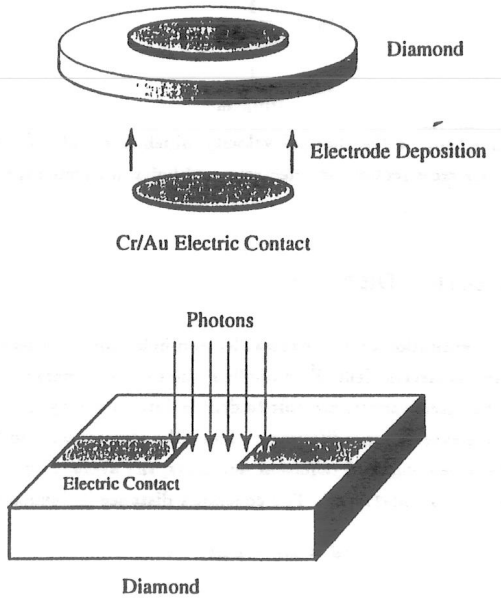

Figure 9: The upper diagram shows the diamond ionization chamber, two electric contacts on the surfaces are deposited. The lower diagram shows a diamond photo-detector, the shaded areas represent the electric contacts.

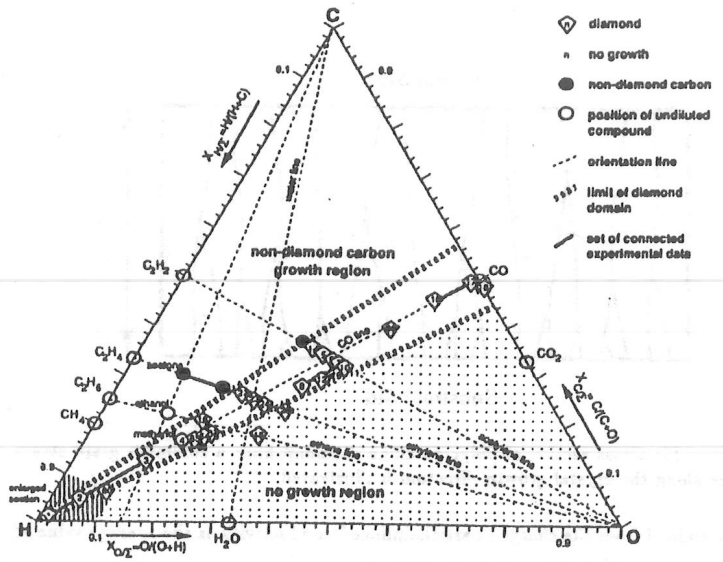

Figure 10: Atomic C-H-O diamond deposition phase diagram (P. K. Bachmann, D. Leers and H. Lydtin, Diamond and Related Materials, 1, 4, 1991).

on the deposition processes, as can the temperature of the CVD gas phase and substrate [15]. Successful diamond deposition is restricted to a well defined area within a C-H-O triangle phase diagram (Figure 10).

Natural diamond and man-made diamond have the same crystal lattice. However, the different production processes introduce different components of impurity concentration levels and different structural defect densities. These differences may likely result in different material properties, e.g. mechanical strength, thermal conductivity and electrical conductivity.

Although natural diamond is single crystal, it is far from perfect, containing high densities of impurities [7] and structural defects. For example, one impurity element common in natural diamond is nitrogen. Its concentration can be as large as 10^{18} cm^{-3}. As CVD diamond growth technology has matured, the quality of the polycrystalline diamonds has improved. It will be seen in the following chapters that some of the material properties of new CVD diamond films have already exceeded those of natural diamond.

1.3.2 An Application of Diamond Detectors

Because diamond has a high saturation velocity and a high breakdown electric field, a detector made of diamond can be operated at high electric field. Hence, high collection efficiency can be attained and fast operation can be achieved. In addition, the strong carbon bonds in diamond gives it excellent resistant to radiation damage. The other advantage of diamond based devices is the potential low cost of CVD diamond growth process.

One application of diamond detectors is in high rate, high radiation environments such as the Superconducting Super Collider (SSC) and the Large Hadron Collider (LHC) which require high performance detectors that can survive extreme environments. These facilities provide a unique opportunity for the discovery and investigation of a host of new phenomenon. Here the unique properties of diamond, when compared with silicon based devices, make diamond detectors extremely attractive.

[7] The major impurities in natural diamond are (1) nitrogen, up to 0.2% in type Ia diamond; (2) nickel, iron etc. up to 10% as inclusions in synthetic diamond; aluminium, up to 10 p.p.m. in natural diamond; boron, up to 0.25 p.p.m. in natural type IIb and 270 p.p.m. in specifically doped type IIb synthetic diamond; (3) up to twenty-five mineral species have been positively identified [16, 17].

1.4 Electrical and Material Characterizations

The work I have undertaken is to investigate the electrical properties of diamond films, to characterize the diamond films using material research experiments, and to seek the possible correlations between the electrical properties and the material characteristics.

1.4.1 Charged Particle-Induced Conductivity

To measure the collection distance, one of the electrical properties of diamond, charged particle-induced conductivity (CPIC) measurements were performed. Accelerator test beams and a radioactive sources, ^{90}Sr, were used. Different particle species with different energies were used in the CPIC experiments. Using the CPIC technique, the electric field dependence of collection distance of natural single crystal diamond and CVD polycrystalline diamond films was measured.

There are differences between single crystal and polycrystalline materials [8]. In natural diamond, due to its single crystal nature, the collection distance in the bulk is equal to the surface collection distance. This was demonstrated in our experiments. In polycrystalline diamond films, a columnar grain structure exists. Figure 11 illustrates the cross section of polycrystalline diamond film with a film thickness of L. In CVD diamond, the crystal quality was found to improve with film thickness along the growth direction. Because there is a gradient in the quality of polycrystalline diamond films, the electrical properties at the surface are no longer equal to those in the bulk. Charged particle-induced conductivity delivers information averaged over the bulk of the diamond films. These bulk measurements were associated with the results of surface measurements. From both experimental observations and theoretical analysis, it was found that the bulk collection distance,

[8] A crystal is a 3-dimensional pattern in which atoms generally assume orderly arrangement. On the contrary, an amorphous solid is of non-periodic disordered state. A polycrystalline solid is in between the two extremes: the orderly pattern of crystalline terminates at grain boundaries; the grain-grain structure extends to form the polycrystalline material.

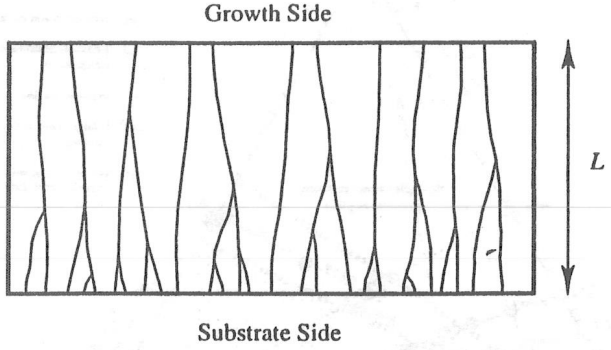

Figure 11: Cross section of polycrystalline diamond film: a columnar grain structure along the crystal growth direction is illustrated.

determined from the charged particle-induced conductivity, is the average value of the collection distances at the two surfaces.

Another problem exists in polycrystalline materials: grain boundaries. In a material with anisotropic grain boundaries, the drift parallel to the boundary may be different than the drift perpendicular to it. When the collection distance is much smaller than the grain size, excess carriers recombine before reaching the boundary. Thus, the boundaries have little the effect on carrier transport. However, when collection distance approaches the grain size, the anisotropic grain boundary conditions may yield a difference in the drift process in different directions. For polycrystalline diamond films, because of the columnar grain structure, few boundaries occur in the columnar direction. Thus, the grain boundaries have minimum influence on the collection distance measured by the CPIC technique. However, for the PIC measurement, when the collection distance is comparable to the lateral grain size, the effect of grain boundaries must be considered.

The electrical properties of diamond may also be limited by crystal imperfections in

the material. These crystal imperfections can be chemical impurities or structural defects. Material characterizations have been used to study the limitations of the electrical properties.

1.4.2 Material Characterizations

Scanning electron microscopy was used to study crystal structure, grain size, faceting and defects. The columnar polycrystalline grain structure was also examined. It was found that the average lateral grain size increases with film thickness. Also, the collection distance and the average grain size were compared.

X-ray diffraction measurements yield information about the lattice constant and crystal imperfections. From the diffraction peak positions, the diamond lattice constant of the polycrystalline films was determined. A deviation from a perfect diamond lattice due to crystal imperfections was observed. In addition, from the width of the diffraction peaks, the overall quality of the polycrystalline films was characterized. Correlations were found between the collection distance and the lattice constant and peak width.

Raman and photoluminescence provide information on impurities in diamonds. From Raman spectroscopy, graphite or amorphous state of carbon can be examined. A correlation between the collection distance and Raman spectrum width was also observed. As characterizations of film quality, the diamond Raman line width was found to be correlated with the x-ray diffraction peak width. Photoluminescence measurements were used to identify crystal defects and characterize polycrystalline diamond films.

From the material characterizations and their correlation with the electrical property studies, structural defects were found to be the major factor limiting the performance of a polycrystalline diamond detectors.

CHAPTER II

Theoretical Analysis

The purpose of this chapter is to describe the ionization and charge collection processes based on fundamental physical concepts and thorough mathematical approaches. An understanding of the ionization and charge collection processes is necessary to link the experimental results and theoretical analysis for charged particle-induced conductivity (CPIC) and photo-induced conductivity (PIC). It is also important to develop a method to characterize the radiation detectors using fundamental physical quantities such as carrier mobility and carrier lifetime.

The external excitation induced by charged particles or by photons can be classified into two categories: intrinsic or extrinsic excitation. Extrinsic behavior results when charge carriers are excited from impurity centers with energy levels within the band gap. Since the diamonds we studied are not doped, the number of carbon atoms is much larger than the number of impurity atoms. This implies that the extrinsic excitation is negligible. Intrinsic excitation is caused by a band-to-band transition where electrons are excited from the valance band to the conduction band leaving empty states in the valance band. Both the excess electrons and the excess holes contribute to the transient conductivity.

When a charged particle, such as an electron, traverses into a piece of semiconductor, electron-hole pairs (e-h pairs) are produced by the ionization process. Although the material remains electrically neutral, the conductivity of the material

increases. Similar to charged particle-induced conductivity, intrinsic photo-induced conductivity results when incident light or other suitable electromagnetic radiation has energy larger than the band gap E_g, generating electron-hole pairs and higher conductivity. To measure the transient conductivity, two metallic electric contacts are deposited on a diamond. A bias voltage is applied to the electric contacts to collect the charges generated by the external radiation.

2.1 Charge Ionization Process

When a non-equilibrium state is produced by an external excitation source, a bounded electron may absorb energy and become a free charge, leaving its parent atom ionized. This process is called *ionization*. The energy transferred is determined by energy and momentum conservation laws during the ionization process.

2.1.1 Charged Particle Excitation

As a high energy charged particle passes through a material, energy transfer occurs due to the Coulomb interaction between the charged particle and atomic electrons in the material. The orbital speed of the atomic electrons is approximately equal to αc, where $\alpha = 1/137$ and c is speed of light in vacuum. Thus, the bounded electrons can be treated as free compared with the incoming high energy particles with velocity ($v \sim c$). The Bethe-Bloch theory has been used to calculated the average energy loss in a material, $\frac{dE}{dx}$ (MeV cm^{2}g^{-1}). Based on energy and momentum conservation when radiative energy loss is negligible [18, 19]:

$$-\frac{dE}{dx} = 4\pi N_A r_e^2 m_e c^2 z^2 \frac{Z}{A}\frac{1}{\beta^2}\left[\ln\left(\frac{2m_e c^2\gamma^2\beta^2}{I}\right) - \beta^2 - \frac{\delta(\gamma)}{2}\right] \qquad (2.1)$$

where the minus sign represents energy loss; ze is the charge of incoming charged particle; N_A, Z and A are the atom density, the atomic number and atomic weight of the material; m_e and r_e are the electron mass and classical radius ($\frac{e^2}{m_e c^2}$), and $4\pi N_A r_e^2 m_e c^2 = 0.3071$ MeV cm^{2}g^{-1}; I is the ionization constant, approximately

equal to $16Z^{0.9}$ eV if $Z > 1$, which is measured to be $I = 78$ eV for diamond [20]; $\beta = v/c$; $\gamma = (1-\beta^2)^{-1/2}$ and $\delta(\gamma)$ is a correction for the density effect caused from the screening of incoming particle's electric field by atomic electrons. When $\gamma < 2$, $\delta(\gamma)$ is approximately equal to zero [20]. The energy loss per unit length, $\frac{d\mathcal{E}}{dx}$ (MeV cm^{-1}), can be written:

$$\frac{d\mathcal{E}}{dx}\,(\text{MeV cm}^{-1}) = \rho_m \frac{dE}{dx} \qquad (2.2)$$

where ρ_m is the mass density. In the low energy region, $\frac{dE}{dx}$ falls due to the $1/\beta^2$ factor; $\frac{dE}{dx}$ increases when the $\ln(\gamma^2)$ term dominates. Using $I = 78$ eV, Eq. 2.1 gives a minimum of energy loss in diamond $\frac{dE}{dx} = \left(\frac{dE}{dx}\right)_{MI} \approx 1.84$ MeV cm^{2}g^{-1} when $\beta \sim 0.957$. This region it is called *minimum ionization*.

Bremsstrahlung Effect

Particles passing through material are scattered and lose energy by collisions and undergo deceleration. It is known that charges which are accelerated emit electromagnetic radiation [21]. The radiation emitted during the collisions is called *Bremsstrahlung radiation* or *braking radiation*. The ratio of the energy loss due to radiation to the energy loss due to the Coulomb interaction is given approximately by [22]:

$$\frac{\left(\frac{dE}{dx}\right)_{rad}}{\left(\frac{dE}{dx}\right)_{Coulomb}} \approx \frac{Z E_i}{1600\, m_e c^2} \qquad (2.3)$$

where E_i is the incident electron energy. The energy at which the loss due to radiation equals to the loss caused by Coulomb interaction is called the *critical energy*:

$$E_{crit} = \frac{1600}{Z} m_e c^2 \qquad (2.4)$$

When $E_i \gg E_{crit}$, radiation is the dominating mechanism for energy loss; when $E_i \ll E_{crit}$, Coulomb interactions dominate. The critical energy for diamond is equal to $E_{crit} \approx 130$ MeV.

2.1.2 Energy Deposition along Particle Tracks

Some of the energy lost by a fast charged particle appears in fast secondary electrons or high energy photons which leave the vicinity of its track within times $\leq 10^{-15}$ sec [23]. For thin materials, the energy deposited near the track by the charged particle, called *restricted energy loss*, may be different from the total energy loss. When energy is carried off by the energetic secondary particles, the energy loss in a material which may be detected is given by [23]:

$$-\left(\frac{dE}{dx}\right)_{\leq E_{max}} = 4\pi N_A r_e^2 m_e c^2 z^2 \frac{Z}{A}\frac{1}{\beta^2}\left[\ln\left(\frac{\sqrt{2m_e c^2\gamma^2\beta^2 E_{max}}}{I}\right) - \frac{\beta^2}{2} - \frac{\delta(\gamma)}{2}\right] \quad (2.5)$$

where E_{max} is the cut-off energy above which the secondary particles escape the material. $E_{max} \approx 7.5$ keV which will be discussed in the following section.

2.1.3 Photon Excitation

When an electromagnetic wave propagates through a dielectric medium, transitions between atomic states occur. As a result of photon absorption, the intensity of the wave attenuates as it propagates. The electromagnetic field can be treated as a classical variable to obtain the solution of the complex dielectric constant $\tilde{\epsilon}(\omega) = n(\omega) + ik(\omega)$ from the Kramers-Kronig relations [5, 24]. The absorption of energy leads to a change of the light intensity — Lambert's law:

$$I(x) = I_0\, e^{-\gamma(\omega)x} \quad (2.6)$$

$$\gamma(\omega) = \frac{Kk(\omega)}{n^2}$$

where $1/\gamma$ is referred to the *absorption length*; x is the depth from the medium surface; ω is the light frequency; $K = \omega\sqrt{\mu\epsilon}/c$; μ and ϵ are the permeability and permittivity of the medium; I_0 is the normal incident intensity and n is the optical index. A full quantum mechanical theory for the induced transitions between two

energy levels leads to a similar result [24]. The absorption length is a function of photon frequency. For a photon energy of 6 eV, the absorption length in diamond is about $1 \sim 2$ μm [2, 25, 26]; for the unfiltered synchrotron spectrum (SSRL, see Table 2), the absorption length is about 0.2 μm [27]

The photon energy attenuation can be used to estimate the cut-off energy E_{max} for the restricted energy loss. When a charged particle traverses a material, some of the energy lost by this charged particle generates high energy photons and fast secondary electrons. If the material thickness is thin, some of those energetic secondary particles may escape from the material. Therefore, those secondary particles can not contribute to generate more excess electron-hole pairs. The photon escape can be described by the intensity attenuation [1]. The intensity after a thin film with a thickness, L, is attenuated by a factor of $\exp(-\gamma L)$. The absorption length is plotted as a function of photon energy in Figure 12 [28]. When the photon energy increases, the attenuation decreases and more photons will escape from the material. Thus, the cut-off energy, E_{max}, can be approximated as the energy above which the probability for the secondary to escape is less than 1/e. Setting $\gamma L = 1$, the absorption length, $1/\gamma$, is equal to 0.05 cm for a thickness $L = 500$ μm. Then the cut-off energy can be extrapolated from Figure 12: $E_{max} \approx 7.5$ keV.

2.1.4 Energy for Electron-Hole Generation

Incident radiation causes the generation of excess carriers (electron-hole pairs). The average energy to generate an electron-hole pair is called E_{pair}. High energy charged particles or photons with energy above the band gap can act as ionization sources.

[1] The e^+e^- pair generation cross section for high energy photons is equal to $\frac{7}{9}$ of that for high energy electrons [28]. Because the restricted energy loss is a weak function of E_{max} (Eq. 2.5), the difference of E_{max} caused by the different cross sections for photons and electrons can be neglected in the calculations of the restricted energy loss.

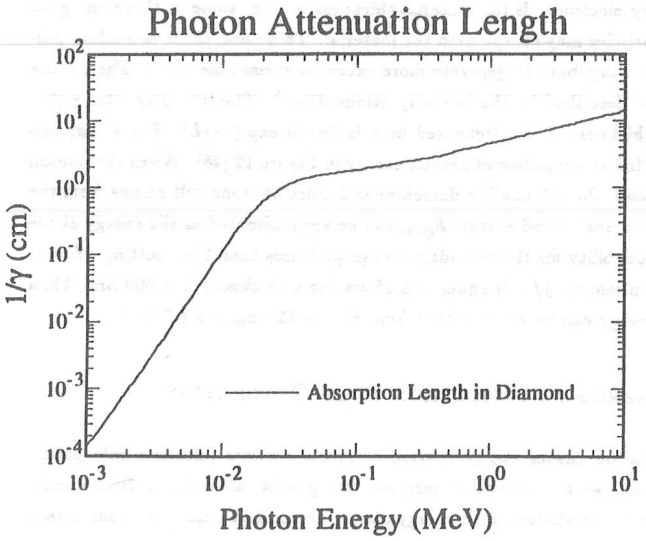

Figure 12: Photon absorption (*Particle Properties Data Booklet*, 121, 1990). The absorption length, $1/\gamma$, is plotted against photon energy for carbon atoms. The mass density of diamond is equal to $\rho_m = 3.52$ g cm^{-3}.

Charged Particle and X-ray Excitation

High energy charged particles can generate excess electrons and excess holes. For an excess carrier with a kinetic energy larger than the ionization threshold E_i, some of the energy is lost in generating additional electron-hole pairs until the end of the ionization process when the excess carrier has a kinetic energy less than E_i. In addition, some of the energy transfers to the lattice through Raman scattering. Shockley [29] proposed that the average energy required to generate an electron-hole pair is given by:

$$E_{pair} = E_i + 2E_f + rE_R \tag{2.7}$$

1. E_i is the energy absorbed in the generation of an electron-hole pair. In a simplified model, $E_i = E_g$.
2. E_f is the kinetic energy of each excess carrier after the ionization process. $E_f < E_i$. For electrons in the conduction band, in a simple parabolic model of the electron energy as a function of the electron momentum, E_f is given by [29]:

$$E_f = \frac{3}{5}E_i = \frac{3}{5}E_g \tag{2.8}$$

As a consequence, for charged particles, the average energy to generate an electron-hole pair in a semiconductor is equal to:

$$E_{pair} = 2.2E_g + rE_R \tag{2.9}$$

An x-ray photon with energy from 500 eV to 3000 eV has a wave number greater than 10^7 cm^{-1}, comparable with the size of Brillouin zone ($\sim 10^8$ cm^{-1}) [1]. Since photon wave number is proportional to the photon momentum, this large momenta make it possible to excite an excess electron anywhere in the Brillouin zone. Similar to the case for charged particles, for the x-ray excitation, E_{pair} is equal to:

$$E_{pair} = 2.2E_g + rE_R \tag{2.10}$$

3. E_R is the energy transferred to lattice through Raman scattering. Because the Raman shift ($\Delta\nu$) corresponding to the optical phonon in diamond is equal to 1333 cm^{-1}, E_R can be calculated to be: $E_R = hc\Delta\nu = 0.165$ eV.

4. r is equal to L_i/L_R, which is the ratio of the carrier mean free path (L_i) and the mean free path for the Raman scattering (L_R). The quantity, r, represents the average number of phonons per ionization. Using the Drude model, the carrier mean free path can be estimated as $L_i \approx 500$ Å. The mean free path for the Raman scattering is of the order of $L_R \approx 50$ Å [29]. Therefore, r can be estimated to be $r \approx 10$.

Using $E_g = 5.5$ eV, $r = 10$ and $E_R = 0.165$ eV, the average energy to generate an electron-hole pair in diamond can be approximated: $E_{pair} \approx 13.8$ eV. The experimental result of E_{pair} in diamond is equal to $E_{pair} = 13$ eV [31].

ULTRA VIOLET LASER EXCITATION

A photon energy of $\varepsilon = 6.1$ eV from an ultra violet (UV) laser excitation source (Chapter III) has a wave number of 5×10^4 cm^{-1}. This is much smaller than the size of a Brillouin zone.

To insure momentum conservation during the transition process, the electron transition from the valance band to the conduction band is limited to occur near the band edge. Therefore, the average energy to generate an electron-hole pair is equal to:

$$E_{pair} \approx \varepsilon \tag{2.11}$$

2.1.5 ELECTRON-HOLE PAIR DENSITY

The number of electron-hole pairs generated can be calculated from the total amount of energy absorbed and the energy to generate one electron-hole pair (E_{pair}). For charged particle excitation, the number of electron-hole pairs generated per unit length, $\bar{n}$, is equal to:

$$\bar{n} = \frac{\frac{d\mathcal{E}}{dx}}{E_{pair}} = \frac{\rho_m \frac{dE}{dx}}{E_{pair}} \tag{2.12}$$

For photon excitation, if an assumption is made that the absorption occurs in a rectangular box with the side along the sample normal direction and the side of the box is the absorption length $1/\gamma$, the electron-hole pair per unit length is given by:

$$\bar{n} = \frac{\frac{d\mathcal{E}}{dx}}{E_{pair}} \approx \frac{\gamma\, \mathcal{E}_{pulse}}{E_{pair}} \approx \frac{\gamma\, \mathcal{E}_{pulse}}{\varepsilon} \tag{2.13}$$

where $\mathcal{E}_{pulse}$ is the photon energy per pulse.

2.2 CHARGE COLLECTION PROCESS

An excess carrier density is generated by absorbing energy from an external excitation source. Driven by an electrical field, the motion of excess carriers induces current pulse which can be integrated to deduce the charge induced on the electric contacts. Excess carriers have a limited lifetime and the population of excess carriers decreases during the drift process due to the recombination processes in the material. The excess carrier densities can be determined by the rate equations.

2.2.1 Rate Equations for a Transient Process

The total current density through a material is composed by the drift current and the diffusion current contributed by electrons ($\vec{J}_n$) and holes ($\vec{J}_p$):

$$\vec{J}_n = e\mu_n \mathcal{N}\vec{E} + eD_n \nabla \mathcal{N} \quad (2.14)$$

$$\vec{J}_p = e\mu_p \mathcal{P}\vec{E} - eD_p \nabla \mathcal{P} \quad (2.15)$$

$\mathcal{N}$ and $\mathcal{P}$ are the total electron and hole density respectively:

$$\mathcal{N} = n_0 + n \quad (2.16)$$

$$\mathcal{P} = p_0 + p \quad (2.17)$$

These are the sum of the carrier densities in the thermal equilibrium state (indicated with subscript "$_0$") and the excess carrier densities. In diamond at room temperature, the intrinsic carrier density is very small compared with the excess carrier densities. Therefore, the total carrier density, $\mathcal{N}$ and $\mathcal{P}$, can be represented by n and p.

Based on the charge conservation, the continuity equations for electrons and holes are given by [7, 21]:

$$\frac{\partial n}{\partial t} = +\frac{1}{e}\nabla \cdot \vec{J}_n - \frac{n}{\tau_n} + g(\vec{r}, t) \quad (2.18)$$

$$\frac{\partial p}{\partial t} = -\frac{1}{e}\nabla \cdot \vec{J}_p - \frac{p}{\tau_p} + g(\vec{r}, t) \quad (2.19)$$

where $g(\vec{r}, t)$ is the charge generation term. Assuming that the illumination between the electric contacts is uniform, space charge is negligible and the generation term becomes independent of position $\vec{r}$. If no spacial gradient is present, $\nabla \cdot \vec{J}_n$ and $\nabla \cdot \vec{J}_p$ vanish [2]. Thus, the rate equations reduce to:

$$\frac{\partial n}{\partial t} = -\frac{n}{\tau_n} + g(t) \quad (2.20)$$

$$\frac{\partial p}{\partial t} = -\frac{p}{\tau_p} + g(t) \quad (2.21)$$

The traversal time for a charged particle passing a diamond film is approximately

[2]Carrier gradient and current density divergence will be discussed in Appendix C.

1 ps. This fast generation process implies that $g(t)$ becomes a $\delta(t)$ function. When the process of $t > 0$ is considered, $g(t) = 0$.

2.2.2 Excess Carrier Density

At $t = 0$, when an excess electron-hole pair density is generated by external radiation, the excess electron density equals to the excess hole density, $n_{\text{ionized}} = p_{\text{ionized}}$. In Figure 13, x' is used to represent where the electron-hole generation occurs at $t = 0$. At time t, an excess carrier has drifted to a position x under an electric field $\vec{E}$. The position of the electric contact with a negative bias, marked with "$-$", is $x = L$; the positive biased electric contact is at $x = 0$, marked with "$+$". Because of recombination, the number of excess carriers decreases with time. The excess electron density $n = n(x)$ and excess hole density $p = p(x)$ can be solved from the rate equations.

The collection distance introduced in Chapter I is the average distance which an excess electron and an excess hole have drifted apart under an electric field E:

$$\begin{aligned} d &= v_d^n \tau_n + v_d^p \tau_p \\ &= d^n + d^p \end{aligned} \quad (2.22)$$

where $d^n = v_d^n \tau_n$ and $d^p = v_d^p \tau_p$ are the distances which the electron and hole drift under E. Since excess electrons drift towards the negative direction of the x axis while excess holes drift towards the positive direction of the x axis (Figure 13), the drift velocities can be written as:

$$v_d^n = -\frac{dx}{dt} \quad (2.23)$$

$$v_d^p = +\frac{dx}{dt} \quad (2.24)$$

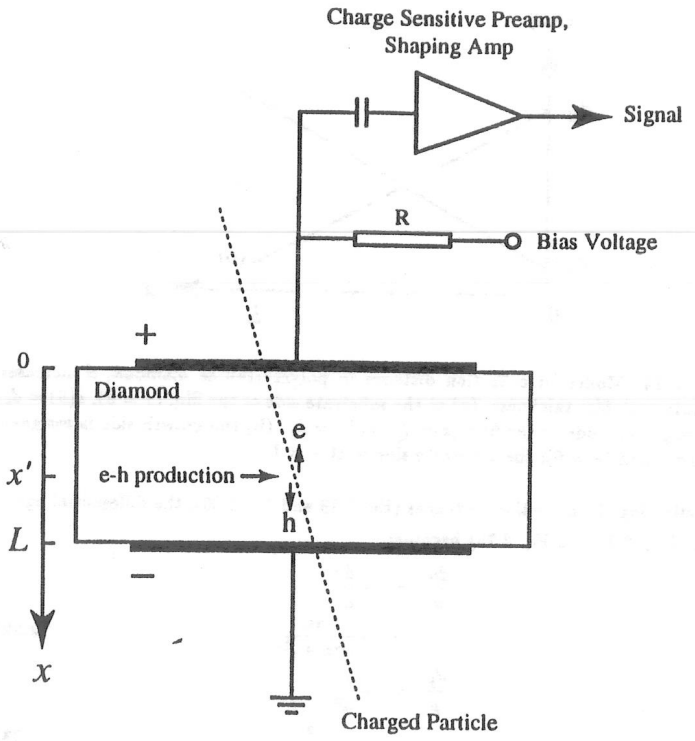

Figure 13: The charge collection process in diamond. The shaded areas represent the electric contacts. Excess electron-hole pair generation occurs along the path of the charged particle where $n_{\text{ionized}} = p_{\text{ionized}}$. The excess electrons drift towards the electric contact at $x = 0$; the excess holes drift towards the electric contact at $x = L$.

Using the definition of collection distance, the rate equations (Eq. 2.20 and Eq. 2.21) can be rewritten in spacial form:

$$\frac{dn}{n} = -\frac{dt}{\tau_n} = +\frac{dx}{v_d^n \tau_n} = +\frac{dx}{d^n} \tag{2.25}$$

$$\frac{dp}{p} = -\frac{dt}{\tau_p} = -\frac{dx}{v_d^p \tau_p} = -\frac{dx}{d^p} \tag{2.26}$$

The solution of these differential equations describes the decaying behavior of the excess carrier densities. As mentioned in Chapter I, unlike single crystal diamond, polycrystalline diamond films have a multi-grain structure. Moreover, the diamond grains demonstrate a columnar structure along the film growth direction. As a result, many material properties vary with the thickness of the film (see Chapter IV). This special feature of polycrystalline CVD diamond film has been taken into account in describing the electrical properties. Thus, the theoretical analysis of this chapter is separated into two parts: (A) single crystal diamond and (B) polycrystalline diamond.

(A) Single Crystal Diamond

The collection distance (d^n, d^p) can be treated as a constant throughout the sample for a natural diamond due to the single crystal nature. The solutions for the rate equations (Eq. 2.25 and Eq. 2.26) are simple exponentials. The initial conditions when $t = 0$ (or $x = x'$) are: $n(x') = n_{\text{ionized}}$ and $p(x') = p_{\text{ionized}}$. The solutions are:

$$n(x, x') = n_{\text{ionized}} \exp\left(-\frac{x' - x}{d^n}\right) \qquad (x < x') \tag{2.27}$$

$$p(x, x') = p_{\text{ionized}} \exp\left(-\frac{x - x'}{d^p}\right) \qquad (x' < x < L) \tag{2.28}$$

It can be seen that both excess electrons and excess holes follow the same decay behavior.

(B) Polycrystalline Diamond

The situation discussed above is appropriate only when the collection distance is a constant across the sample. When a gradient of collection distance exists along the columnar direction, it may be approximated, to first order, by using a linear function with x (Figure 14a, the situation shown in Figure 14b can be carried out by analogy, the results are the same.).

$$d^{n} = \left(\frac{d_g^{n} - d_s^{n}}{L}\right) x + d_s^{n} \stackrel{\text{def}}{=} \alpha^{n} x + \beta^{n} \tag{2.29}$$

$$d^{p} = \left(\frac{d_g^{p} - d_s^{p}}{L}\right) x + d_s^{p} \stackrel{\text{def}}{=} \alpha^{p} x + \beta^{p} \tag{2.30}$$

where d_g^{n}, d_g^{p}, d_s^{n} and d_s^{p} are the collection distances at the growth side and substrate side of the diamond film for both type of carriers. The superscript "n" and "p" represent the values for electron and hole respectively. The other parameters are defined as:

$$\begin{aligned} \alpha^{n} &\stackrel{\text{def}}{=} \frac{d_g^{n} - d_s^{n}}{L} \\ \alpha^{p} &\stackrel{\text{def}}{=} \frac{d_g^{p} - d_s^{p}}{L} \\ \beta^{n} &\stackrel{\text{def}}{=} d_s^{n} \\ \beta^{p} &\stackrel{\text{def}}{=} d_s^{p} \end{aligned} \tag{2.31}$$

When $\alpha^{n} \ll 1$ ($d_g^{n} - d_s^{n} \ll L$), the difference of collection distance between the two surfaces is negligible. This situation can be treated in the same way as for a single crystal. In the following discussions, $\alpha^{n} \geq 1$ and $\alpha^{p} \geq 1$ are treated for polycrystalline diamond.

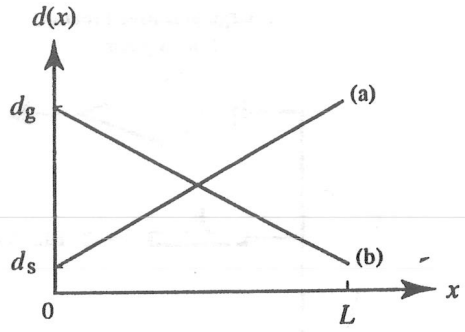

Figure 14: Model for collection distance in polycrystalline diamond, d increases linearly with film thickness. (a) at the substrate side of the film ($x = 0$), $d(0) = d_s$; at the growth side of the film ($x = L$), $d(L) = d_g$. (b) the growth side is assigned as the origin ($x = 0$); the substrate side is at $x = L$.

Substituting the collection distances (Eq. 2.29 and Eq. 2.30), the differential equations (Eq. 2.25 and Eq. 2.26) become:

$$\begin{aligned} \frac{dn}{n} &= +\frac{dx}{d^{n}} \\ &= +\frac{dx}{\alpha^{n} x + \beta^{n}} \end{aligned} \tag{2.32}$$

$$\begin{aligned} \frac{dp}{p} &= -\frac{dx}{d^{p}} \\ &= -\frac{dx}{\alpha^{p} x + \beta^{p}} \end{aligned} \tag{2.33}$$

Using the initial conditions: $x = x'$ when $t = 0$, $n(x') = n_{\text{ionized}}$ and $p(x') = p_{\text{ionized}}$, the solutions for these differential equations are obtained:

$$n(x, x') = n_{\text{ionized}} \left(\frac{x + \beta^{n}/\alpha^{n}}{x' + \beta^{n}/\alpha^{n}}\right)^{+\frac{1}{\alpha^{n}}} \qquad (x < x') \tag{2.34}$$

$$p(x, x') = p_{\text{ionized}} \left(\frac{x + \beta^{p}/\alpha^{p}}{x' + \beta^{p}/\alpha^{p}}\right)^{-\frac{1}{\alpha^{p}}} \qquad (x' < x < L) \tag{2.35}$$

2.2.3 Charge Induction on Electric Contacts

Under an electric field, the excess electrons and holes move in opposite directions. The motion of the charge carriers induces a current pulse. The charge induced on the electric contacts is called $Q_{\text{collected}}$. To use a simplified model to describe the charge induction process, a few assumptions are made: (1) the ionization chamber is modeled by a parallel plate capacitor (electric contact spacing is L and contact area is S); (2) the process during which the charge particle is brought to this capacitor from infinity is neglected.

When $t = 0$ ($x = x'$), the total number of excess electrons or holes in a cylinder with a volume of $dv' = Sdx'$ is given by $n_{\text{ionized}}\ dv'$ or $p_{\text{ionized}}\ dv'$. If we track the excess carriers in this cylinder dv', the number of excess carriers at x is given by $n(x, x')\ dv'$ or $p(x, x')\ dv'$. When these excess carriers have drifted a distance dx under $\vec{E}$, the induced charge on the electric contacts, $dQ_{\text{collected}}$, can be given by [32, 33, 34]:

$$dQ^{\text{n}}_{\text{collected}} = -[e\ n(x, x')\ dv'] \frac{dx}{L} \tag{2.36}$$

$$dQ^{\text{p}}_{\text{collected}} = +[e\ p(x, x')\ dv'] \frac{dx}{L} \tag{2.37}$$

where the minus sign in Eq. 2.36 is due to the fact that dx is negative for excess electrons. Two different derivations are shown in Appendix B. The total charge induced by the two types of excess carriers can be calculated by superposition:

$$Q_{\text{collected}} = Q^{\text{n}}_{\text{collected}} + Q^{\text{p}}_{\text{collected}} \tag{2.38}$$

Substituting the excess carrier densities solved from the rate equations (Eq. 2.36 and Eq. 2.37), the total charge collected on the electric contacts can be obtained.

(A) Single Crystal Diamond

Substituting the solutions of the rate equations for single crystal diamond (Eq. 2.27 and Eq. 2.28),

$$dQ^{\text{n}}_{\text{collected}} = -[e\ n(x, x')\ dv'] \times \frac{dx}{L} = -e\ n_{\text{ionized}}\ dv'\ \exp\left(-\frac{x' - x}{d^{\text{n}}}\right) \times \frac{dx}{L} \tag{2.39}$$

$$dQ^{\text{p}}_{\text{collected}} = +[e\ p(x, x')\ dv'] \times \frac{dx}{L} = +e\ p_{\text{ionized}}\ dv'\ \exp\left(-\frac{x - x'}{d^{\text{p}}}\right) \times \frac{dx}{L} \tag{2.40}$$

Then the total charge induced on the electric contacts can be integrated as:

$$Q^{\text{n}}_{\text{collected}} = \int dQ^{\text{n}}_{\text{collected}} = -\int_V dv' \int_{x'}^{0} e\ n(x, x') \times \frac{dx}{L} \tag{2.41}$$

$$Q^{\text{p}}_{\text{collected}} = \int dQ^{\text{p}}_{\text{collected}} = +\int_V dv' \int_{x'}^{L} e\ p(x, x') \times \frac{dx}{L} \tag{2.42}$$

The total volume of the diamond ionization chamber is $V = \text{S} \times L$, thus, using $dv' = Sdx'$, we have:

$$Q^{\text{n}}_{\text{collected}} = -\text{S} \int_0^L dx' \int_{x'}^{0} e\ n(x, x') \times \frac{dx}{L} \tag{2.43}$$

$$Q^{\text{p}}_{\text{collected}} = +\text{S} \int_0^L dx' \int_{x'}^{L} e\ p(x, x') \times \frac{dx}{L} \tag{2.44}$$

Integrating, we find:

$$Q^{\text{n}}_{\text{collected}} = Q_{\text{ionized}} \frac{d^{\text{n}}}{L} \left[1 - \frac{d^{\text{n}}}{L}\left(1 - e^{-\frac{L}{d^{\text{n}}}}\right)\right] \tag{2.45}$$

$$Q^{\text{p}}_{\text{collected}} = Q_{\text{ionized}} \frac{d^{\text{p}}}{L} \left[1 - \frac{d^{\text{p}}}{L}\left(1 - e^{-\frac{L}{d^{\text{p}}}}\right)\right] \tag{2.46}$$

where Q_{ionized} is defined as total number of excess electrons or holes generated by charged particles:

$$Q_{\text{ionized}} \overset{\text{def}}{=} n_{\text{ionized}} \times (SL) = p_{\text{ionized}} \times (SL) \tag{2.47}$$

When $L \gg d^n, d^p$, the charge collected on the electric contacts becomes:

$$Q^n_{\text{collected}} \approx \frac{d^n}{L} Q_{\text{ionized}} \qquad (L \gg d^n) \tag{2.48}$$

$$Q^p_{\text{collected}} \approx \frac{d^p}{L} Q_{\text{ionized}} \qquad (L \gg d^p) \tag{2.49}$$

The total induced charge on the electric contacts measured by the CPIC technique is equal to:

$$\begin{aligned} Q_{\text{collected}} &= Q^n_{\text{collected}} + Q^p_{\text{collected}} \\ &\approx \frac{d_{\text{CPIC}}}{L} Q_{\text{ionized}} \qquad (L \gg d^n, d^p) \end{aligned} \tag{2.50}$$

where $d_{\text{CPIC}} = d^n + d^p$.

(B) Polycrystalline Diamond

Using solutions of the rate equations for polycrystalline diamond film (Eq. 2.34 and Eq. 2.35),

$$dQ^n_{\text{collected}} = -e\, n_{\text{ionized}}\, dv' \left(\frac{x + \beta^n/\alpha^n}{x' + \beta^n/\alpha^n}\right)^{+\frac{1}{\alpha^n}} \times \frac{dx}{L} \tag{2.51}$$

$$dQ^p_{\text{collected}} = +e\, p_{\text{ionized}}\, dv' \left(\frac{x + \beta^p/\alpha^p}{x' + \beta^p/\alpha^p}\right)^{-\frac{1}{\alpha^p}} \times \frac{dx}{L} \tag{2.52}$$

Integrating, the charge collected on the electric contacts for polycrystalline diamond is obtained.

When $\alpha^n = 1$ ($d^n_g - d^n_s = L$), using the solution of the charge collected in Eq. 2.34, the integral for the charge collected on the electric contacts is given by:

$$\begin{aligned} Q^n_{\text{collected}} &= -S \int_0^L dx' \int_{x'}^0 e\, n(x, x') \times \frac{dx}{L} \\ &= -\frac{Q_{\text{ionized}}}{L} \int_0^L dx' \int_{x'}^0 \left(\frac{x + \beta^n}{x' + \beta^n}\right) \times \frac{dx}{L} \\ &= \frac{Q_{\text{ionized}}}{2L^2} \left[\frac{L^2}{2} + L\beta^n + (\beta^n)^2 \ln \frac{\beta^n}{L + \beta^n}\right] \end{aligned} \tag{2.53}$$

For the charge collected due to excess holes,

$$Q^p_{\text{collected}} = \frac{Q_{\text{ionized}}}{2L^2} \left[\frac{L^2}{2} + L\beta^p + (\beta^p)^2 \ln \frac{\beta^p}{L + \beta^p}\right] \tag{2.54}$$

For the case of $\alpha^n \neq 1$, substituting the solution from Eq. 2.34, the charge collected is equal to:

$$Q^n_{\text{collected}} = \frac{Q_{\text{ionized}}}{L^2} \frac{1}{\frac{1}{\alpha^n} + 1} \left\{\frac{L^2}{2} + \frac{\beta^n L}{\alpha^n} + \frac{1}{\frac{1}{\alpha^n} - 1} \left[\left(\frac{\beta^n}{\alpha^n}\right)^{1 + \frac{1}{\alpha^n}} \left(L + \frac{\beta^n}{\alpha^n}\right)^{1 - \frac{1}{\alpha^n}} - \left(\frac{\beta^n}{\alpha^n}\right)^2\right]\right\} \tag{2.55}$$

The contribution by excess holes is given by:

$$\begin{aligned} Q^p_{\text{collected}} &= \frac{Q_{\text{ionized}}}{L^2} \frac{1}{\frac{1}{\alpha^p} - 1} \left\{\frac{L^2}{2} + \frac{\beta^p L}{\alpha^p} + \frac{1}{\frac{1}{\alpha^p} + 1} \left[\left(\frac{\beta^p}{\alpha^p}\right)^{1 + \frac{1}{\alpha^p}} \left(L + \frac{\beta^p}{\alpha^p}\right)^{1 - \frac{1}{\alpha^p}} - \left(L + \frac{\beta^p}{\alpha^p}\right)^2\right]\right\} \\ &= \frac{Q_{\text{ionized}}}{L^2} \frac{1}{\frac{1}{\alpha^p} + 1} \left\{\frac{L^2}{2} + \frac{\beta^p L}{\alpha^p} + \frac{1}{\frac{1}{\alpha^p} - 1} \left[\left(\frac{\beta^p}{\alpha^p}\right)^{1 + \frac{1}{\alpha^p}} \left(L + \frac{\beta^p}{\alpha^p}\right)^{1 - \frac{1}{\alpha^p}} - \left(\frac{\beta^p}{\alpha^p}\right)^2\right]\right\} \end{aligned} \tag{2.56}$$

It can be seen that the total charge contributed by excess electrons and excess holes has the same form. For the polycrystalline diamond films currently in use, $L \gg d_g^n, d_g^p, d_s^n, d_s^p$. Under these conditions, the last two terms in the two equations above are negligible compared with the first two terms. Then:

$$\begin{aligned} Q^n_{\text{collected}} &\approx \frac{Q_{\text{ionized}}}{L^2} \frac{1}{\frac{1}{\alpha^n}+1} \left(\frac{L^2}{2} + \frac{\beta^n L}{\alpha^n} \right) \\ &= \frac{\bar{d}^n}{L} \left(\frac{1}{\alpha^n + 1} \right) Q_{\text{ionized}} \\ &\approx \frac{\bar{d}^n}{L} Q_{\text{ionized}} \qquad (L \gg d_g^n, d_s^n) \end{aligned} \tag{2.57}$$

$$\begin{aligned} Q^p_{\text{collected}} &\approx \frac{Q_{\text{ionized}}}{L^2} \frac{1}{\frac{1}{\alpha^p}+1} \left(\frac{L^2}{2} + \frac{\beta^p L}{\alpha^p} \right) \\ &= \frac{\bar{d}^p}{L} \left(\frac{1}{\alpha^p + 1} \right) Q_{\text{ionized}} \\ &\approx \frac{\bar{d}^p}{L} Q_{\text{ionized}} \qquad (L \gg d_g^p, d_s^p) \end{aligned} \tag{2.58}$$

where

$$\begin{aligned} \bar{d}^n &= \frac{d_g^n + d_s^n}{2} \\ \bar{d}^p &= \frac{d_g^p + d_s^p}{2} \end{aligned} \tag{2.59}$$

The total charge collected is

$$Q_{\text{collected}} \approx \frac{d_{\text{CPIC}}}{L} Q_{\text{ionized}} \qquad (L \gg d_g^n, d_g^p, d_s^n, d_s^p) \tag{2.60}$$

with $d_{\text{CPIC}} = [(d_g^n + d_g^p) + (d_s^e + d_s^p)]/2$. In either the CPIC or the PIC measurements, the contribution from excess electrons and excess holes can not be distinguished. To simplify the notations, $d_g \stackrel{\text{def}}{=} d_g^n + d_g^p$ and $d_s \stackrel{\text{def}}{=} d_s^n + d_s^p$ are used. Hence:

$$d_{\text{CPIC}} = \frac{d_g + d_s}{2} \tag{2.61}$$

This equation shows that d_{CPIC}, a characterization of the electrical properties of diamond radiation detectors, is equal to the average value of the surface collection

distances when a constant gradient of the electrical properties exists along the columnar direction.

It is worth noting that when $\beta^n = 0$ and $\beta^p = 0$, $(d_s = 0)$,

$$d_{\text{CPIC}} = \frac{d_g}{2} \qquad (d_s = 0) \tag{2.62}$$

The average collection distance in this case is equal to the half of the value of the collection distance at growth side of the film.

2.3 Electric Contacts

Electric contacts have been an important topic of research for electronic devices. They represent the boundary conditions needed for the solution to the charge collected on the electric contacts. When the collection distance is small ($d \ll L$), most of excess carriers are not able to drift to the electric contacts, the boundary conditions at the electric contacts do not play a key role. However, when d is comparable to the film thickness, different boundary conditions at the electric contacts must be considered.

2.3.1 Blocking Contacts

A high resistivity layer at the electric contact region may exist due to a large amount of recombination centers at the contact junction. This layer is called *blocking layer* [14] and the contact with a blocking layer is called a *blocking contact*. When reaching a blocking electric contact, a charge carrier can not jump over or tunnel through the junction barrier. It is trapped by surface states. After reaching the contact, it no longer contributes to the conductivity. In addition, no carrier can be injected into the material from the external circuit.

(A) Single Crystal Diamond

A numerical calculation is used to calculate the charge collected on the electric contacts $Q^{n}_{collected}$ (Figure 15). When $d^{n} = L$, $Q^{n}_{collected} = 0.37\ Q_{ionized}$. The total charge collected is equal to $0.74\ Q_{ionized}$. When $d^{n} \gg L$, $Q^{n}_{collected} \approx 0.5\ Q_{ionized}$. Then, the total charge collected is equal to:

$$Q_{collected} = Q^{n}_{collected} + Q^{p}_{collected} \approx Q_{ionized} \qquad (d^{n}, d^{p} \gg L) \qquad (2.63)$$

All the charges generated in the ionization process are collected.

(B) Polycrystalline Diamond

For polycrystalline diamond, the results from a numerical calculation for the charge collected on the electric contacts, $Q^{n}_{collected}$, are shown in Figure 16. For $d^{n} \gg L$, $Q^{e}_{collected} \approx 0.5\ Q_{ionized}$. Then, the total collected charge is equal to:

$$Q_{collected} \approx Q_{ionized} \qquad (d^{n} - d^{n} \gg L) \qquad (2.64)$$

2.3.2 Ohmic Contacts

For an ohmic contact, no surface barrier exists. When each carrier reaches an ohmic contact, it is elevated by the power supply in the external circuit, and then injected from the other electric contact into the diamond. The mechanism to reduce the current is the recombination process in bulk material. When $d \gg L$, the diamond can keep its high conductive status until all excess carriers recombine.

(A) Single Crystal Diamond

After the excess carrier generation occurs at $x = x'$, excess holes are drifted toward the electric contact at $x = L$ (Figure 13). After being lifted by the power supply in

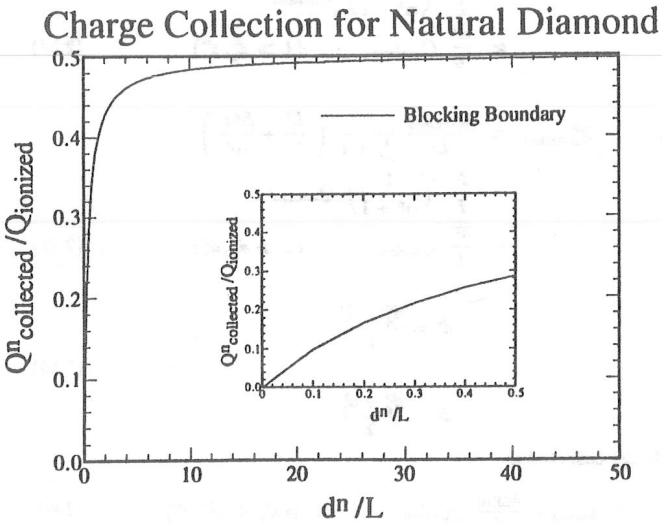

Figure 15: Numerical calculation of the charge collected, $Q^{n}_{collected}$, for a single crystal diamond detector with blocking contacts. For $d^{n} = L$, $Q^{n}_{collected} = 0.37\ Q_{ionized}$; for $d^{n} \gg L$, $Q^{n}_{collected} \approx 0.5\ Q_{ionized}$. The inset shows that $Q^{n}_{collected}/Q_{ionized}$ is approximately a linear function of d^{n}/L when $d^{n}/L < 0.1$.

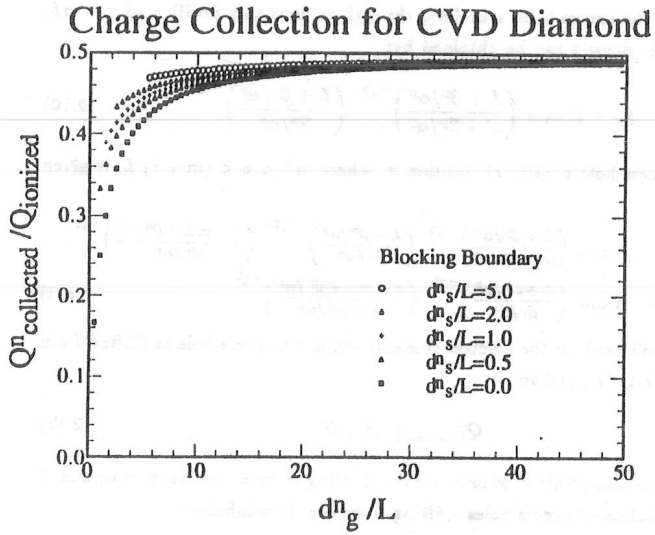

Figure 16: Numerical calculation of charge collected, $Q^{n}_{collected}$, for a polycrystalline diamond detector with blocking contacts. For $d^{n} \gg L$, $Q^{n}_{collected} \approx 0.5\, Q_{ionized}$.

the external circuit, these holes are injected into diamond from the electric contact at $x = 0$, then drift back towards the position where the ionization occurs. In this "cycle", the collection distance is a constant. The excess carrier density decays by a factor of $\exp\left(-\frac{L}{d^{p}}\right)$. As shown in Figure 17, this periodical boundary condition is equivalent to a diamond with infinite thickness composed of diamond films with thickness L in series. Thus, infinity can be used as the upper limit of the induction integral for x. Using Eq. 2.28,

$$\begin{aligned} Q^{p}_{collected} &= S\int_{0}^{L}\int_{x'}^{\infty} e\, p_{ionized} \exp\left(-\frac{x-x'}{d^{p}}\right)\frac{dx}{L}\,dx' \\ &\approx Q_{ionized}\frac{d^{p}}{L} \qquad (d^{p} \geq L) \end{aligned} \tag{2.65}$$

Adding the excess electron contribution, we find:

$$Q_{collected} \approx Q_{ionized}\frac{d_{CPIC}}{L} \qquad (d_{CPIC} \geq L) \tag{2.66}$$

When $d_{CPIC} = L$, $Q_{collected} = Q_{ionized}$, all the charges are collected. When $d_{CPIC} > L$, the integrated charge collected on the electric contacts, $Q_{collected}$, may be larger than the number of excess carriers generated by ionization, $Q_{collected} > Q_{ionized}$. This means that gain occurs:

$$\frac{Q_{collected}}{Q_{ionized}} \approx \frac{d_{CPIC}}{L} \geq 1 \tag{2.67}$$

(B) Polycrystalline Diamond

Unlike a single crystal, in a polycrystalline diamond, the material quality is different at the electric contact ($x = 0$) from that at the electric contact ($x = L$). In Figure 17, a "saw tooth model" is used to substitute the periodic boundary condition. Using Eq. 2.55, the excess hole density at $x = L$ is equal to:

$$p_{1} = p_{ionized}\left(\frac{L+\beta^{p}/\alpha^{p}}{x'+\beta^{p}/\alpha^{p}}\right)^{-\frac{1}{\alpha^{p}}} \tag{2.68}$$

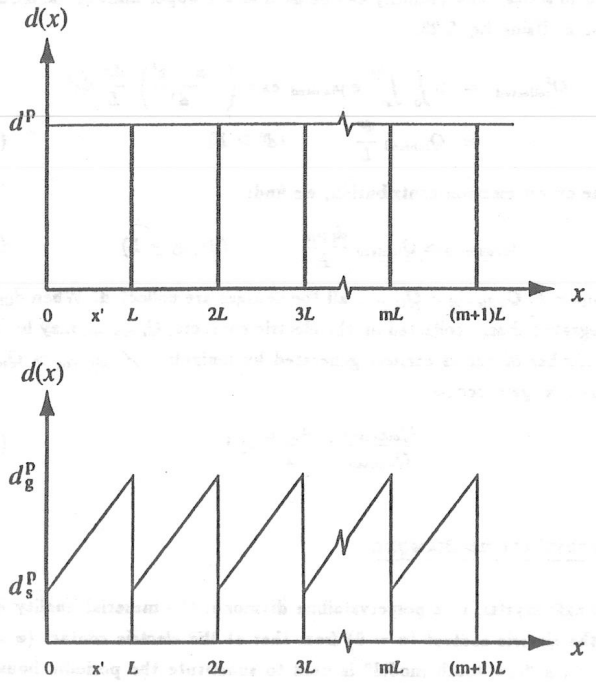

Figure 17: Boundary condition for ohmic contacts. The upper diagram is for single crystal diamond, in which the collection distance is a constant. The lower diagram represents polycrystalline diamond. A linear model is used for the collection distance between mL and (m+1)L. Thus, a "saw tooth" shape is shown.

The excess hole density at $x = 2L$ is equal to:

$$p_2 = p_{\text{ionized}} \left(\frac{L + \beta^p/\alpha^p}{x' + \beta^p/\alpha^p} \right)^{-\frac{1}{\alpha^p}} \left(\frac{L + \beta^p/\alpha^p}{\beta^p/\alpha^p} \right)^{-\frac{1}{\alpha^p}} \tag{2.69}$$

Similarly, for the excess holes travelling through m films to a position of $x = mL$, the excess hole density can be obtained by:

$$p_m = p_{\text{ionized}} \left(\frac{L + \beta^p/\alpha^p}{x' + \beta^p/\alpha^p} \right)^{-\frac{1}{\alpha^p}} \left(\frac{L + \beta^p/\alpha^p}{\beta^p/\alpha^p} \right)^{-\frac{m-1}{\alpha^p}} \tag{2.70}$$

Thus, the excess hole density at position x, where $mL < x < (m+1)\,L$, is given by:

$$\begin{aligned} p_m(x, x') &= p_{\text{ionized}} \left(\frac{L + \beta^p/\alpha^p}{x' + \beta^p/\alpha^p} \right)^{-\frac{1}{\alpha^p}} \left(\frac{L + \beta^p/\alpha^p}{\beta^p/\alpha^p} \right)^{-\frac{m-1}{\alpha^p}} \left(\frac{x - mL + \beta^p/\alpha^p}{\beta^p/\alpha^p} \right)^{-\frac{1}{\alpha^p}} \\ &= p_{\text{ionized}} \left(\frac{L + \beta^p/\alpha^p}{\beta^p/\alpha^p} \right)^{-\frac{m}{\alpha^p}} \left(\frac{x - mL + \beta^p/\alpha^p}{x' + \beta^p/\alpha^p} \right)^{-\frac{1}{\alpha^p}} \end{aligned} \tag{2.71}$$

The charge collected on the electric contacts when an excess hole is drifted from $x = x'$ to infinity is equal to:

$$Q^p_{\text{collected}} = \mathcal{A} + \mathcal{B} \tag{2.72}$$

where $\mathcal{A}$ is the contribution of excess holes drifting from $x = x'$ to $x = L$; and $\mathcal{B}$ is the contribution of excess holes drifting from $x = L$ to infinity:

$$\mathcal{A} = S \int_0^L \int_{x'}^L e\, p_{\text{ionized}} \left(\frac{x + \beta^p/\alpha^p}{x' + \beta^p/\alpha^p} \right)^{-\frac{1}{\alpha^p}} \frac{dx}{L}\, dx' \tag{2.73}$$

$$\mathcal{B} = \sum_{m=1}^{\infty} \left[S \int_0^L \int_{mL}^{(m+1)\,L} p_m(x, x') \frac{dx}{L}\, dx' \right] \tag{2.74}$$

A numerical calculation for the charge collected at the electric contacts is shown in Figure 18. When $d_s = 0$, the boundary condition at the electric contact on the substrate side of the diamond film acts as a blocking contact. The maximum charge collected on the electric contacts is Q_{ionized}. When $d_s > 0$, gain may occur.

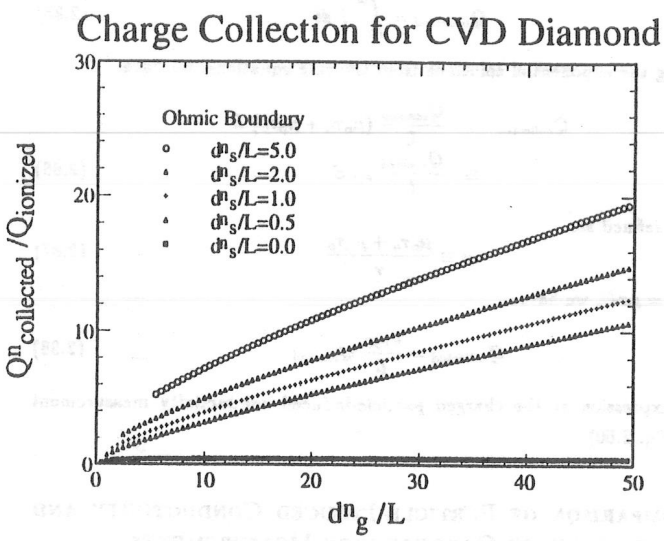

Figure 18: Numerical calculation charge collected, $Q^n_{\text{collected}}$, for a polycrystalline diamond detector with ohmic contacts. Gain ($Q_{\text{collected}} > Q_{\text{ionized}}$) occurs when $d^n_s > 0$.

2.4 Photo-Induced Conductivity

Most of the photo-induced conductivity (PIC) measurements have been performed at Lawrence Livermore National Laboratory. Since the PIC results will be used to compare with the results from the CPIC measurements, photo-induced conductivity is briefly discussed.

This transient process and experimental techniques are similar to the CPIC measurements. After excess electron-hole pair generation by the illumination of photons with energy above the band gap E_g, the motion of excess electrons and holes under an electric field $\vec{E}$ induces a current pulse. From the integration of the current pulse, the charge collected on electric contacts, $Q_{\text{collected}}$, can be obtained. In addition, from the photocurrent decay, the carrier lifetime, τ, can be derived. Instead of using the spacial form of the rate equations (Eq. 2.25 and Eq. 2.26), the rate equations in the time coordinate are used (Eq. 2.20 and Eq. 2.21):

$$\frac{\partial n}{\partial t} = -\frac{n}{\tau_n} + g(t) \tag{2.75}$$

$$\frac{\partial p}{\partial t} = -\frac{p}{\tau_p} + g(t) \tag{2.76}$$

Because of the large band gap of diamond, UV excitation from a laser or x-ray from synchrotron are used to excite electrons from the valance band to the conduction band. From Table 2, we can see that the two types of excitations are in different time and energy regimes.

Table 2: Photon Pulse Excitation Sources [35].

Source	ε (eV)	Width (ps)	Shape	Rate (Hz)
UV (Laser)	6.1	≤ 5	$\delta(t)$	~ 10
X-ray (Synchrotron)	$300 \sim 5000$	350	Gaussian	1.3×10^6

2.4.1 X-RAY SYNCHROTRON EXCITATION

The excitation pulse can be modeled using a Gaussian function with a characterized time σ_G:

$$g(t) = \frac{\bar{n}}{wL} \times \frac{1}{\sqrt{2\pi}\sigma_G} e^{-\frac{t^2}{2\sigma_G^2}} \tag{2.77}$$

where w and L are the electric contact width and spacing and $\bar{n}$ can be calculated from Eq. 2.13. The solutions of the rate equations are given by:

$$n(t) = \frac{n_{ionized}}{2} \exp\left(\frac{\sigma_G^2}{2\tau_n^2} - \frac{t}{\tau_n}\right)\left\{\text{erf}\left[\frac{1}{\sqrt{2}}\left(\frac{t}{\sigma_G} - \frac{\sigma_G}{\tau_n}\right)\right] + 1\right\} \tag{2.78}$$

$$p(t) = \frac{p_{ionized}}{2} \exp\left(\frac{\sigma_G^2}{2\tau_p^2} - \frac{t}{\tau_p}\right)\left\{\text{erf}\left[\frac{1}{\sqrt{2}}\left(\frac{t}{\sigma_G} - \frac{\sigma_G}{\tau_p}\right)\right] + 1\right\} \tag{2.79}$$

$$\tag{2.80}$$

where the error function is defined as:

$$\text{erf}(x) \stackrel{\text{def}}{=} \frac{2}{\sqrt{\pi}} \int_0^x e^{-x'^2}\, dx' \tag{2.81}$$

For x-ray excitation from synchrotron, τ can be determined [27] by numerical integration.

2.4.2 LASER EXCITATION

For laser excitation, the fast laser pulse is considered a $\delta(t)$ function because the recording system has bandwidth limitation. Thus Eq. 2.78 and Eq. 2.79 are reduced to simple exponential terms:

$$n(t) = n_{ionized} \exp\left(-\frac{t}{\tau_n}\right) \tag{2.82}$$

$$p(t) = p_{ionized} \exp\left(-\frac{t}{\tau_p}\right) \tag{2.83}$$

In practice, the current pulse is delivered by a transmission line with a characteristic resistance of 50 Ω to a scope. The current density $J(t)$ is equal to:

$$J(t) = e\left[n(t)\mu_n + p(t)\mu_p\right] E \tag{2.84}$$

Using the expression for the current $I = J \times S$ (S is the cross-sectional area of the current, which is equal to the product of w and the absorption length $1/\gamma$; $v = SL$), the charge collected can be calculated by:

$$Q_{collected} = \int_0^\infty I\, dt \tag{2.85}$$

Substituting the exponential solutions from the rate equations, we have:

$$\begin{aligned} Q_{collected} &= \frac{Q_{ionized}}{L}\left(\mu_n\tau_n + \mu_p\tau_p\right) E \\ &\equiv \frac{Q_{ionized}}{L}\mu\tau E \end{aligned} \tag{2.86}$$

where μ is defined as:

$$\mu \equiv \frac{\mu_n\tau_n + \mu_p\tau_p}{\tau} \tag{2.87}$$

Using $d_{PIC} = \mu\tau E$, we have:

$$Q_{collected} = \frac{d_{PIC}}{L} Q_{ionized} \tag{2.88}$$

the same expression as the charged particle-induced conductivity measurement (Eq. 2.50, Eq. 2.60).

2.5 COMPARISON OF PARTICLE-INDUCED CONDUCTIVITY AND PHOTO-INDUCED CONDUCTIVITY MEASUREMENTS

To summarize the results from the discussions above, the general expression of the collection distance for both single crystalline diamond and polycrystalline diamond measured by the CPIC or the PIC techniques can be written as the following:

$$Q_{collected} = \frac{d_{meas}}{L} Q_{ionized} \tag{2.89}$$

or

$$d_{meas} = \frac{Q_{collected}}{Q_{ionized}} L \tag{2.90}$$

where d_{meas} can be either d_{CPIC} or d_{PIC}.

◇ for single crystal diamond:

$$d_{CPIC} = d_{bulk} = d_{PIC} = d_{surface} \tag{2.91}$$

◇ for polycrystalline diamond (Eq. 2.61):

$$d_{CPIC} = \frac{d_g + d_s}{2} \tag{2.92}$$

$$d_{PIC} = d_{surface} = d_g \text{ or } d_s \tag{2.93}$$

For a special case when $d_s = 0$,

$$d_{CPIC} = \frac{d_{PIC}}{2} \qquad (d_s = 0) \tag{2.94}$$

These are the relationships between the results from the CPIC measurements and PIC measurements. The CPIC study yields information about the bulk of the diamond films while the PIC measurement yields surface information. The two experimental techniques compliment each other and allow us to obtain a complete picture of the electrical properties in diamond.

CHAPTER III

Charged Particle-Induced Conductivity

Charged particle induced conductivity (CPIC) measurements have been performed on both single crystal natural diamond and polycrystalline CVD diamond. To perform these measurements, a metal-insulator-metal (MIM) structure is fabricated on each diamond to create an ohmic contact with the diamond. In order to insure that good contact is made to the diamond a current-voltage (I-V) curve is taken for each diamond. Figure 92 shows a typical I-V curve illustrating a symmetric linear relationship. Contacts which do not have good I-V characteristics are removed and re-applied.

Typically the diamond films studied were a few hundred microns thick and had an approximate lateral size of 50 mm^2. Large area (3 cm×3 cm), continuous polycrystalline films have also been tested. The response of these detectors to charged particles with different species, different energy and from different sources has been observed. The excitation sources include charged particle accelerator beam at the TRI-University Meson Facility (TRIUMF) in Canada and radioactive source (^{90}Sr). The CPIC measurements are summarized in Table 3.

From the response of the detectors to the charged particles, the electrical properties have been investigated. A comparison of single crystal diamond and polycrystalline diamond has been made.

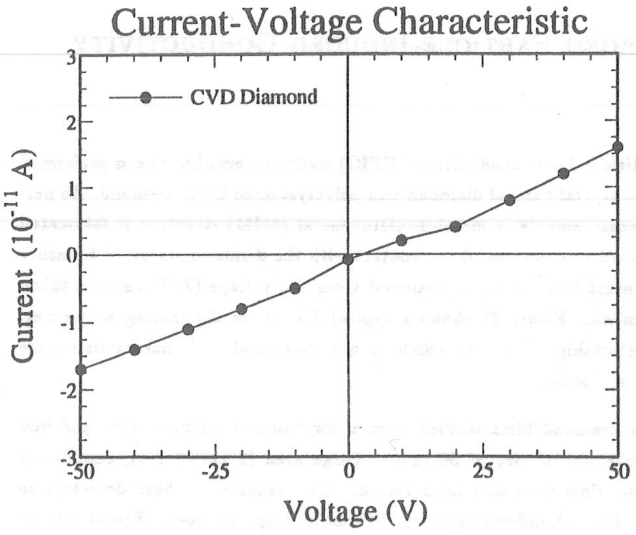

Figure 19: Current-voltage characteristics of a polycrystalline diamond detector.

Table 3: Charged particle-induced conductivity measurements.

Excitation Source	Particle(s)	Energy (MeV)
Radioactive Source (^{90}Sr)	e^-	2.28†
TRIUMF (M13 beam line)	π^-, μ^-, e^-	$\sim$ 100

† cut-off energy of three body decay spectrum

3.1 Experimental Techniques

3.1.1 Accelerator Beam Test at TRIUMF

M13 beam line at TRIUMF national laboratory consists of pions, muons and electrons with momentum, p, of 100 MeV/c (Table 4). At this momentum, electrons are close to minimum ionizing, while muons are 1.7 times of minimum ionizing particle and pions are 2.5 times of minimum ionizing particles in diamond.

Three scintillation counters along with two silicon P-I-N junction detectors [1] were used in the beam test (Figure 20). A trigger was formed by the coincidence of three scintillation counters and a silicon detector (S1·S2·S3·Si#1). The signals from the diamond detector and the silicon detector (Si#2) were averaged and recorded by a digital scope [2] (256 event averaging in a single sequence) and a CAMAC ADC. Sample signal pulses are shown in Figure 21.

Table 4: Charged particles in M13 beam line at TRIUMF.

Particle	m_0 (MeV/c^2)	p (MeV/c)	β	γ	$(\frac{dE}{dx})/(\frac{dE}{dx})_{MI}$
π^-	139.6	100	0.58	1.23	2.5
μ^-	105.7	100	0.71	1.42	1.7
e^-	0.51	100	0.99	7.09	1.0

[1] Hamamatsu S2506.

[2] Tektronics 2440.

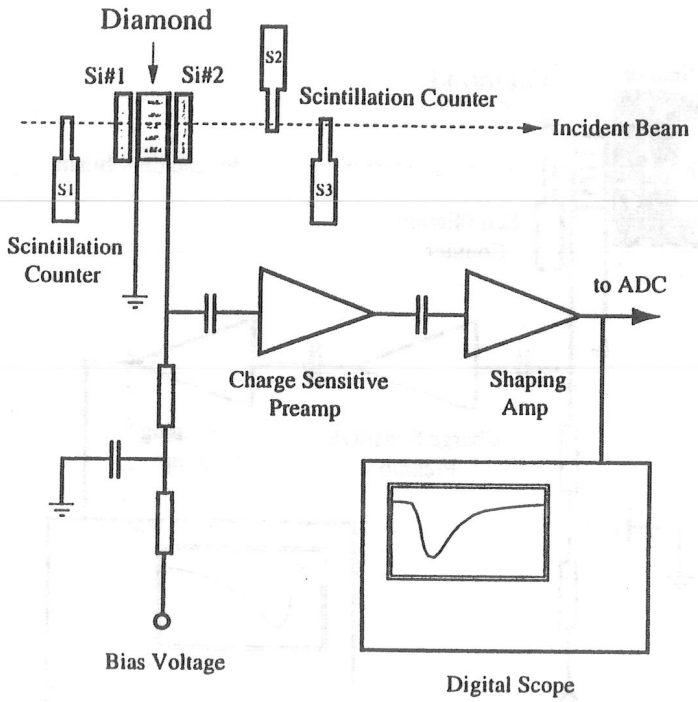

Figure 20: A schematic view of the experimental setup for the TRIUMF beam test. A trigger was formed by three scintillation trigger counters and a silicon detector (S1·S2·S3·Si#1).

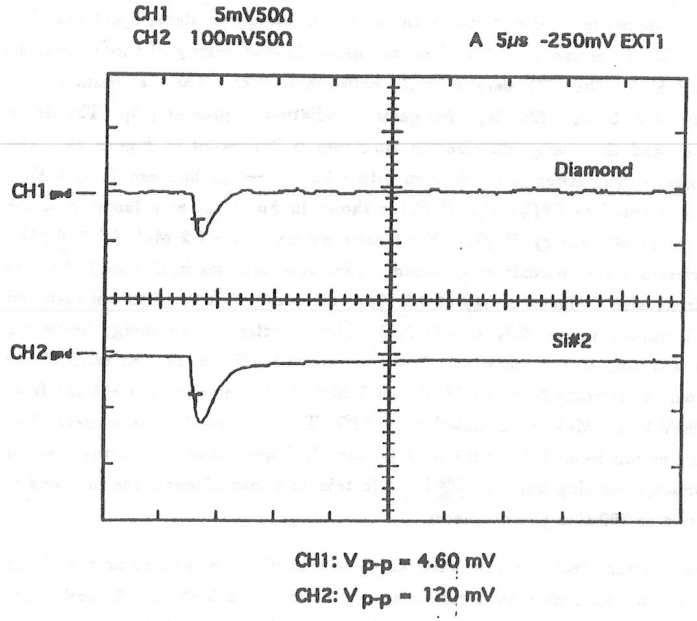

Figure 21: The upper scope trace is the signal from a natural diamond detector at a bias of 200 V averaged over 256 events. The lower trace is the average signal from the Si#2 detector.

3.1.2 Radioactive Source Measurement

The experimental setup for a radioactive source measurement is shown in Figure 22. A ^{90}Sr source produces electrons with continuous energy β^- decay spectrum. ^{90}Sr decays by β^- emission to ^{90}Y. The maximum kinetic energy of those electrons is 0.53 MeV. Then ^{90}Y decays by β^- emission to ^{90}Zr. The maximum kinetic energy is 2.28 MeV [28, 36]. No gamma radiation is present [36]. The decay scheme and the energy distribution spectrum is illustrated in Figure 23. The probability of emission of an electron with a kinetic energy between E_k and $E_k + dE_k$ is denoted as $P(E_k)dE_k$. $P(E_k)$ is shown in Figure 24 as a function of the electron kinetic energy E_k [36]. For kinetic energy above 1.2 MeV ($\beta \geq 0.957$), the electrons are approximately minimum ionizing particles in diamond. For the electrons with a kinetic energy of 0.5 MeV, the energy loss in a 500 μm diamond film is approximately $\Delta E_k \approx 0.35$ MeV. Thus, electrons with energy below 0.5 MeV will stop in the diamond. From the curve in Figure 24, the ratio of the number of electrons from 0.5 MeV to 1.2 MeV to the number of electrons from 0.5 MeV to 2.3 MeV is calculated to be 62%. Thus, the total average energy loss if an electron from Sr^{90} source may be slightly higher than the energy loss for a minimum ionizing particle, $\left(\frac{dE}{dx}\right)_{MI}$. To take this into account, the diamond is modeled as 500 thin (1 μm) pieces.

When electrons travel in the material, their velocities are reduced as they loose energy. For electrons with a kinetic energy between 0.5 MeV to 1.2 MeV, more energy is lost as they travel through the diamond because $\frac{dE}{dx}$ increases as the particle velocity decreases. The average energy loss for an electron with a kinetic energy of E_k in the 500 thin pieces of diamond is calculated by:

$$\overline{\left(\frac{dE}{dx}\right)} = \frac{1}{500}\sum_{i=1}^{500}\left(\frac{dE}{dx}\right)_i \qquad (3.1)$$

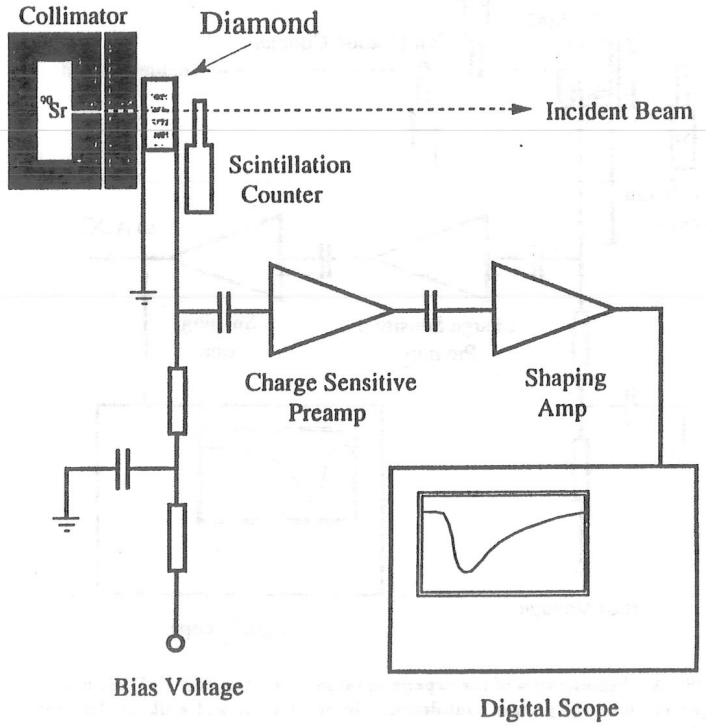

Figure 22: Setup for radioactive source-induced conductivity measurement. The electron beam is formed by two brass collimators between the ^{90}Sr source and diamond. A scintillation counter behind diamond triggers the digital scope.

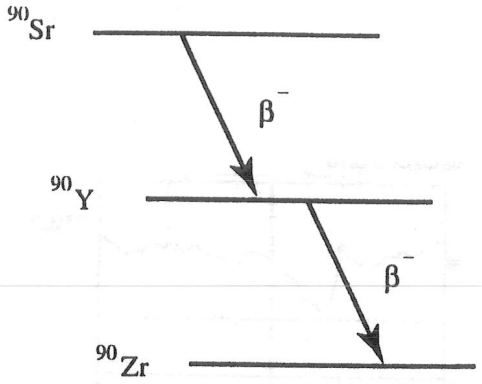

Figure 23: Decay scheme for ^{90}Sr and ^{90}Y.

where $\left(\frac{dE}{dx}\right)_i$ is the energy loss in the ith slice. The total energy loss for the electrons from the β-decay is then:

$$\begin{aligned}\left(\frac{dE}{dx}\right)_T &= \int_{0.5\,\mathrm{MeV}}^{2.3\,\mathrm{MeV}} \overline{\left(\frac{dE}{dx}\right)} P(E_k)\, dE_k \\ &= 1.99\ \mathrm{MeV cm^2 g^{-1}} \\ &= 1.08 \times \left(\frac{dE}{dx}\right)_{MI} \end{aligned} \tag{3.2}$$

This calculation indicates that the energy loss of electrons from Sr^{90} is 8% larger than minimum ionizing particles.

In order to form a well defined particle beam, two brass collimators with a total thickness of 30 mm were placed between the diamond detector and the radioactive source. The aperture size of the collimators is 2 mm. One scintillation counter was placed directly behind the diamond detector to trigger the acquisition system. The signals were averaged and recorded by a digital oscilloscope [3]. An analog

[3] TEKTRONICS TD540.

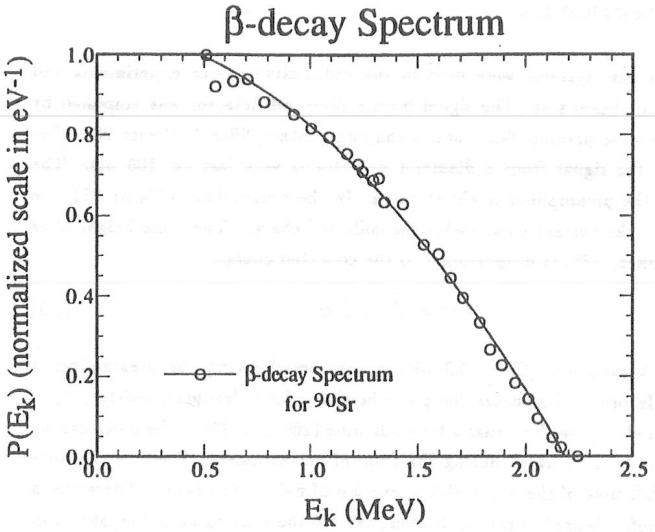

Figure 24: The energy spectrum of the β^- emission for ^{90}Sr radioactive source. $P(E_k)dE_k$ is the probability of emission of an electron with a kinetic energy between E_k and $E_k + dE_k$. The electrons with a kinetic energy larger than 1.2 MeV are minimum ionizing particles in diamond. The electrons with energy below 0.5 MeV will stop in diamond.

oscilloscope [4] was used to monitor the signals. Figure 25 shows the pulse traces from the digital scope in both single shot mode and averaging mode.

3.1.3 ELECTRONICS

Similar electronic systems were used in the radioactive source experiments and the accelerator beam test. The signal from a diamond detector was amplified by a charge sensitive preamplifier [5] and a shaping postamplifier [6] (Figure 26). The rise time of the signal from a diamond detector is very fast (< 100 ps). The rise time of the preamplifier is about 50 ns. In the preamplifier (Figure 27), the integration of the current pulse yields the collected charge. The pulse height after the preamplifier, V^{pre}, is proportional to the collected charge:

$$V^{pre} \propto \frac{1}{C_f} \int I \, dt \tag{3.3}$$

The feedback capacitor (C_f = 0.2 pF) is very small giving the preamplifier a large gain. In order to measure the pulse height, a large feedback resistor, R_f = 1.0 GΩ, is used to give the signal a long fall time (200 μs). Thus, the pulse can be approximated as a constant during the time of measurement. However, because of the long fall time of the preamplifier, overlap of pulses may occur. Therefore, a shaping amplifier is used to cancel this long tail. In the shaping amplifier, shown in Figure 27, a pole-zero filter (C_1/R_1) differentiates the signal from the preamplifier to obtain a pulse with faster falling time. However, by differentiating the falling part of the pulse, a negative tail occurs. This negative tail can be offset by using a parallel path (C_2/R_2) with a long time constant. An integrator after the pole-zero filtering network is used to increase the signal-to-noise ratio. All signals have the same shape after the shaping amplifier. In the radioactive source measurement, the shaping time of the postamplifier is 2.5 μs. The shaping time of the postamplifier used in the TRIUMF beam test is 0.8 μs.

[4] TEKTRONICS 2465.

[5] HIC-1576 from Digitex Laboratory Co., Ltd. Ref. [37].

[6] OSU-M475.

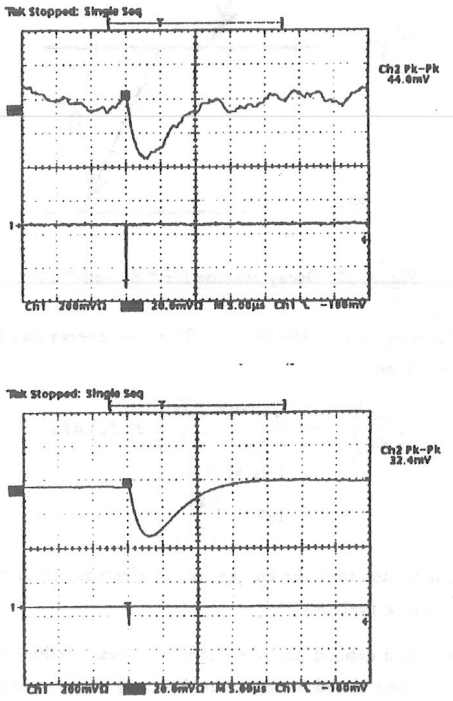

Figure 25: Scope traces of signals from a polycrystalline diamond at a bias of 300 V: (a) single shot signal; (b) an average over 5000 events. The lower trace in each diagram is the trigger pulse. The different shaping time used in the TRIUMF beam test shown in Figure 21 can be noticed.

By measuring the pulse height of the signal from the shaping amplifier, the number of charges induced on the electrodes, $Q_{\text{collected}}$, can be calculated. Since all signals have the same shape, the pulse height of the signal from the shaping amplifier, V_{PH}, is proportional to the charge collected on the electrodes of the detector. The proportional factor is the electronic gain G:

$$V_{\text{PH}} = \text{G} \times Q_{\text{collected}}$$

or (3.4)

$$Q_{\text{collected}} = \frac{V_{\text{PH}}}{\text{G}}$$

3.1.4 Electronic Gain

To determine the electronic gain, the output pulse height V_{PH} from the shaping amplifier and the input charge Q_{in} to the preamplifier were measured. A step pulse V_{pulse} from a pulse generator [7] was used to charge a test capacitor C_{test}. The input pulse on the test capacitor (Figure 26) is given by:

$$V_{\text{in}} = V_{\text{pulse}} \times \text{attenuation} \tag{3.5}$$

The attenuation was measured to be 0.0263 for a two stage Γ-type voltage divider. The charge on the test capacitor is $Q_{\text{in}} = V_{\text{in}} C_{\text{test}}$. The electronic gain is given by:

$$\begin{aligned} \text{G} &= \frac{V_{\text{PH}}}{Q_{\text{in}}} \\ &= \frac{V_{\text{PH}}}{V_{\text{in}}\, C_{\text{test}}} \\ &= \frac{V_{\text{PH}}}{(V_{\text{pulse}} \times \text{attenuation})\, C_{\text{test}}} \\ &= \frac{1}{0.0263} \times \frac{V_{\text{PH}}}{V_{\text{pulse}}\, C_{\text{test}}} \end{aligned} \tag{3.6}$$

The built-in test capacitor on the preamplifier circuit board is called C_0. To change the capacitance C_{test}, an external capacitor, C', was used in parallel to C_0. Thus,

[7] Hewlett Packard HP-8011A.

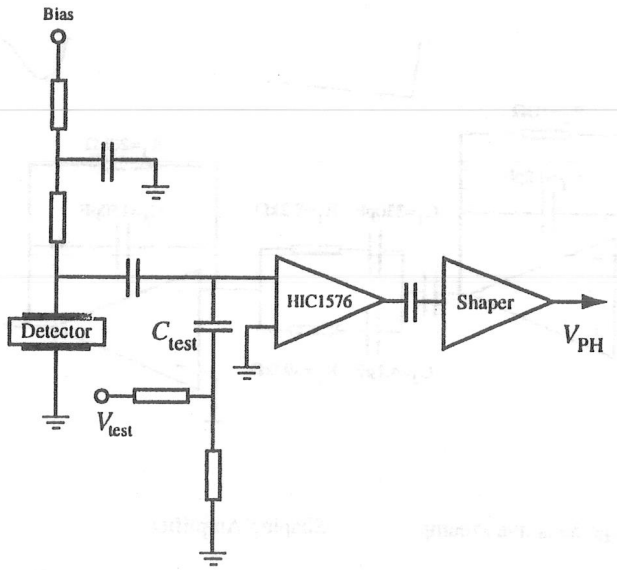

Figure 26: Schematic view of the electronics setup. A charge sensitive preamplifier and a shaping postamplifier are shown.

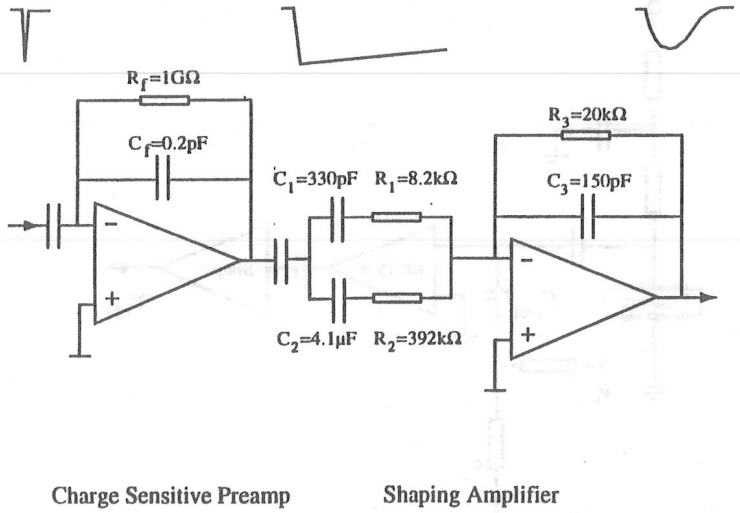

Figure 27: Detail of the preamplifier and shaping postamplifier circuits. The rise time of the signal from diamond detector is less than 100 ps. The rise time of the preamplifier is about 50 ns and the fall time is 200 μs. A long tail can be seen for the signal from the preamplifier. The shaping time of the shaping amplifier is 2.5 μs.

Table 5: Capacitance in the electronic gain measurements.

Capacitor	C' (pF)	$\Delta C'$ (pF)
"10pF"	9.4	1.2
"20pF"	17.2	1.4
"30pF"	27.4	1.8

the total test capacitance is equal to:

$$C_{test} = C' + C_0 \tag{3.7}$$

Three different capacitors C' were used with marked values of "10pF", "20pF" and "30pF". Their capacitances were measured. The mean values of C' are listed in Table 5. From a histogram of the deviation from the mean values, the error of the measurements can be estimated: $\sigma_s = 1.15$ pF. Another error introduced in the measurements is the meter accuracy, approximately 5% of C'. The total error in quadrature is given by:

$$\Delta C' = \sqrt{\sigma_s^2 + (5\%\ C')^2} \tag{3.8}$$

Eq. 3.6 can be rewritten as:

$$\begin{aligned} C_{test}(\text{pF}) &= C'(\text{pF}) + C_0(\text{pF}) \\ &= K(\text{pF}) \times \left(\frac{V_{PH}}{V_{pulse}}\right) \end{aligned} \tag{3.9}$$

where

$$K(\text{pF}) = \frac{1.6 \times 10^{-19}\ (\text{C/e})}{10^{-12}\ (\text{F/pF})} \times \frac{1}{0.0263} \times \frac{1}{\text{G (V/e)}} \tag{3.10}$$

By plotting V_{PH}/V_{pulse} verse C', K can be determined from the slope and then the electronic gain can be calculated. In Figure 28, the slope, K^{-1}, can be obtained by fitting the experimental results: $K^{-1} = 3.17$ pF^{-1}. Thus, G (volts per electron) can be derived from Eq. 3.10: G$= 1.93 \pm 0.08 \times 10^{-5}$ V/e.

The electronic gain has been measured frequently to ensure the stability of the electronic system. Figure 29 illustrates the electronic gain of the radioactive source setup as a function of time over a two year period.

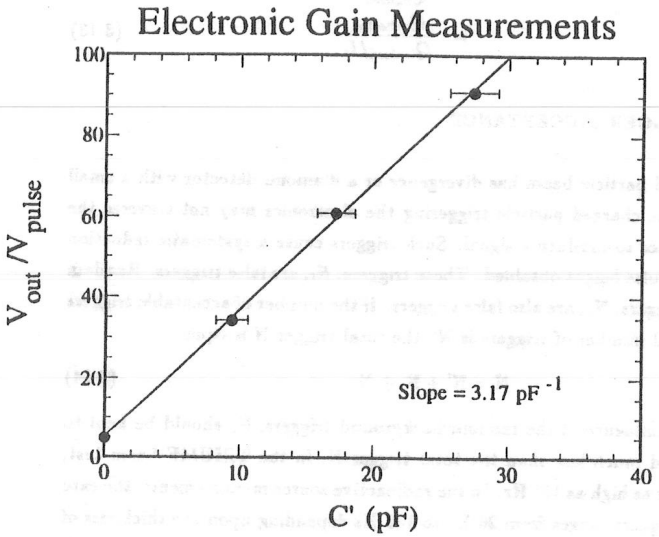

Figure 28: To determine the electronic gain, V_{PH}/V_{pulse} verses C' is plotted. G can be calculated from the slope.

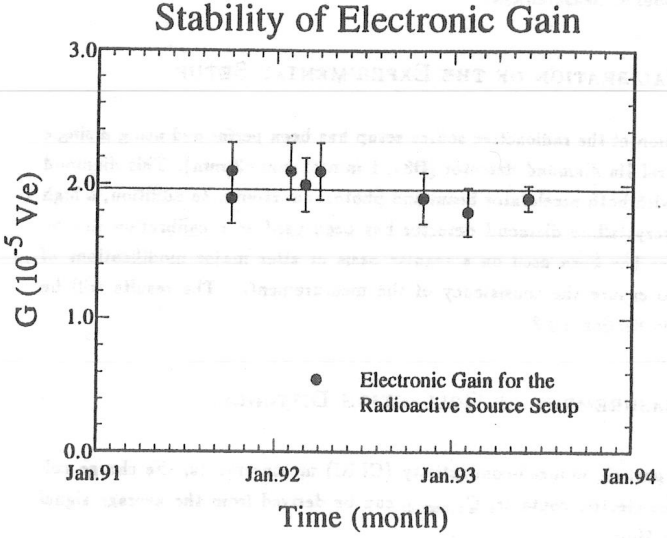

Figure 29: Plot exhibits the stability of the electronic gain over two years.

The gain of the electronics used in the TRIUMF beam test was measured to be $G^{Dia} = 0.77 \times 10^{-5}$ V/e for the diamond channel, $G^{Si\#1} = 0.69 \times 10^{-5}$ V/e for the Si#1 channel and $G^{Si\#2} = 0.67 \times 10^{-5}$ V/e for the Si#2 channel. The smaller gain is primarily due to the faster shaping time used in the TRIUMF beam test than that in the source measurement.

3.1.5 Calibration of the Experimental Setup

The calibration of the radioactive source setup has been performed using a single crystal natural IIa diamond detector (D34, 1 mm×1 mm×3 mm). This diamond was tested with both accelerator beam and photoconductivity. In addition, a high quality polycrystalline diamond detector has been used as a calibration device. This detector has been used on a regular basis or after major modifications of the setup to ensure the consistency of the measurements. The results will be introduced in Section 3.3.3.

3.2 Measurement of Collection Distance

In charged particle induced-conductivity (CPIC) measurements, the charge collected on the electric contacts, $Q_{collected}$, can be derived from the average signal pulse height V_{PH}:

$$Q_{collected} = \frac{V_{PH}}{G} \tag{3.11}$$

The average pulse height V_{PH} for N triggers is equal to:

$$V_{PH} = \frac{1}{N} \sum_{i=1}^{N} V_{PH}^{i} \tag{3.12}$$

where V_{PH}^{i} is the pulse height for the i^{th} trigger and V_{PH} can be measured by a digital scope in an averaging mode. Therefore, using Eq. 2.90, the measured collection distance can be evaluated:

$$\begin{aligned} d_{CPIC} &= \frac{Q_{collected}}{Q_{ionized}} L \\ &= \frac{Q_{collected}}{Q_{ionized}/L} \end{aligned} \tag{3.13}$$

3.2.1 Trigger Acceptance

When a charged particle beam has divergence or a diamond detector with a small area is used, the charged particle triggering the electronics may not traverse the diamond detector to produce a signal. Such triggers cause a systematic reduction of the average pulse height obtained. Those triggers, N_f, are false triggers. Random background triggers, N_b, are also false triggers. If the number of acceptable triggers among the total number of triggers is N′, the total trigger N is equal to:

$$N = N' + N_f + N_b \tag{3.14}$$

To reduce the influence of the random background triggers, N_b should be kept to a minimum and much less than the total trigger N. In the TRIUMF beam test, trigger rate was as high as 10^4 Hz. In the radioactive source measurements, the rate of the beam triggers ranges from 20 Hz to 100 Hz depending upon the thickness of the diamond film. The rate of background random triggers is about 1 Hz. Thus, the background triggers are negligible.

When the signal pulses are averaged, false triggers lead to systematic reduction of the average pulse height and to an inaccurate result. They must be taken into account. A trigger acceptance factor, a, is used to calculate the average pulse height for N′ acceptable triggers:

$$a = \frac{N'}{N} \tag{3.15}$$

Figure 30 illustrates the geometry for the triggering detectors and diamond detector in the TRIUMF beam test. The false triggers caused by beam divergency are

shown. From a beam Monte Carlo calculation for M13 beam line at TRIUMF, the trigger ratio of the Si#2 detector to the Si#1 detector (Figure 20) is equal to 0.85 due to the beam divergency [38]. This calculation means that the trigger acceptance factor for the Si#2 detector is equal to $a_d^{Si\#2} = 0.85$. Because the diamond detector was located halfway between the two silicon detectors, the trigger acceptance factor for diamond detector can be calculated by a linear extrapolation: $a_d^{Dia} = 0.92$.

The other factor causing false triggers is a smaller detector area. Because the area of the Si#1 ($A^{Si\#1}$) is equal to the area of the Si#2 ($A^{Si\#2}$), the trigger acceptance factor for the Si#2, $a_a^{Si\#2}$, is equal to unity. The trigger acceptance factor for a diamond detector with small area, A^{Dia}, is equal to:

$$a_a^{Dia} = \frac{A^{Dia}}{A^{Si\#1}} \tag{3.16}$$

When $A^{Dia} > A^{Si\#1}$, $a_a^{Dia} = 1$. The total trigger acceptance factor is equal to:

$$a = a_d \times a_a \tag{3.17}$$

The trigger acceptance factors for the Si#1 detector, the Si#2 detector and the diamond detector are listed in Table 6. Therefore, the collection distance d_{CPIC} calculated from the average pulse height is equal to:

$$d_{CPIC} = \frac{1}{a} \times \frac{Q_{collected}}{Q_{ionized}/L} \tag{3.18}$$

In radioactive source measurements, the beam size is smaller than the size of diamond detector and the scintillation trigger counter. In addition, the the distance between the collimator and diamond detector and the distance between diamond detector and the scintillator were kept very small (see Figure 31 and Table 7). Several sets of x-y-z translation stages allows to adjust the relative positions of the source, collimators, diamond detector and the scintillator in order to obtain an optimum alignment of the system. When the system is well aligned, the trigger acceptance factor for diamond detector is equal to unity.

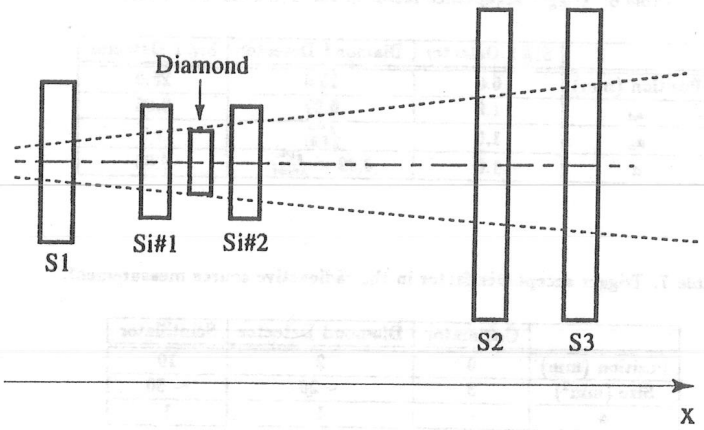

Positions:
End of Beam Pipe, x=0 mm
S1: Scintillation Counter #1, x=28 mm
S2: Scintillation Counter #2, x=440 mm
S3: Scintillation Counter #3, x=535 mm
Si#1: Silicon Detector #1, x=204 mm
Si#2: Silicon Detector #2, x=230 mm
Diamond Detector, x= 217 mm

Figure 30: A geometric diagram showing the false triggers caused by the beam divergency. A cone shape beam due to the beam divergency can be seen. The triggers formed by the particles outside the cone are false triggers.

Table 6: Trigger acceptance factor in the TRIUMF beam test.

	Si#1 Detector	Diamond Detector	Si#1 Detector
Position (mm)	0.0	13.0	26.0
a_d	1.0	0.92	0.85
a_a	1.0	$\frac{A^{Dia}}{A^{Si\#1}}$	1.0
a	1.0	$0.92 \times \frac{A^{Dia}}{A^{Si\#1}}$	0.85

Table 7: Trigger acceptance factor in the radioactive source measurement.

	Collimator	Diamond Detector	Scintillator
Position (mm)	0	2	10
Size (mm^2)	3	~ 20	~ 50
a	–	1	1

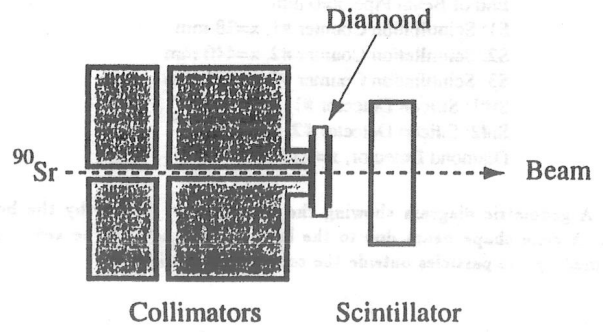

Figure 31: A geometric diagram in the radioactive source measurement. The small aperture size of the collimators limits the beam divergency.

3.2.2 Electron-Hole Pair Generation in Diamond

Measurement from the TRIUMF beam test

The number of electron hole pairs per unit length (Q_{ionized}/L) in diamond can be calculated using Bethe-Bloch equation (Eq. 2.1) [8].The energy loss in diamond for a minimum ionizing particle is $\frac{dE}{dx} = 1.84$ MeV cm^{2}g^{-1}. Using the density of diamond and the energy needed to generate one electron-hole pair in diamond ($E_{\text{pair}} = 13$ eV), the number of excess carrier per unit length generated by a minimum ionizing particle can be calculated for bulk diamond:

$$\begin{aligned} \frac{Q^{\text{Dia}}_{\text{ionized}}}{L} &= \frac{\rho_m \frac{dE}{dx}}{E_{\text{pair}}} \\ &= \frac{3.52 \text{ g cm}^{-3} \times 1.84 \text{ MeV cm}^2\text{g}^{-1}}{13 \text{ eV/pair}} \\ &= 49.8 \text{ pairs}/\mu\text{m} \end{aligned} \tag{3.20}$$

Similar calculations can be carried out for bulk silicon:

$$\frac{Q^{\text{Si}}_{\text{ionized}}}{L} = 107.0 \text{ pairs}/\mu\text{m}. \tag{3.21}$$

[8]Bremsstrahlung effect can be ignored in the radioactive source experiments because in diamond $E_{crit} \approx 130$ MeV which gives:

$$\begin{aligned} \frac{(\frac{dE}{dx})|_{\text{rad}}}{(\frac{dE}{dx})|_{\text{Coulomb}}} &\approx \frac{E_1}{130 \text{ MeV}} \\ &\leq \frac{2.28 \text{ MeV}}{130 \text{ MeV}} \\ &\approx 1.8\% \end{aligned} \tag{3.19}$$

Therefore, the mechanism of the energy loss is dominated by Coulomb interaction.

On the other hand, $Q^{Si}_{ionized}/L$ was determined experimentally. Figure 32 exhibits a histogram for signal pulse height from a silicon detector (the Si#2 detector in Figure 20) in response to pions. The average pulse height is equal to $V_{PH} = 122 \pm 12$ mV from a Gaussian fit for the 605 acquisitions. The electronic gain for the Si#2 channel is $G^{Si\#2} = 0.67 \times 10^{-5}$ V/e. Considering that the trigger acceptance factor a for the Si#2 detector is 0.85 and the normalization factor to minimum ionizing particles is 2.5, $Q^{Si}_{ionized}$ in silicon can be calculated from Eq. 3.4:

$$\begin{aligned} Q^{Si}_{ionized} &= \frac{1}{0.85} \times \frac{V_{PH}}{2.5 \times G^{Si\#2}} \\ &= 8569 \text{ pairs} \end{aligned} \tag{3.22}$$

The length of the depletion region, L, can be derived from the junction capacitance of the silicon detector. The junction capacitance was extrapolated from the plot of junction capacitance as a function of the reverse bias [39]. At a reverse bias of 30 V, $C_j = 7.7$ pF. The junction area, $A^{Si\#2}$, is equal to 0.277 cm$\times$ 0.277 cm from the technical data sheet (HAMAMATSU, INC) [39]:

$$C_j = \frac{\epsilon \epsilon_0 A^{Si\#2}}{L} \tag{3.23}$$

where ϵ is the dielectric constant of silicon and ϵ_0 is the permittivity of free space. The calculated length of the depletion region is equal to $L = 106 \pm 5$ μm [9].

Hence, the number of excess carriers per unit length in the silicon can be calculated using the total number of excess carriers, $Q^{Si}_{ionized}$, and the length of the depletion region L. Therefore, the experimental result for the number of excess carriers per unit length is equal to:

$$\frac{Q^{Si}_{ionized}}{L} = 81 \pm 9 \text{ pairs}/\mu m \tag{3.24}$$

The value of (107 pairs/μm) calculated from Bethe-Bloch theory is based on converting all the energy lost by a charged particle into the generation of electron-hole pairs. For a material with a large thickness, all the energy lost by a charged particle is contained in the material. For a thin film, some of the energy lost by the

[9] The length of the depletion region given by the manufacturer is 100 μm.

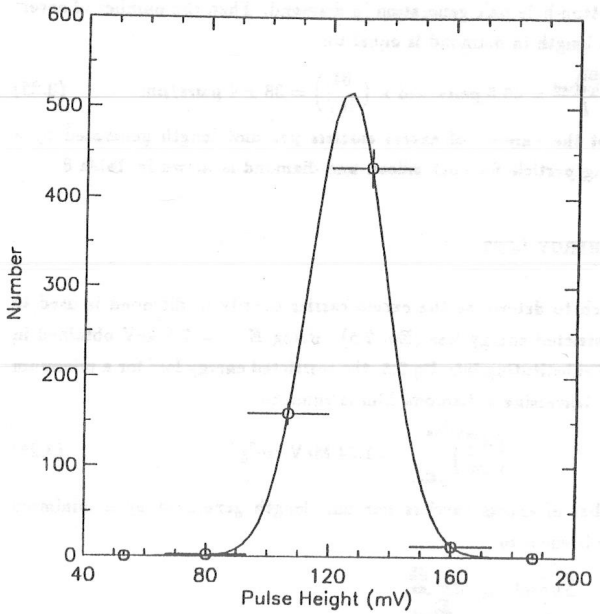

Figure 32: Pulse height distribution of silicon detector for 605 pion events in the TRIUMF beam test. The mean value is 122 $\pm$ 12 mV, which are obtained from a Gaussian fit shown by the solid line.

charged particle may escape the material. A calculation of the energy deposition in a thin film using the restricted energy loss will be discussed later.

From the measurement for the Si#2 detector, the ratio of the energy generated the excess electron-hole pairs to the total energy loss is equal to $\left(\frac{81}{107}\right)$. Same ratio is used for the electron-hole pair generation in diamond. Then the number of excess carriers per unit length in diamond is equal to:

$$\frac{Q^{\rm Dia}_{\rm ionized}}{L} = 49.8 \text{ pairs}/\mu\text{m} \times \left(\frac{81}{107}\right) = 38 \pm 4 \text{ pairs}/\mu\text{m} \qquad (3.25)$$

A comparison of the number of excess carriers per unit length generated by a minimum ionizing particle for both silicon and diamond is shown in Table 8.

RESTRICTED ENERGY LOSS

Another approach to determine the excess carrier density in diamond is used to calculate the restricted energy loss (Eq. 2.5). Using $E_{\rm max} = 7.5$ keV obtained in Chapter II and substituting into Eq 2.5, the restricted energy loss for a minimum ionizing particle traversing a diamond film is equal to:

$$-\left(\frac{dE}{dx}\right)^{\rm Dia}_{\leq E_{\rm max}} = 1.34 \text{ MeV cm}^2\text{g}^{-1} \qquad (3.26)$$

Then, the number of excess carriers per unit length generated by a minimum ionizing particle is equal to:

$$\begin{aligned} \frac{Q^{\rm Dia}_{\rm ionized}}{L} &= \frac{\rho_{\rm m} \frac{dE}{dx}}{E_{\rm pair}} \\ &= \frac{3.52 \text{ g cm}^{-3} \times 1.34 \text{ MeV cm}^2\text{g}^{-1}}{13 \text{ eV/pair}} \\ &\approx 36.3 \text{ pairs}/\mu\text{m} \end{aligned} \qquad (3.27)$$

Using the same calculations for the Si#2 detector, the restricted energy loss for pions traversing silicon film is equal to:

$$-\left(\frac{dE}{dx}\right)^{\rm Si}_{\leq E_{\rm max}} = 3.21 \text{ MeV cm}^2\text{g}^{-1} \qquad (3.28)$$

Table 8: Electron-hole pair generation in diamond and silicon. Comparisons are shown for the experimental values and the calculated values from the restricted energy loss (r.e.l).

	$E_{\rm pair}$ (eV)	$Q^{\rm exp.}_{\rm ionized}/L$ (pairs/μm)	$Q^{\rm r.e.l.}_{\rm ionized}/L$ (pairs/μm)
Silicon	3.6	81±9	80.2
Diamond	13	38±4	36.3

Thus, the number of excess carriers per unit length in silicon generated by a minimum ionizing particle is equal to:

$$\frac{Q^{\rm Si}_{\rm ionized}}{L} = 80.2 \text{ pairs}/\mu\text{m} \qquad (3.29)$$

The experimental results of the excess carrier density generated by a charged particle agree with the calculations from the theory of the restricted energy loss.

3.2.3 PEDESTAL ANALYSIS

In order to measure the signal size and the electronic noise of the system, the pulse height spectrum was recorded using a multichannel analyzer [10]. A gate width of 10 μsec was used to encompass the signal pulse. Figure 33 shows the experimental setup for the pulse height analysis. The electronic system was triggered by a pulse generator instead of the trigger counter. Figure 34 shows (a) the "raw" pulse height spectra when a 400 V bias was applied; (b) the pedestal spectrum when bias on diamond was 400 V; (c) the pulse height spectrum after the pedestal subtraction from the "raw" spectra.

The signal-to-noise ratio (S/N) is calculated as:

$$\begin{aligned} \text{S/N} &= \frac{V^{\rm p}_{\rm dia} - V^{\rm p}_{\rm ped}}{\sigma_{\rm ped}} \\ &= 3.7 \end{aligned} \qquad (3.30)$$

[10] CANBERRA-35 multichannel analyser.

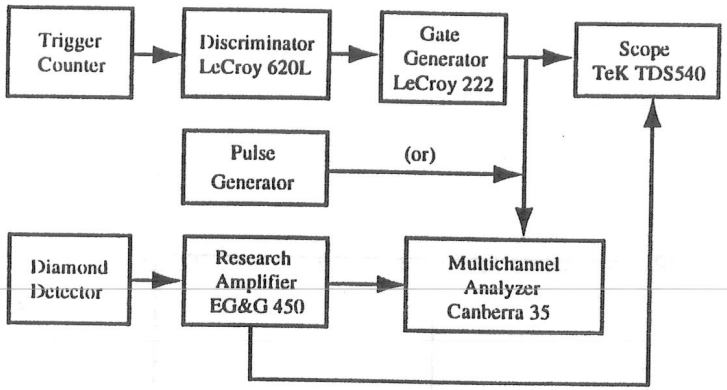

Figure 33: Experimental setup for pulse height spectrum analysis.

where σ_{ped} is the width of the pedestal spectrum; V^P_{dia} is the peak pulse height from the diamond detector; and V^P_{ped} is the peak pulse height of pedestal. A clear signal is evident. Although this method yields all the information desired, it is time consuming. Thus, a different method was used in the CPIC measurements.

In the CPIC measurements, the collected charge on the electric contacts were measured using the pulse height of the average signals. *Peak-to-peak* value of the average pulse was used for V_{PH}. At zero bias, noise gives a non-zero *peak-to-peak* background value, V_b, for a finite number of events. For an average over N events, the background voltage is equal to:

$$V_b \propto \frac{1}{\sqrt{N}} \tag{3.31}$$

To calculate the charge collected at the electric contacts, this background voltage should be subtracted from the "raw" *peak-to-peak* pulse height V_{PH} at each bias.

To determine this background voltage, a histogram of pulse height at zero bias on diamond detector is plotted in Figure 35. The mean value of the background voltage (V_b) and the deviation (σ_b) can be determined. Then, the pulse height

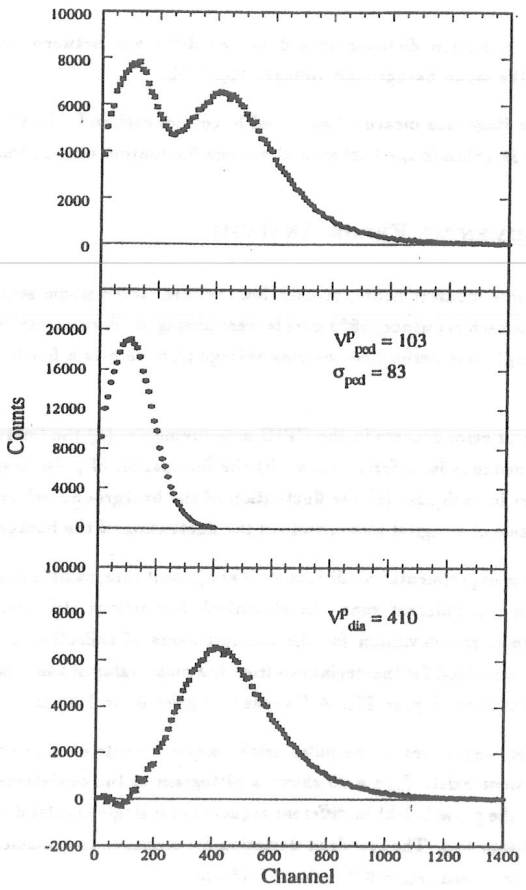

Figure 34: Pulse height spectrum of polycrystalline diamond detector: (a) the "raw" pulse height spectra when a 400 V bias is applied; (b) pedestal spectrum when bias on diamond is 400 V; (c) the pulse height spectrum after the pedestal subtraction from the "raw" spectra.

used to calculate collection distance should be the difference between the raw pulse height and the mean background voltage: $V_{\rm PH} - V_{\rm b}$.

The background voltage was measured and used to correct each pulse height measurement. Figure 36 exhibits the background voltage fluctuation over 15 months.

3.2.4 Experimental Error Analysis

In radioactive source measurements, at each bias voltage, three single sequences were measured. In each sequence, 5000 events were averaged. A complete run for each diamond sample was performed covering voltage from zero to a few hundred volts.

There are five major error sources in the CPIC measurements: (a) the fluctuation of the collection distance in different runs, (b) the fluctuation of pulse height in different sequences in each run, (c) the fluctuation of the background voltage, (d) the digitization scale of a digital scope, and (e) the fluctuation of the background.

(a) Even though the experimental conditions such as incident rate, sample positions were kept the same in different runs, the statistical fluctuations still exist. To determine the *run-to-run* deviation for the measurements of collection distance ($\sigma_{\rm rr}$), a histogram is plotted for the deviations from the mean value of the collection distance in different runs (Figure 37). A Gaussian fit gives $\sigma_{\rm rr} = 1.3$ μm.

(b) For the different sequences in the pulse height measurements at each voltage, statistical fluctuations exist. Figure 38 shows a histogram of the deviations from the mean value of the pulse height in different sequences for single crystal diamond in the TRIUMF beam test. The standard deviation for *sequence-to-sequence* fluctuation can be determined: $\sigma_{\rm ss} = 0.31$ mV or 0.43 μm.

(c) Background noise fluctuation introduces error when the background voltage is deduced from the raw pulse height. The standard deviation ($\sigma_{\rm b}$) can be obtained from the histogram shown in Section 3.2.3. A typical value of the fluctuation is equal to $\sigma_{\rm b} = 0.08$ mV or 0.11 μm.

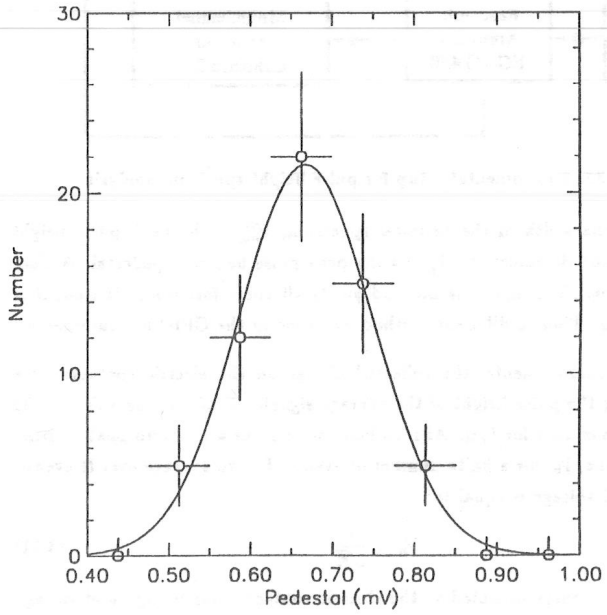

Figure 35: Background voltage distribution. The average background voltage is equal to $V_{\rm b} = 0.67 \pm 0.08$ mV from a Gaussian fit.

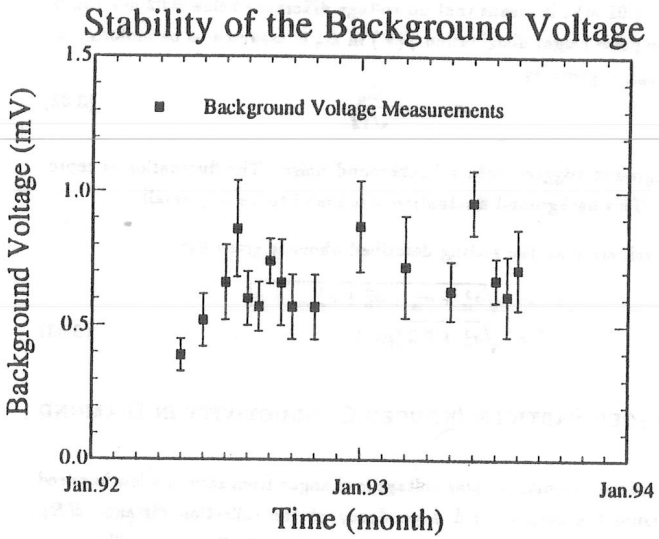

Figure 36: The background voltage stability over 15 months.

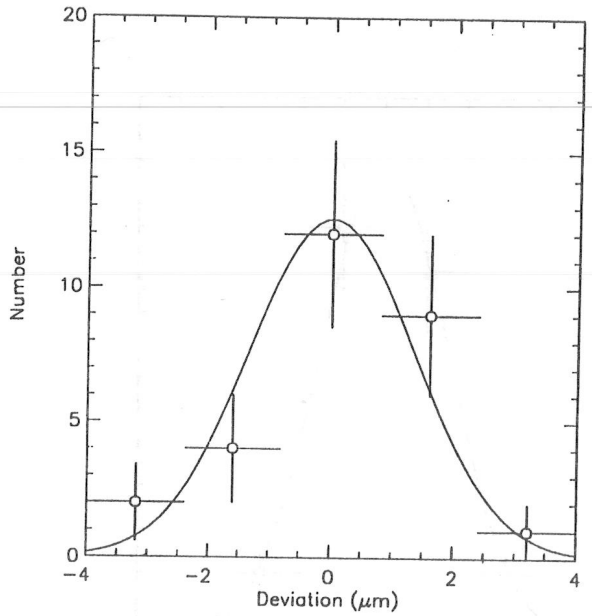

Figure 37: Deviation for *run-to-run* fluctuation at an electric field of 10 kV cm^{-1}. The solid line is a Gaussian fit where σ_{rr} can be determined.

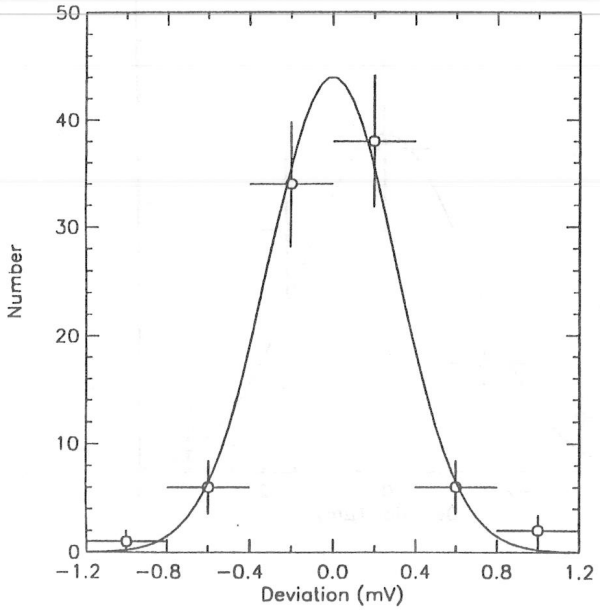

Figure 38: Deviation for *sequence-to-sequence* fluctuation. The solid line is a Gaussian fit where σ_{ss} can be determined.

(d) The digitization of the digital scope gives error in the pulse height measurements. The digitization, Δ_q, depends on the chosen scope range. For example, when a range of 20 mV/div is used in TEKTRONICS TD540, the digitization is equal to $\Delta_q = 0.02$ mV. It means that no voltage difference below 0.02 mV can be recorded. The pulse height distribution $f(V)$ in Δ_q is assumed to be uniform, the deviation, σ_{scope}, is given by:

$$\sigma_{scope} = \frac{\Delta_q}{\sqrt{12}} \tag{3.32}$$

(e) The background triggers yield a background noise. The fluctuation is represented by σ_b. This background fluctuation was found to be very small.

A typical overall error for the setting described above is given by:

$$\begin{aligned} \sigma &= \sqrt{\sigma_{rr}^2 + \sigma_{ss}^2 + \sigma_b^2 + \sigma_{scope}^2 + \sigma_b^2} \\ &= \sqrt{\sigma_{rr}^2 + 0.2}\ (\mu\text{m}) \end{aligned} \tag{3.33}$$

3.3 CHARGED PARTICLE-INDUCED CONDUCTIVITY IN DIAMOND

In the CPIC measurements, the bias voltage is changed from zero to a few hundred volts to measure the electric field dependency of the collection distance $d(E)$. Both single crystal natural diamond and polycrystalline CVD diamond films were measured.

3.3.1 SINGLE CRYSTAL DIAMOND

In the TRIUMF beam test, the response of single crystal natural IIa diamond radiation detector (D34) to pions (π's), muons (μ's) and electrons (e's) was tested and analyzed.

Figure 39 shows the pulse height as a function of bias voltage for a single crystal diamond (D34, 1 mm×1 mm×3 mm) in response to pions, muons and electrons. The apparent steps in the pulse hight measurements are due to a small number of

events in the average (256 events) and a coarse scope setting (σ_{scope} = 2 mV for a setting of 20 mV/div). Normalizing the pulse height for different charged particles to minimum ionization particles, Figure 40 illustrates the averaged collection distance deduced from the pulses from the particles. At an electric field up to 25 kV cm^{-1}, no saturation of pulse height is observed. This indicates no saturation of the carrier drift velocity up to this electric field. In addition, no internal breakdown has occurred up to this electric field.

The same detector (D34) used at the TRIUMF beam test was measured in the radioactive source induced conductivity test. The consistency between the beam test and the source test is shown in Figure 41.

3.3.2 Polycrystalline Diamond

The quality of the polycrystalline diamonds varies from wafer to wafer. Different growth processes, different growth parameters and different post-growth processing may give quite different electrical properties and detector response.

Signals were detected at the TRIUMF beam test (Figure 42) from the detectors made by polycrystalline diamond films grown in 1990. This was the first demonstration that polycrystalline diamond could be used in radiation detection. The collection distance of the best diamonds at that time was about 10 μm at an electric field of 10 kV cm^{-1}, three times less than that of single crystal diamond.

The collection distance of the polycrystalline diamond films grown in the last year was over 40 μm. At low electric field, the collection distance is comparable to or even exceeds that of single crystal diamond (Figure 43).

3.3.3 Stability of Collection Distance Measurement

A high quality polycrystalline diamond has been used over a long period of time to calibrate the radioactive source system. Figure 44 illustrates the consistency of

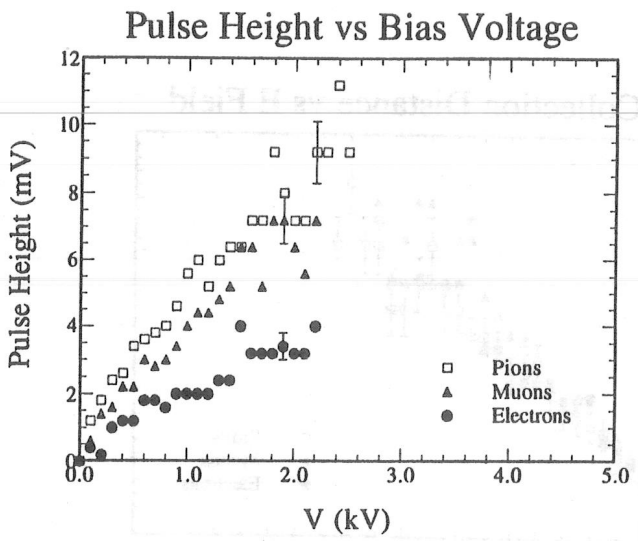

Figure 39: Pulse height as function of bias for a single crystal diamond detector (D34) in the TRIUMF beam test. Typical errors are shown.

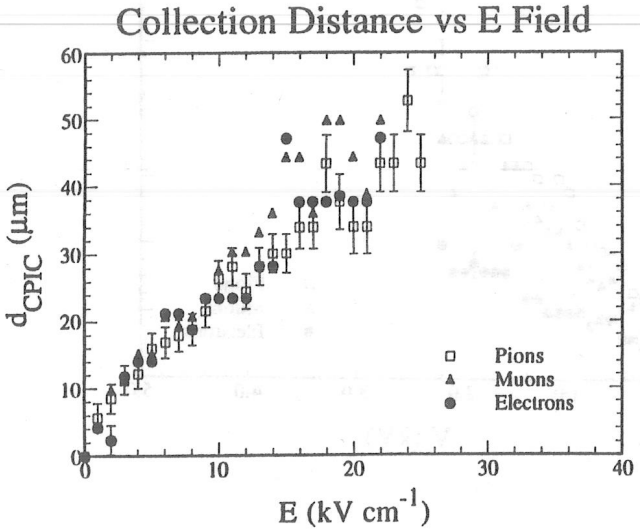

Figure 40: Collection distance as a function of electric field for a single crystal diamond detector (D34) in the TRIUMF beam test. Normalized signals from pions, muons and electrons to minimum ionizing particles.

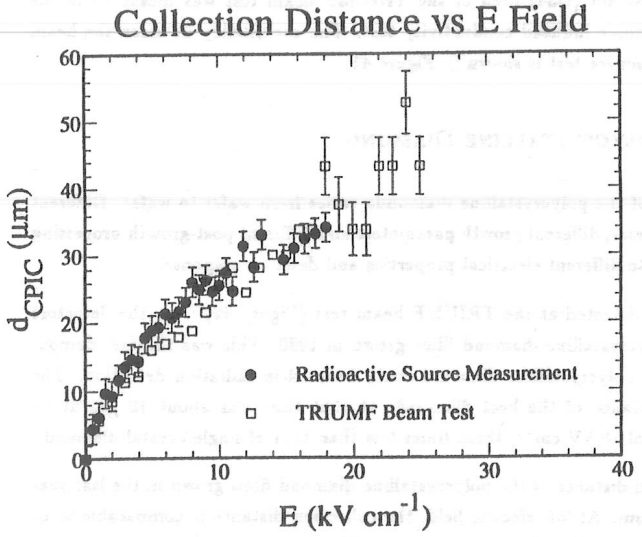

Figure 41: Collection distance versus electric field for a single crystal diamond detector (D34) in radioactive source measurement.

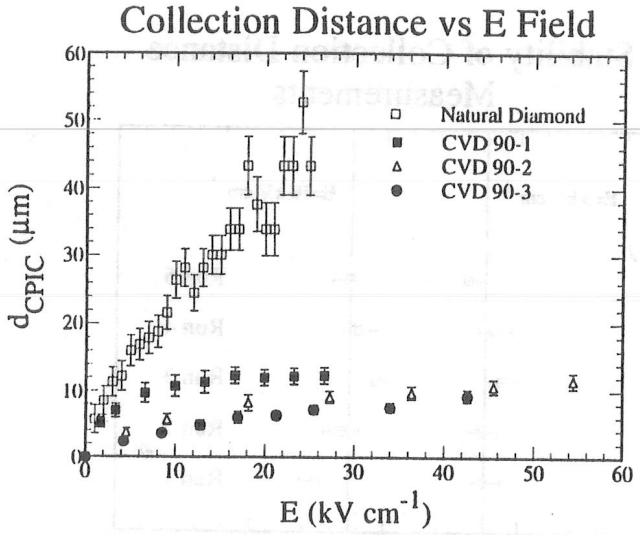

Figure 42: Collection distance of polycrystalline diamond in the TRIUMF beam test. Collection distance of a single crystal diamond (D34) is plotted as a comparison.

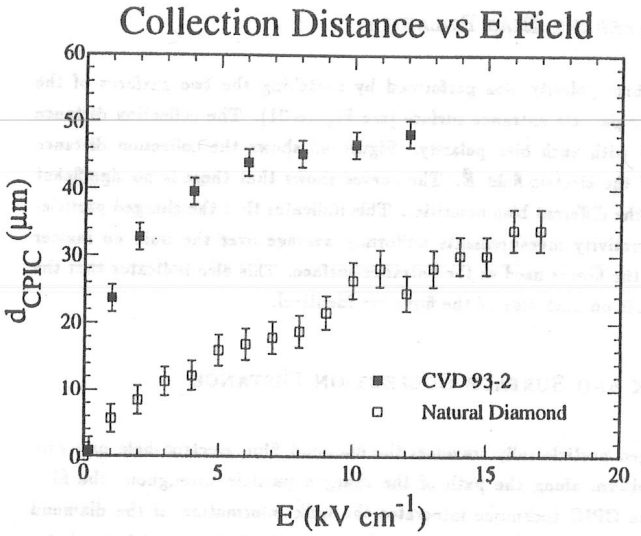

Figure 43: Collection Distance of recent polycrystalline diamond measured by the CPIC. The collection distance of a single crystal diamond (D34) is also shown.

the measurements of collection distance at a low electric field (E = 3 kV cm^{-1}) and a higher field (E = 10 kV cm^{-1}).

3.3.4 Different Bias Polarity

A change of bias polarity was performed by switching the two surfaces of the detector as the particle entrance surface (see Figure 31). The collection distance was measured with each bias polarity. Figure 45 shows the collection distance as function of the electric field $\vec{E}$. The curves shows that there is no significant difference for the different bias polarities. This indicates that the charged particle-induced conductivity measurements uniformly average over the bulk no matter which side of the film is used as the entrance surface. This also indicates that the electric contacts on both side of the films are identical.

3.4 Bulk and Surface Collection Distance

Since a charged particle fully traverses the diamond film, electron-hole pair production is uniform along the path of the charged particle throughout the film. Therefore, the CPIC technique integrates the bulk information of the diamond film. The measured collection distance averages over the bulk material. In photo-induced conductivity studies (Figure 46), the absorption depth (1/e) for the photon of 6.1 eV is about 1 $\sim$ 2 μm, the electron hole pair generation occurs in a region near the surfaces of a diamond film. Therefore, the PIC technique delivers information near the surface of the diamond film.

3.4.1 Single Crystal Diamond

From the transient photo-induced conductivity experiment at Stanford Synchrotron Radiation Laboratory (SSRL) [40], the field dependent collection distance for detector D34 was measured. A agreement between the CPIC and the PIC measure-

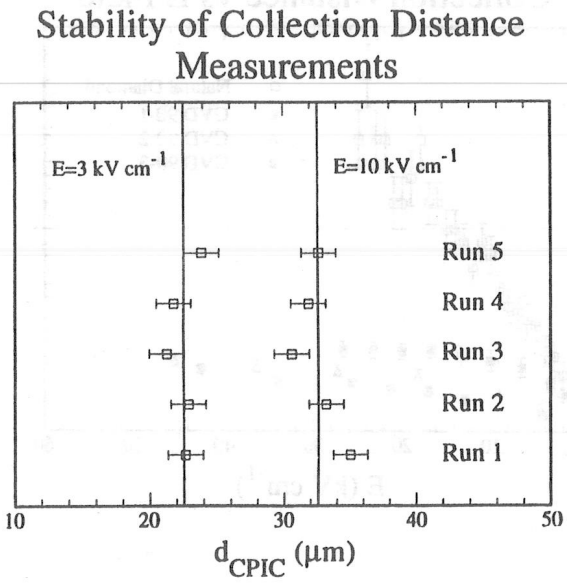

Figure 44: Stability of the measurements of collection distance. The consistency of the measurement for a diamond sample over a period of several months at both low and high electric field.

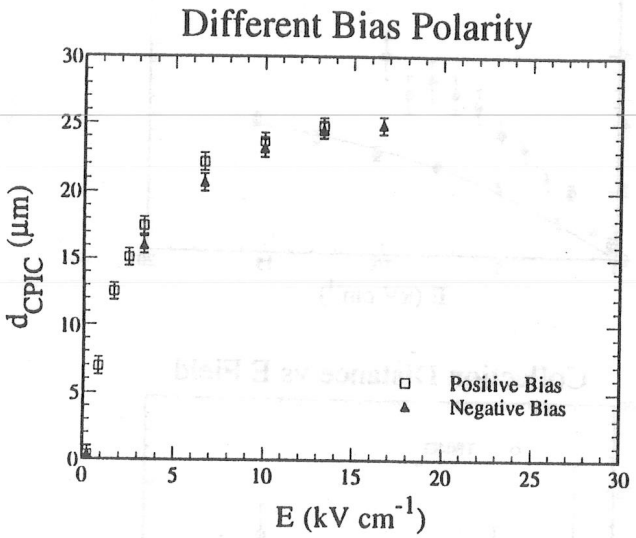

Figure 45: Collection distance with different bias polarity for a polycrystalline diamond detector. No obvious difference can be seen.

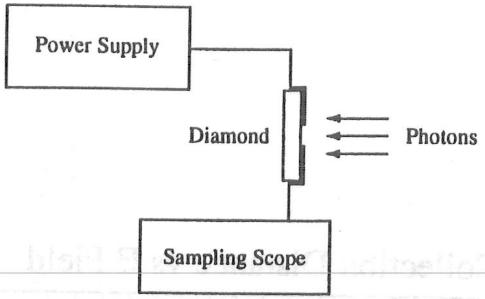

Figure 46: Photo-induced conductivity measurement.

ments is shown in Figure 47. This agreement indicates uniform electrical properties throughout the single crystal diamond from the bulk to the surface. This is consistent with the result of Eq. 2.91, the theoretical analysis in Chapter II.

3.4.2 Polycrystalline Diamond

Unlike single crystal diamond, for polycrystalline diamond, the results from the CPIC measurements and the PIC measurements were found to be different. From Figure 48, it is clear that the bulk measurement differs from the surface measurement and that d_{CPIC}/d_{PIC} is approximately equal to 0.5 and independent of electric field strength E. This result led us to pursue the hypothesis that the crystal quality of the polycrystalline diamond increases with the film thickness along the columnar direction of the film [41] resulting in a corresponding change of electric properties along the columnar direction. In the other words, a gradient of the electrical properties in the columnar direction exists. As a consequence of this gradient, different results may be obtained if the experimental techniques probe different portions of the polycrystalline film.

In Figure 49, d_{CPIC}, the average value throughout the bulk along the columnar direction, is plotted as a function of d_{PIC}, the surface value at the growth side of the

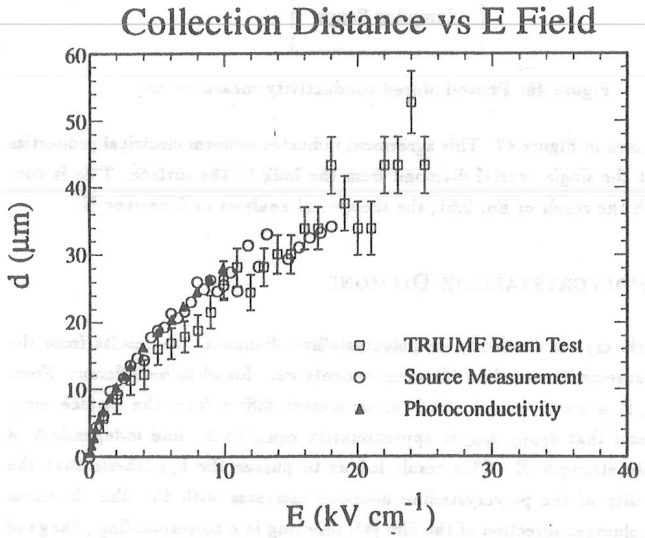

Figure 47: Bulk and surface collection distance of a natural IIa single crystal diamond (D34).

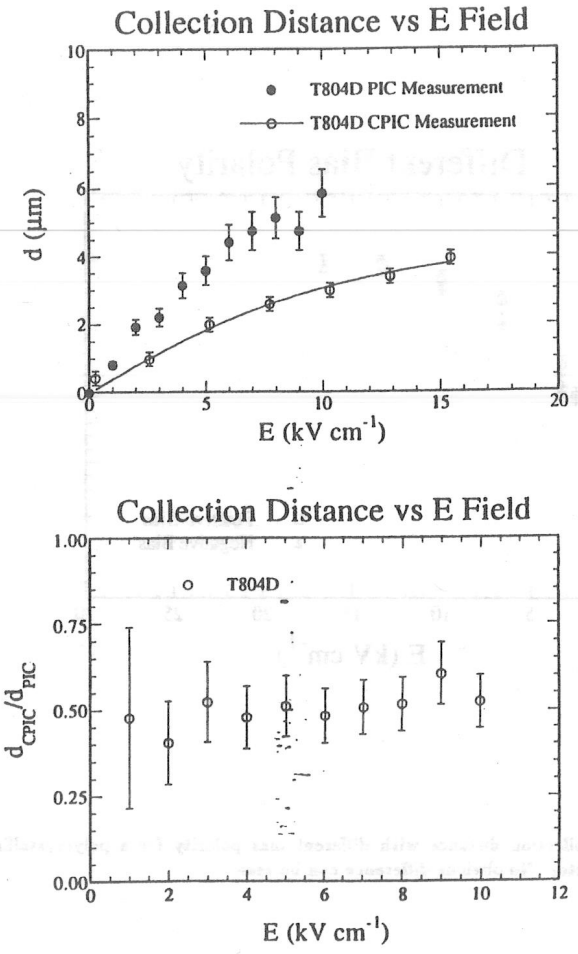

Figure 48: Difference between the CPIC and the PIC measurements for a CVD diamond. d_{PIC} was found to be larger than d_{CPIC} (upper plot). The lower plot shows the ratio of d_{CPIC}/d_{PIC} as a function of electric field E. d_{CPIC} is extrapolated from the curve in the upper plot fitting the experimental results. $d_{CPIC}/d_{PIC} \approx 0.5$.

films. Figure 49 shows that for polycrystalline diamond film, the collection distance averaged over the bulk of the material is not equal to the collection distance near the surface of the material. This implies that the collection distance is not a constant along the columnar direction. A weighted fit of the data yields $d_{CPIC} = (0.51 \pm 0.07)\ d_{PIC}$.

From the discussion in Chapter II, the collection distance from the CPIC measurement is equal to the average value of the collection distances at the two surfaces of the film (Eq. 2.61):

$$d_{CPIC} = \frac{d_g + d_s}{2} \tag{3.34}$$

For unpolished samples, the PIC measurements show that the collection distance at the substrate side of the polycrystalline diamond films is very small ($d_s \approx 0.1\ \mu m$) compared with that of growth side of the film. In the other words, the collection distance from the CPIC measurements for polycrystalline diamonds, d_{CPIC}, is equal to half of the collection distance at the growth side of the film determined from the PIC measurements d_{PIC}.

When the quality of the polycrystalline diamond films improves, the collection distance should increase. In Figure 50, d_{CPIC} is plotted against d_{PIC} for the samples with high collection distance and the samples shown in Figure 49. $d_{CPIC} = 0.5\ d_{PIC}$ still holds for the samples with large collection distance samples.

The gradient of the collection distance along the columnar direction was demonstrated by measuring the collection distance depth profile $d(x)$ where x is the "depth" in the film measured from the substrate side of the film; $d(x)$ is the collection distance as a function of depth x. Two approaches were used to prepare the samples for the depth profile studies. One approach used thick diamond samples (500 μm) cut from the same wafer which were thinned by removing different amount of materials to different thickness (Figure 51). The other approach, the different thicknesses were achieved by varying the growth time, keeping all other growth conditions constant.

Although the CPIC measurements deliver the averaged bulk information, the col-

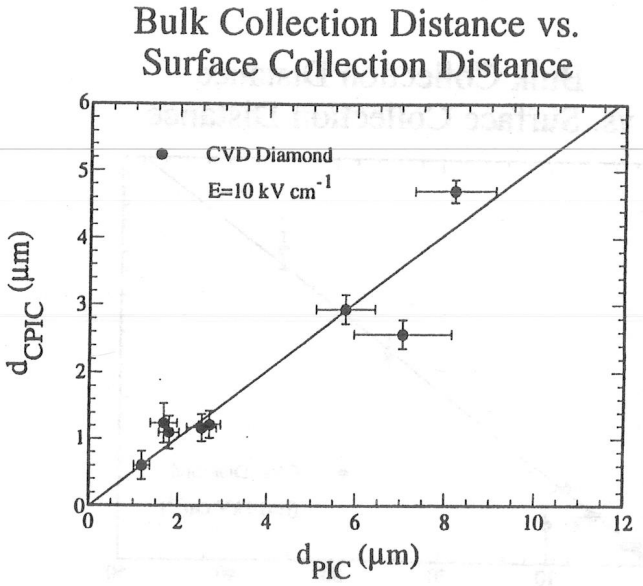

Figure 49: The relation between the results from the PIC measurements and the CPIC measurements. A weighted fit of the data gives $d_{CPIC} = (0.51 \pm 0.07)\ d_{PIC}$. This indicates that the bulk value is approximately equal to the average value of the collection distances at the two surfaces.

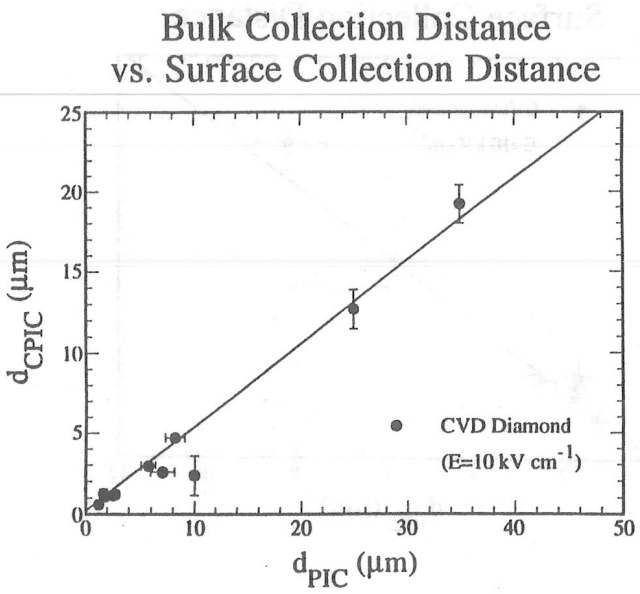

Figure 50: Bulk collection distance verse surface collection distance.

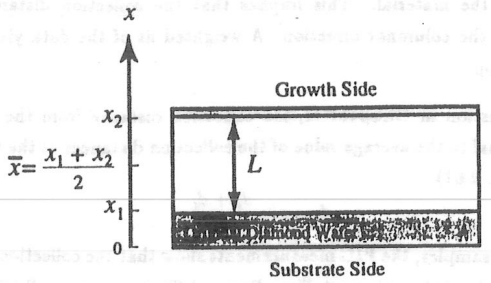

Figure 51: Sample preparations for the depth profile studies: the original wafer is shown. A sample is thinned down to a thickness of L. The shaded areas are the areas where materials are removed. The positions of the two surfaces of the sample are x_1 and x_2.

lection distance at the surfaces still can be derived based on the experimental results and theoretical analysis. Figure 52 illustrates the average collection distance, d_{CPIC}, as a function of $\overline{x} = (x_1 + x_2)/2$, where $\overline{x}$ is the "position" of each sample relative to the substrate of the original diamond wafer, and x_1 and x_2 represent the position of the two surfaces of each sample relative to the substrate (Figure 51).

As an averaged value of the collection distance in the bulk over a thickness of $L = x_2 - x_1$, d_{CPIC} can be expressed as:

$$d_{CPIC} = \frac{\int_{x_1}^{x_2} d(x')\,dx'}{x_2 - x_1} \tag{3.35}$$

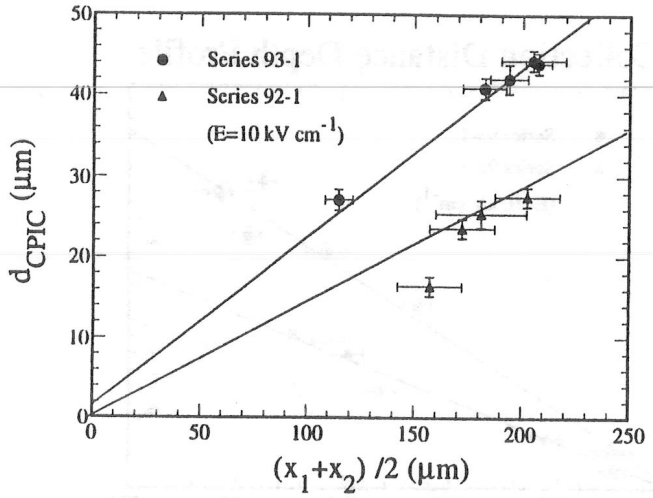

Figure 52: Plot shows the experimental results of d_{CPIC} as a linear function of $\bar{x} = (x_1 + x_2)/2$.

Figure 52 illustrates the linear relationship between d_{CPIC} and $(x_1 + x_2)/2$. As a result,

$$d_{\mathrm{CPIC}} = \frac{\int_{x_1}^{x_2} d(x')\,dx'}{x_2 - x_1} = a\,\frac{x_1 + x_2}{2} + b \tag{3.36}$$

where

$$a = \frac{2\,(d_{\mathrm{CPIC}} - d_s)}{x_1 + x_2}, \qquad b = d_s \tag{3.37}$$

Rewriting Eq. 3.36:

$$\int_{x_1}^{x_2} d(x')\,dx' = \frac{a}{2}\,(x_2^2 - x_1^2) + b\,(x_2 - x_1) \tag{3.38}$$

The solution of this equation may give the collection distance in a form of

$$d(x) = ax + b = \frac{2\,(d_{\mathrm{CPIC}} - d_s)}{x_1 + x_2}\,x + d_s \tag{3.39}$$

For the collection distance at the surfaces, we have:

$$d(x_1) = ax_1 + b = 2\,(d_{\mathrm{CPIC}} - d_s)\left(\frac{x_1}{x_1 + x_2}\right) + d_s \tag{3.40}$$

$$d(x_2) = ax_2 + b = 2\,(d_{\mathrm{CPIC}} - d_s)\left(\frac{x_2}{x_1 + x_2}\right) + d_s \tag{3.41}$$

This result suggests that if d_{CPIC} is a linear function of $\bar{x}$, which can be demonstrated by the CPIC measurements, the derived surface value $d(x)$ may be a linear function of x.

The depth profile of the surface collection distance is plotted in Figure 53 and Figure 54 for several series of diamond samples. The open marks are the derived values from the CPIC measurements. The solid marks are from the PIC measurements, the collection distance at the surface of the film. The horizontal error bar is estimated from the uncertainty as the result of removal of material applied on both side of the film. The solid line is the fit for the PIC results. A linear change in the collection distance with depth is shown for each series of samples. The linear behavior exhibited in Figure 53 and Figure 54 shows no saturation up to thickness of 500 μm.

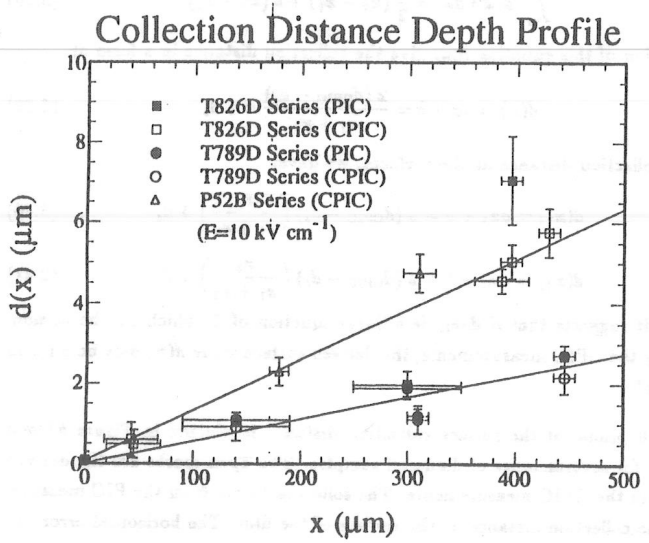

Figure 53: Collection distance depth profile. The solid marks are the surface values obtained directly from the PIC measurements. The open marks are the surface values derived from the bulk values d_{CPIC} based on the experimental results and analysis.

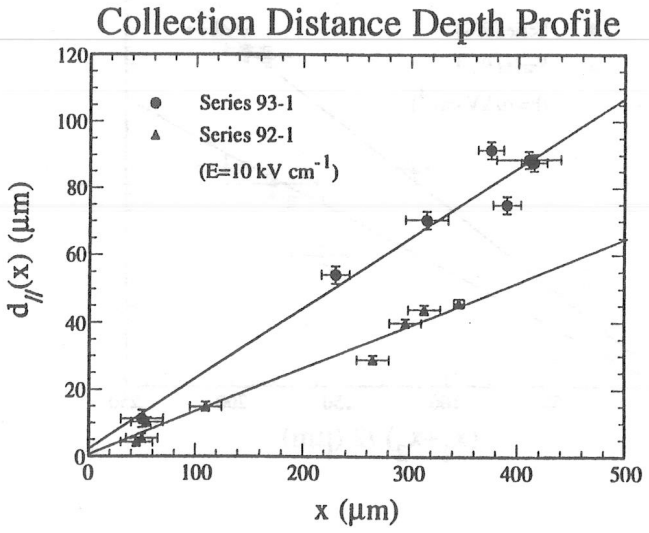

Figure 54: Plots show the depth profile for the derived surface collection distance from the CPIC measurements for high quality polycrystalline diamond films.

CHAPTER IV

MATERIAL CHARACTERIZATIONS

The electrical properties discussed earlier may be limited by imperfections in the material. By imperfections, we mean chemical impurities or structural defects. Such imperfections may form charged centers and crystal boundaries which reduce the carrier mobility. Imperfections may also form recombination centers which reduce the excess carrier lifetime. Material characterizations may help us understand the factors which limit the electrical properties in diamond.

A series of material characterization experiments have been performed on diamond samples. The material characterization experiments include visual observations, scanning electron microscopy, x-ray diffraction, Raman spectroscopy and photoluminescence. Visual observation may provide quantatitive information on impurities such as graphite or amorphous carbons in CVD diamond. An electron microscope image is a map of a crystal structure in real space. This method provides a powerful and direct approach to observe the material structure and defects at the surface. An x-ray diffraction pattern of a crystal is a map of the crystal in reciprocal space. X-ray diffraction measurements may deliver the information on crystal imperfections. Raman scattering yields information on phonon scatterings, impurities and defects. In this chapter, the material characterization experiments are introduced and the measurements are presented.

4.1 VISUAL OBSERVATIONS

Visual observation of polycrystalline diamond films leads to information on film color and transparency. Thus, the bulk polycrystalline film quality can be examined. The transparency was quantified by using the template grey scale shown in Figure 55. The template was printed on a piece of translucent tracing paper. When a diamond film was in contact with the template placed with a lighted background, the transparency, T, was determined by matching the greyness of the film with one of the markers on the template. By using a decreasing number of dots per unit area for each marker, the template was designed with a linear scale. When the film is opaque, the transparency T is equal to zero; when film is transparent, the transparency $T \sim 100$. The results for the measurements of T are listed in Table 9. The uncertainty of T measurement is of the order of $\Delta T \approx \pm 2$. In Figure 56, the transparency is plotted for three groups of samples with different thicknesses: ($350\ \mu\text{m} < L < 400\ \mu\text{m}$), ($400\ \mu\text{m} < L < 450\ \mu\text{m}$) and ($450\ \mu\text{m} < L < 500\ \mu\text{m}$). The uniform distributions of the transparency T in Figure 56 indicates that at a given thickness, the transparency of a diamond may vary. Thus, thickness alone does not determine the transparency.

When polycrystalline diamond films contain a large amount of non-diamond components such as graphite or amorphous carbon, they may look opaque and dark (Figure 57). In Figure 58, the sample containing less non-diamond components looks lighter. When samples have high quality, they look white, and after polishing they are translucent (Figure 59).

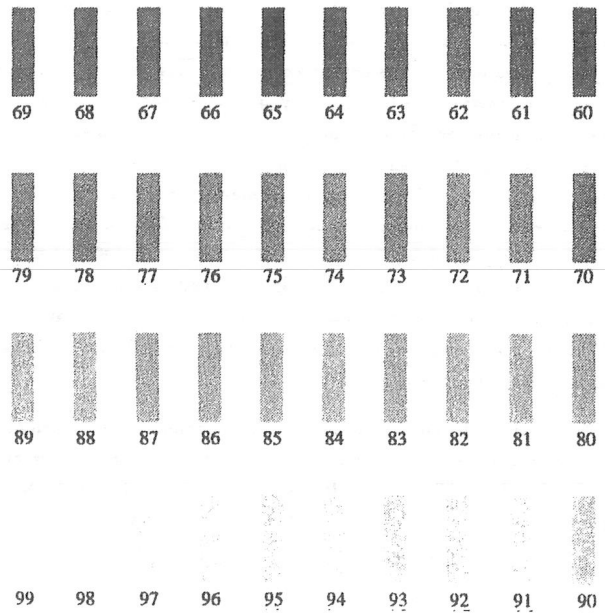

Figure 55: Transparency scale which is determined by the number of dots per unit area. The scale is linear. When the film is opaque, the transparency $T = 0$; when film is transparent, the transparency $T \sim 100$.

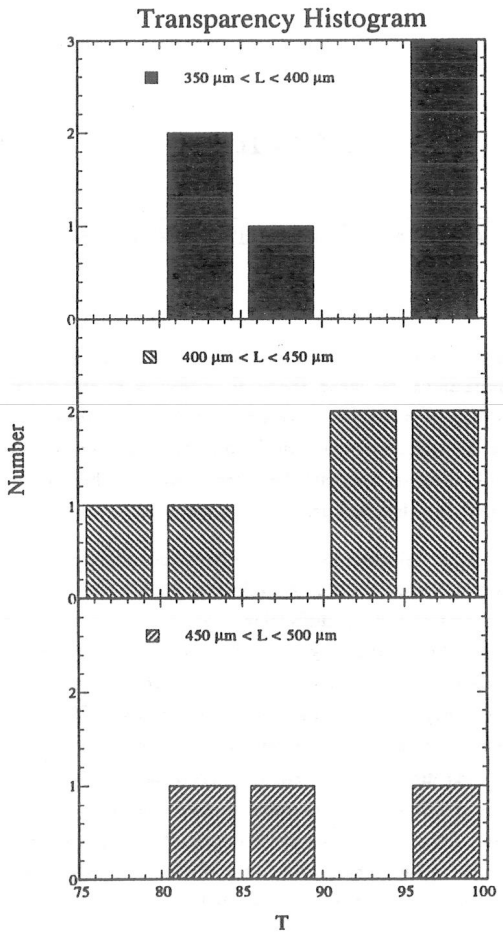

Figure 56: Transparency histograms for film with different thicknesses. The uniform distribution of each histogram indicates that at a given thickness, factors other than thickness determine the transparency.

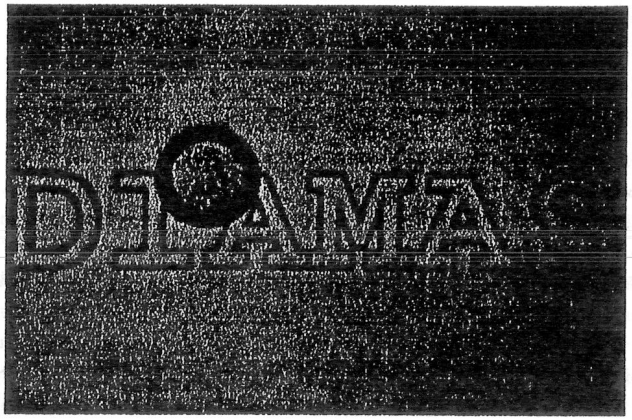

Figure 57: An optical image for a "dark" diamond ($T = 85$). This sample contains a large amount of non-diamond components. The light area at the center of the film is the metallic electric contact.

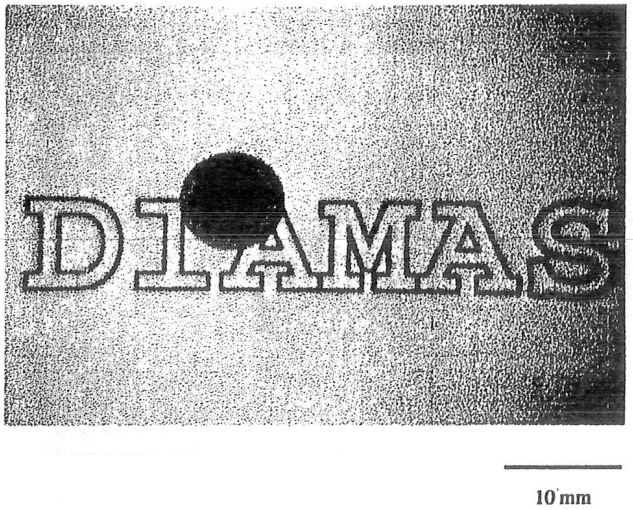

Figure 58: An optical image for a "light" diamond ($T = 95$).

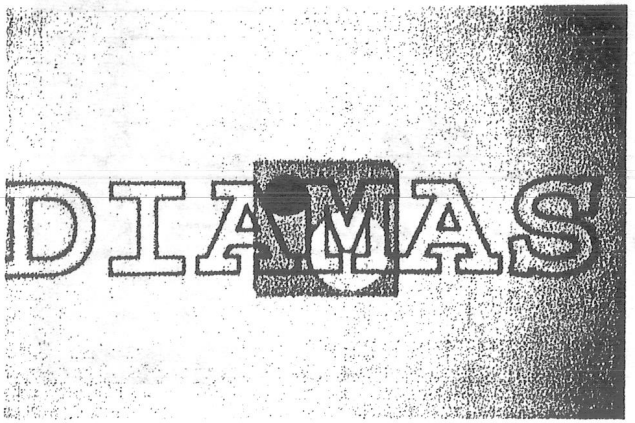

Figure 59: An optical image for a translucent diamond film ($T = 99$). There is a hole cut out of the diamond.

4.2 Scanning Electron Microscopy

Scanning electron microscopy (SEM) has been used to collect information on the crystal structure at surface of polycrystalline films. Grain uniformity was examined and the average grain size was determined at each surface. A cross-sectional observation was performed to examine the crystal growth formation.

4.2.1 Formation of Topographic Contrast

In a scanning electron microscope, an electron beam with a diameter of ~ 10 nm is produced under acceleration of $10 \sim 20$ kV in a vacuum chamber at 10^{-5} torr. A scanning generator controls a set of electromagnetic coils to scan the primary electron beam across the sample to collect information in a given area. When a sample is irradiated by a finely focused electron beam (Figure 60), secondary electrons [1], backscattered electrons, characteristic x-rays and several other types of radiation (Auger electrons, continuous x-ray spectrum etc.) are emitted from the irradiated zone due to the electron-sample interactions. The intensity of these signals depends upon the shape and the chemical composition of the irradiated volume. Since the energy of secondary electrons is small, the emission region of secondary electrons is just a few nanometers beneath the sample surface. Thus, the secondary electron image can be used to deliver surface information of a material.

Figure 61 illustrates the formation of the topographic contrast: ϕ is the angle between the primary beam and the normal to the sample surface, the yield of secondary electrons is given by [42]:

$$\text{yield} \propto \frac{1}{\cos \phi} \tag{4.1}$$

Since $\phi_A < \phi_B$, the yield of the secondary electron from surface "A" is less than that from surface "B". As a result, a detector will collect more secondary electrons

[1] Secondary electrons are the electrons excited by the primary electron beam bombardment having energy larger than the work function. The energy of secondary electrons is about a few electron volts.

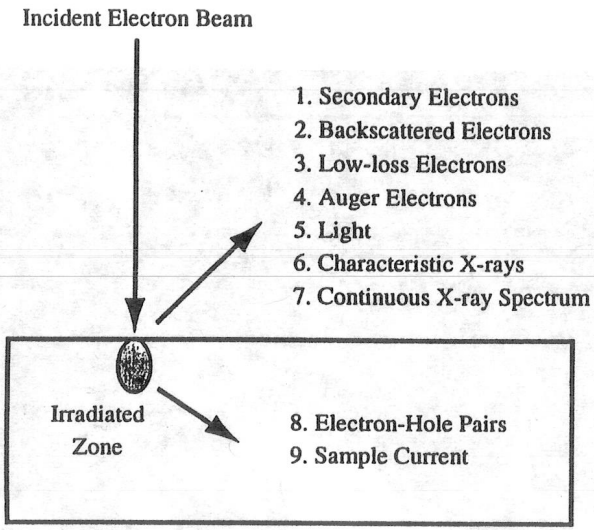

Figure 60: Schematic view of the electron-material interaction. A suitable detector is chosen to detect the desired signal. In a scanning electron microscope, the secondary electron image is used.

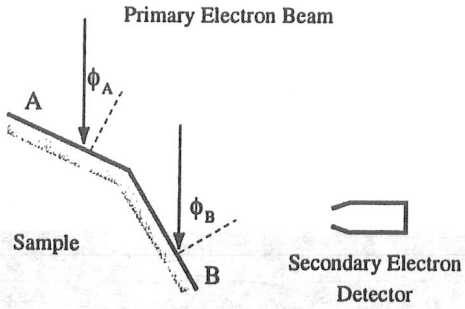

Figure 61: $\phi_A < \phi_B$, the yield of the secondary electron from surface "A" is less than that from surface "B". Thus a topographic contrast is formed.

from surface "B" than from surface "A". Hence, surface contours are illustrated by topographic contrast. This contrast modulates the brightness of the display on a cathode-ray tube (CRT) or on a POLAROID camera. The brighter parts of the image correspond to those parts of the sample with stronger signal.

The typical secondary electron images for the substrate side and growth side of polycrystalline diamond film are shown in Figure 62 and Figure 63. On the substrate side, the average grain size is $1 \sim 2$ μm and gaps can be observed between grains. On the growth side, large grains and clear faceting are visible.

The film cross section for a fractured portion is shown in Figure 64 where the cone shaped columnar crystal structure along the growth direction can be observed.

4.2.2 EXPERIMENTAL TECHNIQUES

The operating voltage of the electron microscope [2] was kept at 15 kV and the magnifications were typically $200 \sim 2000$. A photomultiplier sensitive to secondary

[2] INTERNATIONAL SCIENTIFIC INSTRUMENT ISI-SX-30.

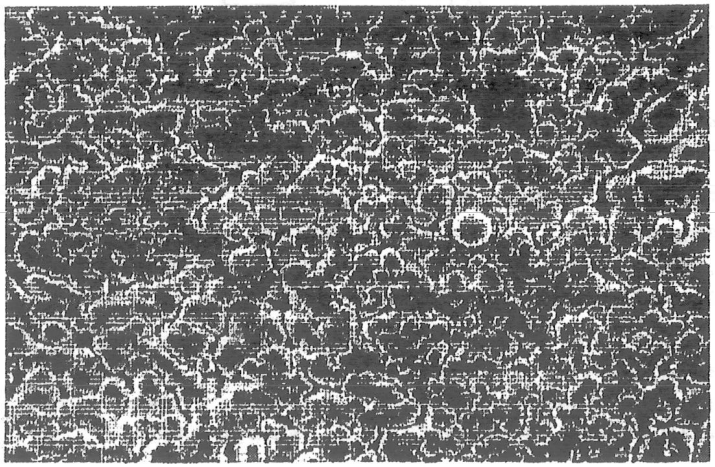

Figure 62: SEM photo of the substrate side of a polycrystalline diamond. The average grain size is $1 \sim 2\ \mu m$.

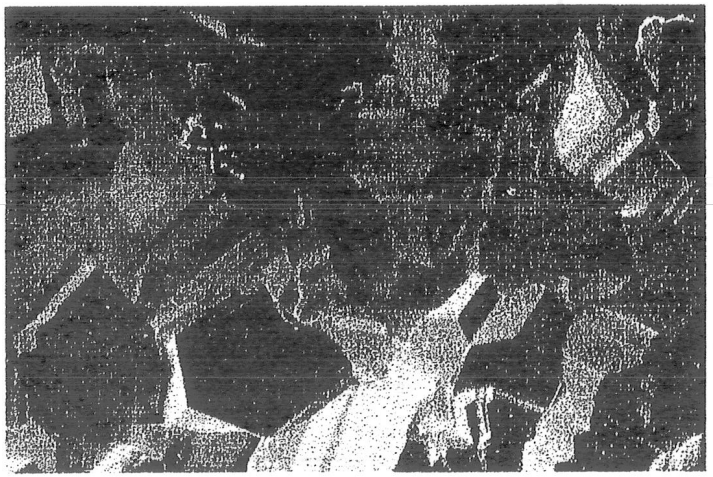

Figure 63: SEM photo of the growth side of a polycrystalline diamond.

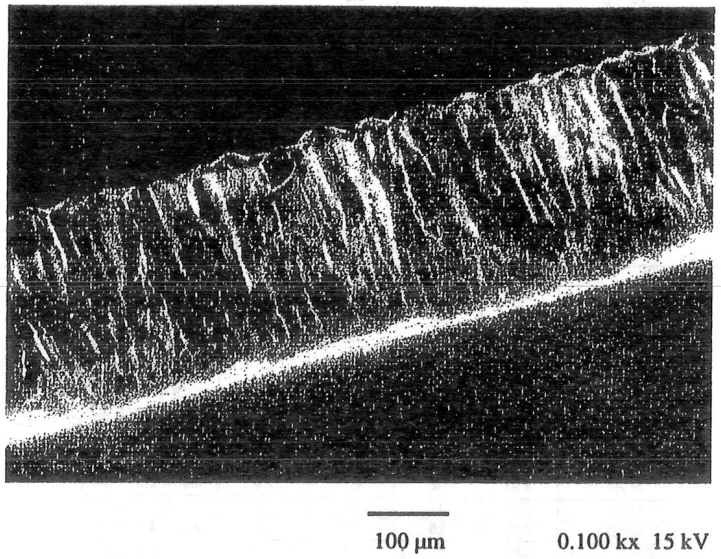

Figure 64: SEM photo of the cross section of a polycrystalline diamond film. The lower edge is the substrate side of the polycrystalline diamond film. The upper edge is the growth side. The columnar grain structure along the normal direction of the film can be seen.

electrons ($\sim$ 5 eV) was used.

For a highly insulating material, charge accumulation on the sample surface may occur when the sample is under exposure from the electron beam. The charge accumulated on the sample surface deflects the primary electron beam and interacts with the secondary electron causing an image distortion. This is called the *charging effect*. The charging effect was observed in our SEM experiments. To avoid this effect, a metallic layer was coated on the surface of each diamond.

4.2.3 Average Grain Size Measurement

As shown in Figure 64, polycrystalline diamond film has a cone shaped columnar grain structure. We use $g^{\parallel}$ to represent the grain size in the film normal direction, parallel to the columnar direction, and $g^{\perp}$ to represent the lateral average grain size on the film surfaces, perpendicular to the columnar direction. The average grain size, $g^{\perp}$, is measured following the standard method by American Society of Material Testing (ASMT): (1) choose an area, A, from an SEM photograph, usually a POLAROID film, (2) deduct the area of the spacing between adjacent grains (grain gap), A′, (3) count the number of grains N in the area (A − A′), (4) calculate the average area which each grain occupies, (5) calculate the average grain size using:

$$g^{\perp} = \sqrt{\frac{A - A'}{N}} \tag{4.2}$$

4.2.4 Experimental Observations and Results

As shown in Figure 62 and Figure 63, there is a difference of grain appearance and grain size between the substrate and the growth side of polycrystalline diamond films for all samples.

On the substrate side of the films, the grains are small, typically 1 $\sim$ 3 μm. Some samples exhibit a loose lateral structure. The gap between adjacent grains

can be as large as 8 μm while some samples show small gaps under 0.5 μm. The appearance of the substrate side of the film looks similar for different growth processes, microwave assisted plasma CVD process or DC Arc Jet CVD process, and different substrates, tungsten, molybdenum or silicon.

On the growth side of the films, the grains are larger than the substrate side. Some individual grains were measured to be as large as 100 μm. The average grain size, $g^{\perp}$, differs from sample to sample, ranging from 20 μm $\sim$ 70 μm. The grain appearance for different samples was also found to be different. Some samples exhibit smooth grain surface and clear crystal faceting; others show obvious structural defects.

The grain size along the columnar direction (Figure 64), $g^{\parallel}$, is larger than one hundred microns for a sample > 300 μm thick. Table 9 shows a summary for the SEM measurements for our samples.

Table 9: Results of SEM measurements and transparency measurements.

Sample	L (μm)	$g_g^{\perp}$ (μm)	$g_s^{\perp}$ (μm)	$l^{\dagger}$ (μm)	Gap (μm)	T
4K391B	60	23	0.5	$\sim$ 1	$\sim$ 0	-
4K440	250	28	‡	‡	‡	-
17Z05	330	46	‡	‡	‡	98
P52B-A	310	12	‡	‡	‡	71
P52B-B	180	10	1.0	1.0 $\sim$ 1.5	0.2 $\sim$ 1.0	72
T784D	408	54	2.5	2.0 $\sim$ 3.0	0.2 $\sim$ 5.5	75
T789D-1	445	28	3.8	3.0 $\sim$ 8.0	0.2 $\sim$ 8.0	90
T789D-2	310	21	2.0	2.0 $\sim$ 6.0	0.2 $\sim$ 3.0	95
T789D-3	165	20	5.7	-	-	-
T793D	275	46	2.2	1.0 $\sim$ 3.5	0.2 $\sim$ 2.0	95
T797D	470	47	1.5	1.5	0.2 $\sim$ 1.2	85
T797D-1	480	40	1.4	2.0	0.2 $\sim$ 0.5	84
T801D	370	51	2.4	1.5 $\sim$ 5.5	0.2 $\sim$ 3.5	82
T804D	390	45	1.8	2.0	0.2 $\sim$ 1.5	80
T816D-1	195	16	3.5	1.5 $\sim$ 5.0	0.2 $\sim$ 6.0	75
T821D	430	26	2.3	2.5	0.8	92
T826D-1	395	32	1.2	1.0	0.2 $\sim$ 0.8	89
T826D-U	430	36	1.6	1.0 $\sim$ 3.0	0.2 $\sim$ 2.0	89
T826D-P	340	35	4.0	4.0	$\sim$ 0	85
T826D-PA1	345	27	3.5	3.0	0.6	89
T834D-1	265	26	2.1	0.8 $\sim$ 2.5	0.2 $\sim$ 2.5	90
T846D-1	600	54	4.1	2.5 $\sim$ 5.5	0.2 $\sim$ 5.5	84
T886D	965	72	1.5	2.0	0.2 $\sim$ 2.0	91
T942D-U	330	23	2.5	2.0	0.2 $\sim$ 2.0	98
T942D-P	275	22	‡	‡	‡	99
T942D-C	345	26	2.2	3.0	0.2 $\sim$ 2.0	96
T949D	320	28	1.7	1.5 $\sim$ 3.5	0.2 $\sim$ 2.5	97
T950D	430	34	1.5	2.0	0.2 $\sim$ 1.0	97
T1013A	495	46	1.7	2.0	1.0	-
T1038D-U	430	48	1.2	1.0	0.2	97
T1093D	550	54	1.2	1.5	0.2 $\sim$ 1.0	97
T1097D	400	52	3.5	1.5 $\sim$ 5.0	0.2 $\sim$ 2.0	95
T1119D	625	56	3.0	1.0 $\sim$ 2.0	0.2 $\sim$ 3.0	97
T1154D	380	36	1.0	1.0	0.5	97
T1202D	390	42	1.4	1.0 $\sim$ 2.0	0.5 $\sim$ 2.0	95

† l: Grain-grain distance on the substrate side.
‡ smooth surface, crystal structure can not be resolved.

An increase of grain size $g^{\perp}$ with film thickness has been observed in all samples. The samples for the collection distance depth profile studies in Chapter III were measured using SEM to investigate the grain size depth profile for different growth conditions. Figure 65 shows the SEM results of grain size depth profile for several series of samples. The increasing behavior can be described by a linear function for a given series of samples. This linear increasing trend does not seem to saturate for sample thicknesses up to about 600 μm. The increase of grain size with the film thickness is consistent with the cone shaped columnar structure from the cross-sectional observations. This indicates that some crystal orientations have higher growth rate than the others in both the columnar and the lateral directions.

4.3 X-ray Diffraction

4.3.1 Diffraction Condition

Because of the periodic structure of a lattice, a diffraction pattern is formed when a monochromic x-ray beam is incident on a crystal. According to Bragg's law, the diffraction angle θ is determined by:

$$2\, d_{hkl}\, \sin\theta = n\, \lambda \tag{4.3}$$

$$d_{hkl} = \frac{a}{\sqrt{h^2 + k^2 + l^2}}$$

where 2θ is the angle between incident beam and diffracted beam (Figure 66); λ is the x-ray wavelength; n is the diffraction order; a is the lattice constant; h, k and l are the lattice plane indices.

4.3.2 Diffraction Selection Rule

The diffraction intensity, I, is given by [44]:

$$I \propto S_G^2 M^2 \tag{4.4}$$

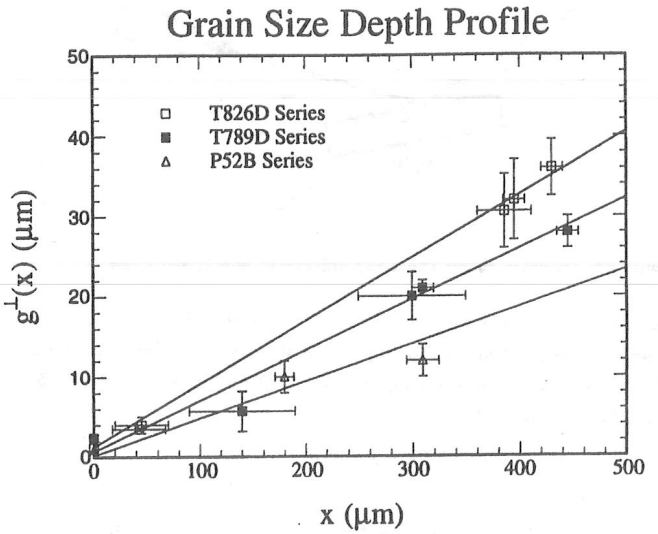

Figure 65: The average grain size depth profile $g^{\perp}(x)$. The substrate position of the diamond film is taken as $x = 0$.

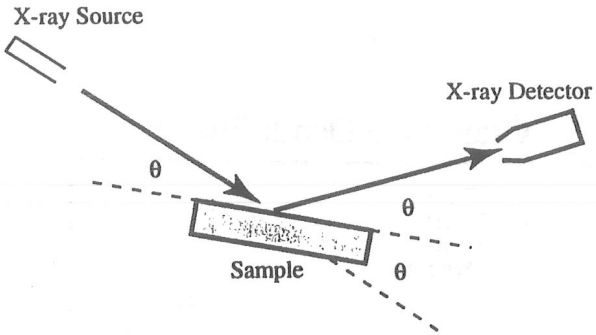

Figure 66: Diagram shows the x-ray diffraction and Bragg's law.

where M is the total number of unit cells in the crystal and S_G is called the *structural factor*. The structural factor represents the x-ray amplitude scattered by one unit cell and determines the x-ray diffraction (XRD) selection rules [1, 5]. The structural factor is given by:

$$S_G = \sum_j f_j \, e^{-i\vec{G}\cdot\vec{r}_j} \tag{4.5}$$

where the summation is over all the atoms of the basis; $\vec{r}_j$ is the position of j^{th} atom; $\vec{G}$ is the reciprocal lattice vector; and f_j is the *atomic form factor* for each atom j, which is defined as:

$$f_j = \int n_j(\vec{r}) \, e^{-i\vec{G}\cdot\vec{r}} \, d^3\vec{r} \tag{4.6}$$

where the integral extends over the atomic electron concentration n_j. Identical atoms have the same atomic form factor: $f_j = f$.

A diamond crystal consists of a face center cubic (*fcc*) lattice and a basis with two atoms on $(000, \frac{a}{4}\frac{a}{4}\frac{a}{4})$. The basis of an *fcc* lattice has identical atoms at $(000, 0\frac{a}{2}\frac{a}{2}, \frac{a}{2}0\frac{a}{2}, \frac{a}{2}\frac{a}{2}0)$. Because the primitive translation vectors of the lattice reciprocal to an *fcc* lattice are [1]:

$$\begin{aligned} \vec{b}_1 &= \frac{2\pi}{a}(-\vec{x}+\vec{y}+\vec{z}) \\ \vec{b}_2 &= \frac{2\pi}{a}(+\vec{x}-\vec{y}+\vec{z}) \\ \vec{b}_3 &= \frac{2\pi}{a}(+\vec{x}+\vec{y}-\vec{z}) \end{aligned} \tag{4.7}$$

the reciprocal lattice vector, $\vec{G}$, is given by:

$$\vec{G} = h\vec{b}_1 + k\vec{b}_2 + l\vec{b}_3 \tag{4.8}$$

The structural factor for an *fcc* lattice, S_G^{fcc}, is equal to:

$$S_G^{fcc} = f\left[1 + e^{-i\pi(k+l)} + e^{-i\pi(h+l)} + e^{-i\pi(h+k)}\right] \tag{4.9}$$

This means that in an *fcc* lattice, $S_G^{fcc} = 0$ when the indices are partly even and partly odd. In these situations, no diffraction occurs.

In the diamond basis, two atoms are located at $\vec{r}_1 = (000)$ and $\vec{r}_2 = (\frac{a}{4}\frac{a}{4}\frac{a}{4})$, the product of $\vec{G}\cdot\vec{r}_1$ is equal to unity and the product of $\vec{G}\cdot\vec{r}_2$ is equal to:

$$\begin{aligned} \vec{G}\cdot\vec{r}_2 &= (h\vec{b}_1 + k\vec{b}_2 + l\vec{b}_3)\cdot\frac{a}{4}(\vec{x}+\vec{y}+\vec{z}) \\ &= \frac{\pi}{2}(h+k+l) \end{aligned} \tag{4.10}$$

Then the structural factor for the diamond basis, S_G^{db}, can be calculated as:

$$\begin{aligned} S_G^{db} &= \sum_j f_j \, e^{-i\vec{G}\cdot\vec{r}_j} \\ &= f\left[1 + e^{i\frac{\pi}{2}(h+k+l)}\right] \end{aligned} \tag{4.11}$$

Hence, when the following conditions are satisfied, the structural factor for the diamond basis is given by:

$$\begin{aligned} S_G^{db} &= 0 && \text{if } h+k+l = 2(2m+1),\ m = 0,1,... \\ S_G^{db} &= 2f && \text{if } h+k+l = 4m,\ m = 0,1,... \\ S_G^{db} &= (1 \pm i)\, f && \text{if } h+k+l = \text{odd} \end{aligned} \tag{4.12}$$

The requirement of a non-vanishing structural factor, $S_G = S_G^{fcc} \cdot S_G^{db}$, yields diffraction selection rules. As a consequence, the allowed diffraction patterns for diamond lattice satisfy one of the following:

$$\begin{aligned} &(1)\ h+k+l = 4\text{m (all indices are even, m is an integer)} \\ &\qquad\qquad \text{or} \qquad\qquad (4.13) \\ &(2)\ \text{all indices } (h,k,l) \text{ are odd} \end{aligned}$$

When the Bragg condition Eq. 4.3 and the selection rules Eq. 4.13 are satisfied, a diffraction peak occurs and can be recorded by a detector. The allowed diffraction and the relative intensities for diamond powder [3] are listed in Table 10. The (220) diffraction is the second order diffraction for the crystal plane (110). The (220) diffraction peak is used to represent the (110) crystal plane since (110) diffraction is forbidden. The same situation is true for the (400) diffraction: since both the (100) and the (200) diffraction are forbidden, the fourth order diffraction for the crystal plane (100) is used to represent the (100) crystal plane.

From the x-ray diffraction pattern, information about the periodicity of the lattice, such as the lattice constant a, can be determined. In addition, the diffraction peaks may shift from the ideal position and the peaks may be broadened due to the existence of impurities and defects in polycrystalline diamond films. Thus, the effect of the crystal imperfections can be observed from the x-ray diffraction measurements.

4.3.3 X-ray Attenuation in Diamond

Normal Attenuation

When x-rays propagate in a material, energy is absorbed and the intensity is attenuated due to photo-electric absorption and incoherent scattering. The attenuation

[3] In powder form, each crystal orientation is randomly distributed.

Table 10: The allowed x-ray diffraction for diamond powder. The the wavelength of the incident x-ray is 1.5406 Å. Results were published by the Joint Committee for Powder Diffraction [43].

Diffraction	2θ (degrees)	Relative Intensity
(111)	43.917	100
(220)	75.304	25
(311)	91.542	16
(400)	119.659	8

of the x-ray intensity is given by [44, 45]:

$$\begin{aligned} I(x) &= I_0 \exp(-\gamma_L x) \\ &= I_0 \exp(-\gamma_m \rho_m x) \end{aligned} \qquad (4.14)$$

where I_0 is the incident x-ray intensity; if x is used to represent the distance from the material surface, $I(x)$ is the x-ray intensity at x; ρ_m is the mass density of the material; γ_m ($cm^2\ g^{-1}$) is called the *mass absorption coefficient* and the product of γ_m and ρ_m is called the *linear absorption coefficient*: γ_L (cm^{-1}) $= \gamma_m \rho_m$.

The mass absorption coefficient of carbon as a function of photon energy is shown in Figure 67. For an x-ray with a wavelength of 1.54 Å, the mass absorption coefficient is equal to $\gamma_m = 4.18\ cm^2\ g^{-1}$, and the linear absorption coefficient is equal to $\gamma_L = \gamma_m \rho_m = 14.7\ cm^{-1}$. This gives an absorption length ($1/\gamma_L$) of 680 μm in diamond. When an x-ray with a wavelength of 1.54 Å propagates through a 300 μm diamond film, the intensity attenuation is equal to:

$$\frac{I}{I_0} \approx 0.64 \qquad (4.15)$$

Abnormal Attenuation: Extinction

For a crystal with a periodic lattice structure, diffraction creates additional attenuation of the x-rays incident when the crystal is set at the Bragg angle. In

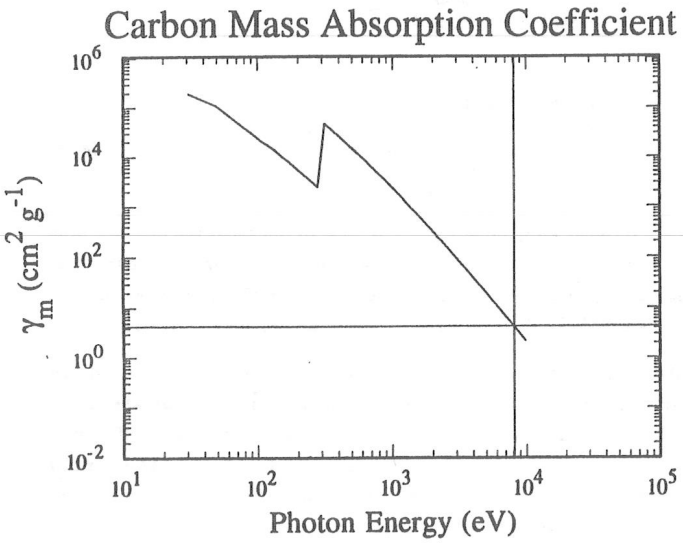

Figure 67: Mass absorption coefficient in carbon (B. L. Henke *et al.*, Atomic Data and Nucl. Data Table, 27, 27, 1982). For an x-ray with a wavelength of 1.54 Å (8047.8 eV of photon energy), the mass absorption coefficient is equal to $\gamma_m = 4.18$ cm^{2}g^{-1}.

addition to ordinary mass absorption, this coherent scattering process reflects the x-rays and the intensity of the transmitted x-ray is significantly reduced [4]. This phenomenon is called *extinction* [47].

The total attenuation can be empirically expressed by a linear attenuation factor γ'_L. The attenuation equation Eq. 4.14 can be rewritten as [44]:

$$I(x) = I_0 \exp(-\gamma'_L x) \tag{4.16}$$

where the linear absorption coefficient, γ'_L, is equal to:

$$\gamma'_L = \gamma_m \rho_m + gQ \tag{4.17}$$

In Eq. 4.17, g is the extinction constant and Q is called the *reflection scattering power* for an absorptionless crystal. The reflection scattering power is a function of the structural factor (S_G), the volume of the unit cell (V), the x-ray wavelength (λ) and the diffraction angle (θ) [5]:

$$Q = \left(\frac{e^2}{m_e c^2}\right)^2 S_G^2 \frac{\lambda^3}{V^2} \Theta(\theta)$$

$$\Theta(\theta) = \frac{1 + \cos^2 2\theta}{2 \sin^2 2\theta} \tag{4.18}$$

When the atomic planes form an arbitrary angle with the incident beam, no diffraction occurs. Under these circumstances, the second term in Eq. 4.17 is equal to zero. The attenuation is only a result of mass absorption. When diffraction occurs, the second term in Eq. 4.17 contributes to the attenuation of the x-ray intensity. If the size of a crystallite domain, r, is about 1 μm, a maximum value of the extinction constant can be given by: $g \approx r/\lambda \approx 6500$ [48]. Using the atomic form

[4] It is interesting that this was observed by Bragg in a diamond crystal. It was found that the observed intensities were considerably smaller than expected. This led Bragg to suspect that the diffracted beams were absorbed by the diamond crystal. A few years later, a complete explanation of this "abnormal" absorption effect was presented by Darwin [46].

[5] $V = \frac{1}{4}a^3$ for an *fcc* lattice.

Table 11: Linear attenuation length in diamond when diffraction occurs.

Diffraction Peak	$\Theta(\theta)$	Q (cm^{-1})	$1/\gamma_L'$ (μm)
(111)	1.50	0.385	4.0
(220)	0.572	0.147	10.8
(311)	0.501	0.129	11.6
(400)	0.171	0.0439	33.3

factor given by Eq. 4.6 for the carbon atom ($Z = 6$) at $r = 0$:

$$\begin{aligned} f &= \int n(\vec{r})\, e^{-i\vec{G}\cdot\vec{r}}\, d^3\vec{r} \\ &= \int n(\vec{r})\, d^3\vec{r} \\ &= 6 \end{aligned} \tag{4.19}$$

Then, the quantity Q, the linear attenuation coefficient (γ_L') and attenuation length ($1/\gamma_L'$) can be calculated. In Table 11, we list the results of this calculation. These results indicate that the x-ray diffraction measurements deliver the information near the diamond surface [6].

4.3.4 Experimental Techniques

A four-circle diffractometer [7] was used at room temperature. The x-ray radiation is produced by a secondary beam. When an accelerated electron beam strikes a copper target, the electrons occupying the inner atom orbitals of copper are excited leaving vacant orbitals. X-rays emit when the electrons with higher energy transit to fill in the vacancies. Figure 68 illustrates the L-K and M-K transitions and the corresponding frequencies of the x-ray emissions. For the α emissions, a doublet of wavelengths is obtained: $\lambda_{K\alpha_1} = 1.5406$ Å and $\lambda_{K\alpha_2} = 1.5443$ Å.

[6] If the crystallite domain is larger than 1 μm, from Eq. 4.17, the attention length, $1/\gamma_L'$, will be smaller than the values in Table 11.

[7] Scintag PAD-V with a diffraction management software package (DMS-2000™).

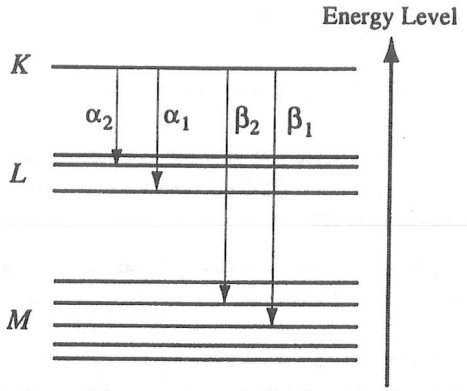

Figure 68: X-ray production through L-K and M-K shell transitions: $\lambda_{K\alpha_1} = 1.5406$ Å and $\lambda_{K\alpha_2} = 1.5443$ Å. $\lambda_{K\beta_1} = 1.39214$ Å and $\lambda_{K\beta_2} = 1.39220$ Å.

The acceleration voltage and current were kept at 45 kV and 20 mA respectively. A nickel filter was used to eliminate the K_β emissions. A set of small receiving slits (0.3 mm/0.1 mm) at the entrance of the detector was used to reduce the instrumental broadening of the diffraction peaks. The position of the x-ray source was fixed. The sample rotates about the x-ray source controlled by a step motor with a constant angular velocity of ω while the detector rotates with an angular velocity of 2ω.

In order to satisfy the Bragg condition Eq. 4.3 (Figure 66), the normal direction of the sample surface should be kept in the plane formed by the incident beam and diffracted beam. In addition, the angle between the sample surface and the incident beam should be the same as the angle between the sample surface and the diffracted beam (the Bragg angle θ). Thus, the angle between the incident beam and the diffracted beam is equal to 2θ. To achieve these geometrical requirements, an angular position calibration for the sample holder and detector was performed before measurements started. A slow motor speed was chosen to maintain the

accuracy in the intensity of the diffraction patterns.

4.3.5 Diffraction Peak Intensity

A scan of a diamond sample started with $2\theta = 25°$ and ended above 120°. Because of the polycrystalline nature of the CVD diamond films, a multi-peak diffraction pattern was observed (Figure 69).

Unlike the random distribution of the crystal orientations for a material in the powder form, polycrystalline material has a preferred crystal orientation, called *texturing*. Because the diffraction intensity is proportional to the square of the total number of unit cells in the crystal [49], the relative intensity of the diffraction peaks from differently oriented crystals represents the relative quantities of those crystals. Thus, the relative diffraction intensity can be used to demonstrate a preferred orientation in polycrystalline materials.

Texturing was observed in all the polycrystalline diamond samples. The ratio of the relative intensity was found to be different from sample to sample. Even for the same sample, the texturing at the growth side differs from that at the substrate side. In Figure 69, the difference of texturing at the growth side and the substrate side of a polycrystalline diamond is shown. For comparison, a schematic diffraction pattern for diamond powder is also shown in Figure 69. It can be seen that the crystals exhibit more (110) texturing at the growth side of the film than the substrate side. The (110) texturing is larger than the random orientation of diamond in powder form.

From our measurements, at the substrate side, samples with (110) texturing or (111) texturing were found. At the growth side, strong (110) texturing was observed in almost every sample. This indicates that the growth rate of the crystals with (110) orientation is higher than other orientations. That implies that coned shaped (110) oriented crystal grains are formed at the growth side of the films.

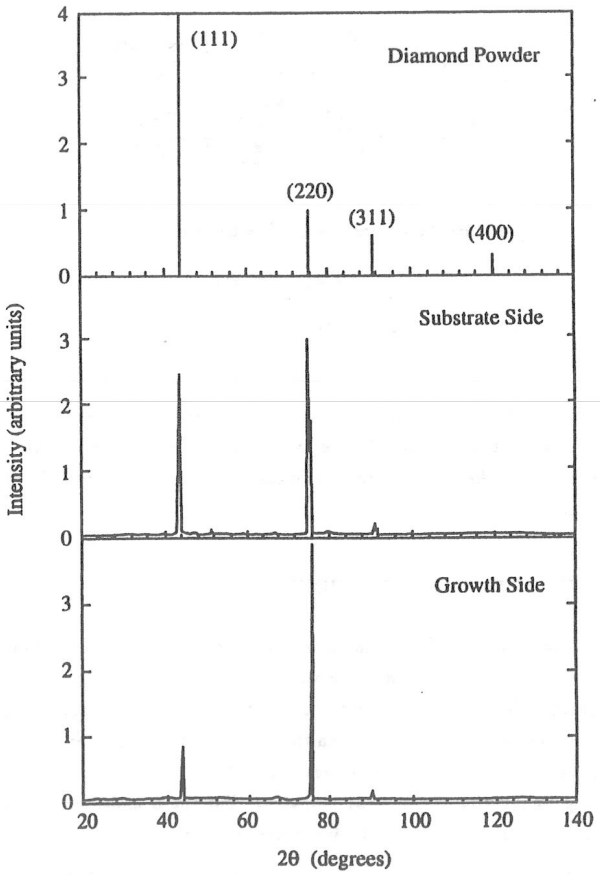

Figure 69: X-ray diffraction pattern for the substrate side and the growth side of a polycrystalline diamond film (T942D-U): (111), (220) and (311) diffraction peaks can be seen. The upper plot shows the relative diffraction intensity for diamond powder.

4.3.6 Diffraction Peak Position

The diffraction peak position (2θ) can be determined from the experimental results. Since the α x-ray radiation contains two peaks, a double Gaussian function was used to fit the experimental diffraction intensity $I(\theta)$:

$$I(2\theta) = I_0 + I_1 \exp\left[-\frac{(2\theta - 2\theta_{\alpha_1})^2}{2\sigma_{\alpha_1}^2}\right] + I_2 \exp\left[-\frac{(2\theta - 2\theta_{\alpha_2})^2}{2\sigma_{\alpha_2}^2}\right] \qquad (4.20)$$

Among the fitting factors, I_0 is the background intensity; $2\theta_{\alpha_1}$ and $2\theta_{\alpha_2}$ are the measured doublet peak positions; σ_{α_1} and σ_{α_2} are the peak widths. The error of the intensity $I(2\theta)$ is equal to $\sqrt{I(2\theta)}$ because of the Poission distribution for counts from the photo-multiplier x-ray detector. Substituting θ_{α_1} and θ_{α_2} in Eq. 4.3 and using $\lambda_{K\alpha_1}$ and $\lambda_{K\alpha_2}$, the lattice constant, a, can be calculated and averaged (Table 12).

A standard calibration sample (quartz pellet) provided by the instrument manufacturer, was used to calibrate the system. The deviation of the diffraction peak position (2θ) from the JCPD standard results [43] indicates an error less than 0.02° (Figure 70). This implies an error of 0.001 Å in the diamond lattice constant measurement at $2\theta \sim 75°$.

For a comparison with polycrystalline diamond films, a natural IIa diamond sample, (110) orientation, are also measured and analyzed (Figure 71). To offset the misalignment between the atomic plane and the film surface plane, the sample was tilted to fit the atomic plane into the system calibrated reference plane where Bragg condition can be satisfied. The experimental results are listed in Table 12.

From the lattice constant measurements, deviations from an ideal diamond lattice constant were found in polycrystalline diamond films. Deviation from a perfect crystal lattice due to crystal imperfections may cause the diffraction peak position shift [44, 49, 50]. For polycrystalline diamond, during the growth processes, the existence of vacancies in the crystal, impurities incorporated into the lattice, and structural defect may cause internal strain in diamond films. The strain can slightly enlarge or reduce the lattice constant which will also shift the diffraction peaks [44,

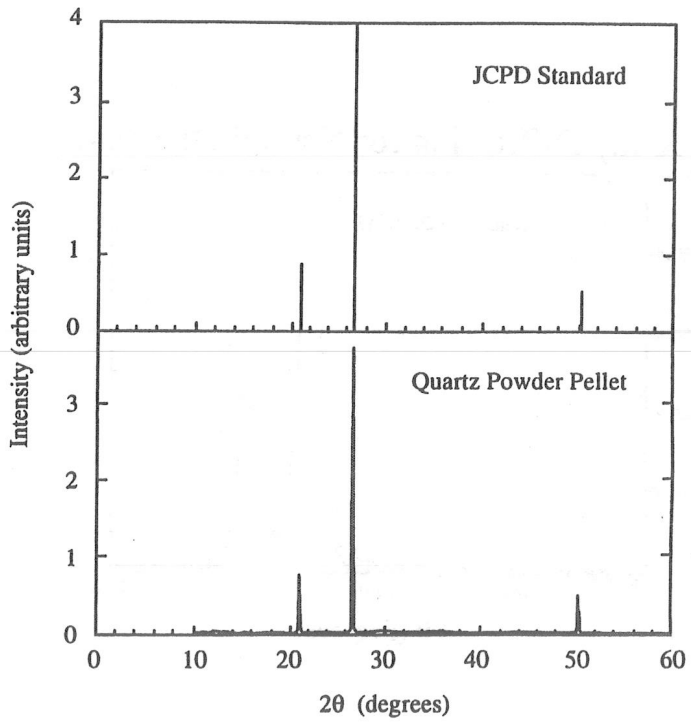

Figure 70: X-ray diffraction for a quartz powder pellet. The top plot is from the JCPD standard diffraction data file for quartz.

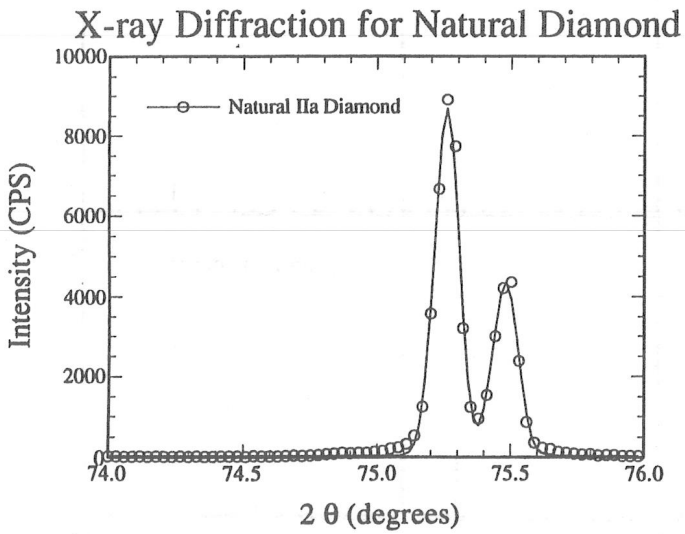

Figure 71: X-ray diffraction for a single crystal diamond sample. Crystal orientation is (110).

Table 12: Results of x-ray diffraction measurements.

Sample	a (Å)	β_d (degrees)
Natural (4×4)	3.5703 ± 0.0004	0.010 ± 0.008
T784D	3.5648 ± 0.0004	0.200 ± 0.008
T789D-1	3.5665 ± 0.0004	0.135 ± 0.008
T793D	3.5669 ± 0.0004	0.052 ± 0.008
T797D	3.5654 ± 0.0004	0.158 ± 0.008
T801D	3.5657 ± 0.0004	0.179 ± 0.008
T804D	3.5653 ± 0.0004	0.214 ± 0.008
T826D-1	3.5665 ± 0.0004	0.154 ± 0.008
T826D-U	3.5678 ± 0.0004	0.084 ± 0.008
T834D-U2	3.5676 ± 0.0004	0.068 ± 0.008
T846D-U2	3.5655 ± 0.0004	0.117 ± 0.008
T942D-U	3.5689 ± 0.0004	0.044 ± 0.008
T942D-C	3.5698 ± 0.0004	0.048 ± 0.008
T1038D-U	3.5701 ± 0.0004	0.048 ± 0.008
T1093D	3.5691 ± 0.0006	0.074 ± 0.008
T1097D	3.5694 ± 0.0006	0.079 ± 0.008

49].

For each run of XRD measurements, the result of the peak positions, $2\theta_{\alpha_1}$ and $2\theta_{\alpha_2}$, were found to have fluctuations caused by random factors such as misalignment and non-perfect position calibration. To estimate the random errors, the deviation of the each diffraction peak position from the mean value is plotted in a histogram in Figure 72. The standard deviation is equal to 0.026° which is consistent with that measured using the quartz pellet. This leads to an error in an individual lattice constant measurement of $\sigma_a = 0.001$ Å. The error of a mean value for N measurements is equal to $\sigma_a/\sqrt{N}$.

4.3.7 Diffraction Peak Width

The diffraction peak obtained from the experiments has a finite width. The measured peak width, β_{meas}, can be the result of the following reasons:

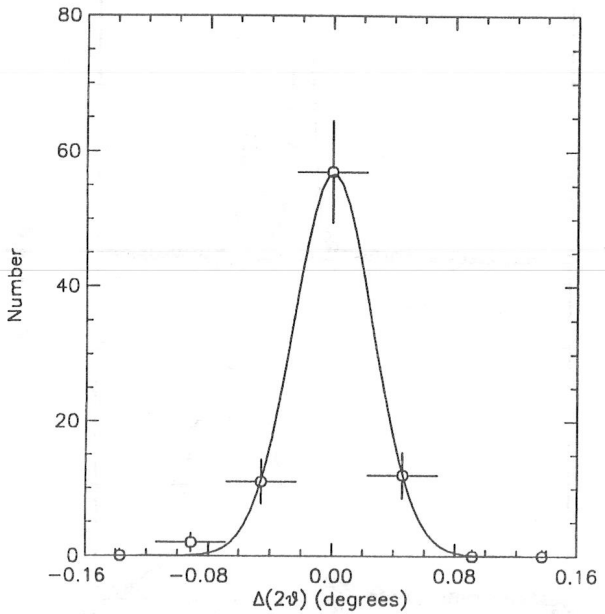

Figure 72: The deviation of the diffraction peak position from a mean value. A Gaussian fit gives an estimated error due to the random factors: $\sigma = 0.026°$.

1. Instrumental broadening. Because of a non-monochromaticity of the x-ray, finite size of the source, divergent incident beam, finite size of the receiving slits, and unresolved doublet diffraction peaks, the diffraction peak has a minimum width, β_{inst}.

   In order to analyze the diffraction width, sample with crystallite size causing no broadening and low defect density is usually used to estimate the instrumental broadening β_{inst} [44]. From the XRD measurements on a quartz pellet, the instrumental width was estimated to be $\beta_{inst} \sim 0.1°$.

2. Small grain size. Bragg's law is applicable to crystals consisting of an infinite stack of parallel atomic planes. In a polycrystalline material, the crystallite with limited grain size contains a much smaller number of atomic planes than a single crystal. This may cause a broadened diffraction peak. Scherrer (1928) first derived a formula to estimate the grain size from the diffraction width β_g. A number of investigators have confirmed this relation [44, 49, 50, 51]:

   $$\beta_g = \frac{\kappa\lambda}{D\cos\theta} \tag{4.21}$$

   where λ is the x-ray wavelength; D is the average grain size; $\kappa = 0.94$ for the grain dimension normal to the reflection planes and $\kappa = 1.8$ for the grain dimension parallel to the reflection planes.

   From the SEM measurements on the polycrystalline diamond films, the smallest average grain size was found to be about 1 μm. Using Eq. 4.21, the peak width β_g due to the grain dimensions was calculated. The result shows that β_g is much smaller than the instrumental width: $\beta_g \ll \beta_{inst}$. Thus, the peak broadening due to the grain size can not be observed in this experiment. In other words, the diffraction peak broadening is not the consequence of the polycrystalline grain size.

3. Structural defects. Deviation from a perfect crystal lattice due to crystal imperfections may cause a broadened diffraction peak [44, 49, 50]. Defects such as dislocations and small angle boundaries [8] may cause the crystal to deviate

[8] formed by parallel array of dislocations.

from a perfect periodic structure resulting in broadened diffraction peaks. Also, a non-uniform strain can contribute to the diffraction peak width [44]. The diffraction peak width caused by the crystal structural defects is called β_d. The actually observed curve is the convolution of the contribution of instrumental factor and the crystal defects. Stokes developed a method to resolve the convolution due to the two kinds of broadening [44]:

$$\beta_d = \sqrt{\beta_{meas}^2 - \beta_{inst}^2} \tag{4.22}$$

Thus, the diffraction peak width due to the crystal structural defects, β_d, can be evaluated.

The width of the diffraction peak can be used as a relative measure of crystal quality. When the diffraction peaks are sharp enough, the α doublet diffraction peaks can be resolved. However, when crystal quality is poorer, as shown in the lower plot in Figure 73, the broadened α_1 and α_2 peaks can not be easily resolved.

Using the same method to estimate the random errors in the peak position measurements, the deviation of the each diffraction peak width (σ) from the mean value is plotted in a histogram in Figure 74. We find the standard deviation to be 0.02°

4.3.8 Correlations with Visual Observation

Transparency T from the visual measurements was found to be correlated with the XRD measurements. In Figure 75, an increase of transparency with lattice constant is shown. In addition, the transparency increases when the x-ray diffraction peak width decreases (Figure 76).

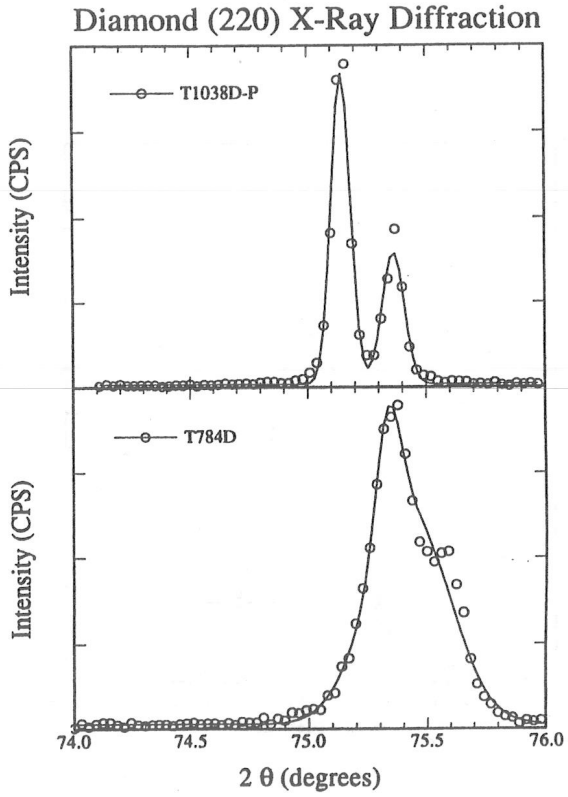

Figure 73: The difference in crystal quality as characterized by the peak width. Polycrystalline diamond (220) diffraction peak is plotted: the upper plot shows that the α doublet can be resolved for a film with good quality; the lower plot shows the poorer film quality where the α doublet can not be resolved. The solid lines are the double Gaussian fit. Also, the difference of the peak positions for the two samples can noticed.

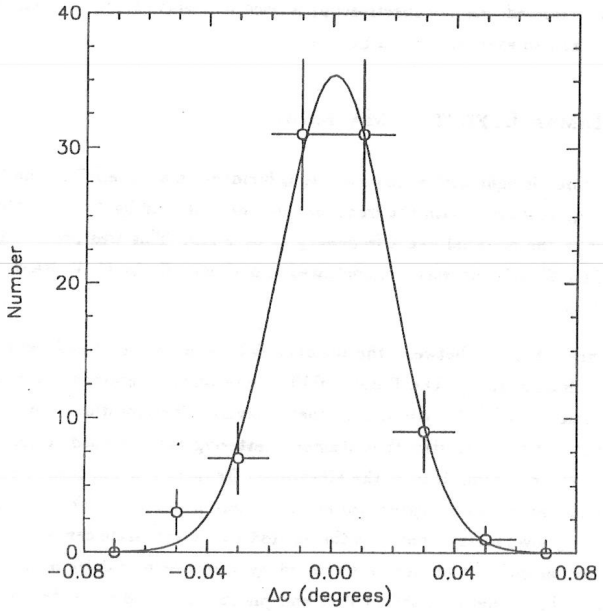

Figure 74: The deviation of the diffraction peak width (σ) from a mean value. A Gaussian fit gives an estimated error due to random factors ($\sigma = 0.02°$).

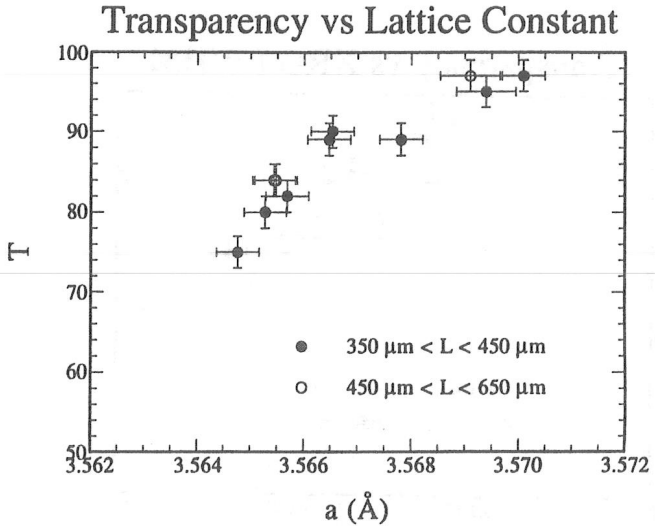

Figure 75: Transparency as a function of lattice constant. The transparency increases when lattice constant, a, approaches 3.57 Å.

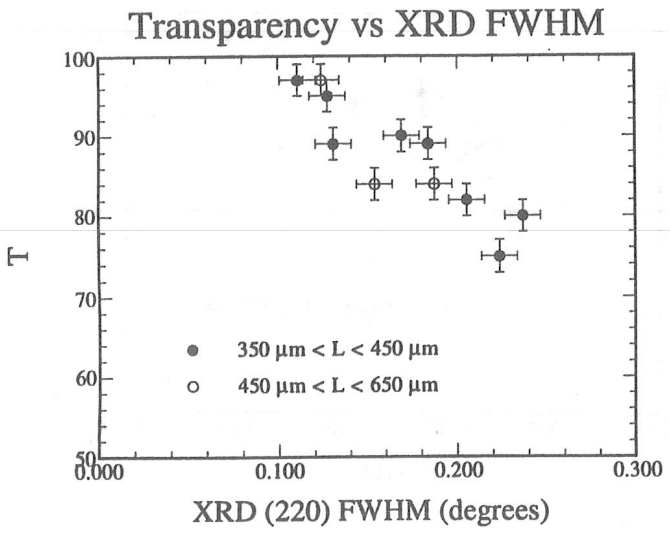

Figure 76: Transparency as a function of x-ray diffraction peak width. The narrower the x-ray diffraction peak, the higher the transparency.

4.4 Raman Spectroscopy

During the CVD growth process of diamond, it is crucial to form sp^3 σ-type bonds among the carbon atoms. However, if the growth conditions are not correct, some undesired type of bonds such as graphite with sp^2 π-type bonding, or amorphous carbon may be formed. Raman spectroscopy is used to observe these non-diamond compositions and to examine crystal quality.

4.4.1 Raman Effect in Material

When monochromic light with a frequency ν_0 is incident on a material, in addition to the Rayleigh scattering with the frequency ν_0, the scattered light by the atoms or molecules in the material has a frequency of $\nu_0 \pm \Delta\nu$. This was predicted by A. Smekal in 1923 [52] and was demonstrated experimentally by C. V. Raman in 1928 [53, 54, 55].

The frequency difference between the incident light and the scattered light $\Delta\nu$ is called the *Raman shift*. The Raman shift corresponds to phonon transitions between atomic or molecular vibrational energy levels. The vibrational levels are a characteristic of the material; thus Raman scattering may be used to identify impurities in the material. If ν_1 is the vibrational frequency of the ground state, the vibrational energy can be expressed as $h\nu_1$, where h is the Planck's constant. Then the energy level corresponding to the excited vibrational state can be written as $h\nu_2$. When an incident photon is scattered by atoms or molecules in a material, energy exchange between the photon and phonon occurs due to the phonon transition between vibrational levels. After scattering, the energy of the photon becomes:

$$h\nu' = h\nu_0 \mp h\Delta\nu \tag{4.23}$$

where $\Delta\nu = \nu_2 - \nu_1$ and "$\mp$" represents the direction of the energy transfer: "$-$" represents the energy is transferred from the photon to the atoms (molecules); "$+$" represents the energy is transferred from the atoms (molecules) to the photon

(Figure 77). $h\nu' = h\nu_0 - h\Delta\nu$ is called the *Stokes line*; $h\nu' = h\nu_0 + h\Delta\nu$ is called the *anti-Stokes line.*

The diamond Raman line is $\Delta\nu = 1333.5 \pm 0.5$ cm^{-1} at 149°K; $\Delta\nu = 1332.5 \pm 0.5$ cm^{-1} at 300°K. The temperature broadening of the Stokes line of diamond is measured 1.48 ± 0.02 cm^{-1} at 149°K and 1.65 ± 0.02 cm^{-1} at 300°K [56]. The temperature broadening yields a minimum width for the diamond Raman line.

Momentum conservation only allows the Raman phonon transition to occur near the center of Brillouin zone ($\vec{k} \sim 0$) because of the small wave vector of the photon compared with the size of Brillouin zone, This is called the $\vec{k}$-selection rule. Single crystal graphite shows a Raman line at $\Delta\nu = 1575$ cm^{-1}. However, microcrystalline graphite and disordered carbons can cause relaxation of the transition $\vec{k}$-selection rule for the optical branch phonons due to the loss in long range order. As a consequence, more phonons are allowed in the transition resulting broadened bands at 1355 cm^{-1} and 1590 cm^{-1} [56, 57, 58].

From the Raman spectra, the following information can be obtained.

1. The impurities in polycrystalline diamond film. The non-diamond carbon compositions, graphite or amorphous carbons, can be identified.
2. The overall crystal quality. The existence of chemical impurities and structural defects gives rise to distortion of the lattice from a perfect periodic structure. This may disturb lattice vibrations (phonon scatterings). The profile of the diamond Raman line at 1333 cm^{-1} and the line width, Γ, can be used as the relative measures of this distortion [57]. From the line width Γ, the crystal perfection may be used to rank the quality of the polycrystalline diamond films. Also, the comparison with the line width of a natural diamond can be made.
3. Lattice strain. This can be observed from a shift of the Raman line because the vibration modes are associated with the force constant or Young's modulus [59].
4. Grain size. When crystallites are small enough (a few hundred angstroms),

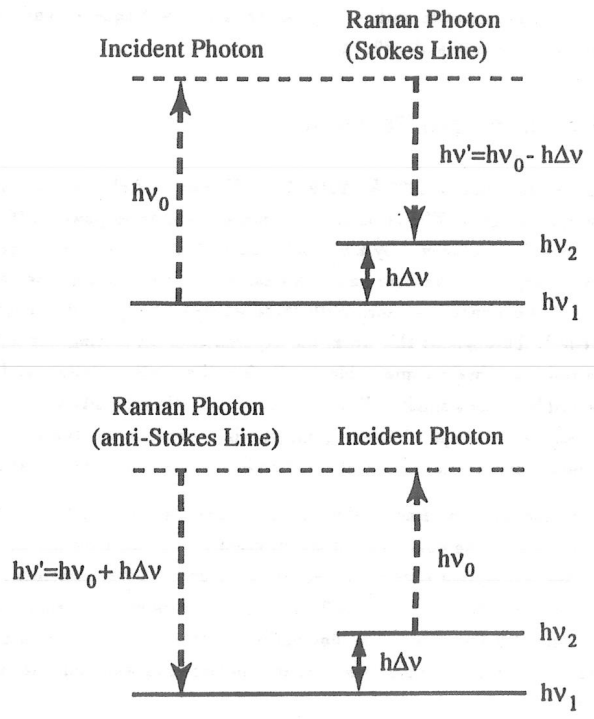

Figure 77: Transition diagrams for Raman scattering: above diagram shows the Stokes transition; bottom diagram shows the anti-Stokes transition.

the violation of periodic boundary condition for an ideal crystal results in a relaxation for the transition $\vec{k}$-selection rule. Then the Raman line shape tends to be asymmetric with a long tail towards low frequency end. Also, the line position will shift [60, 61].

4.4.2 Experimental Technique

The primary laser excitation 4880 Å (20491.7 cm^{-1}) from an Ar^+ laser was used to provide the incident light. The beam size is 1 mm and the beam power is 50 mW. The Raman signal was observed by a monochromator [9]. A sample was placed at a 45° angle with respect to the laser beam. An entrance slit of 200 μm was used in the entrance of the monochromator. With these settings, the spectrum resolution is about 2 cm^{-1}. Throughout this work, the experimental slit setting was fixed at 200 μ m in order to obtain comparable results for all samples. Better resolution may be reached by using a smaller slit (50 μm), however, the intensity will decrease accordingly and some samples become unmeasurable. Caution was taken to avoid using high power excitation to prevent the diamond phase from graphitization.

An extended scan with the Raman shift $\Delta\nu$ from 200 cm^{-1} to > 2000 cm^{-1} was performed to identify the non-diamond compositions. The scanning increment of 5 cm^{-1} and the integrating time of 0.4 seconds were used. A fine increment (0.02 cm^{-1}) was used from 1310 cm^{-1} to 1350 cm^{-1} for the diamond spectrum with an integrating time of 0.4 seconds. The fluctuations of the position of the diamond Raman line for the same sample measured in different runs was found to be less then 0.2 cm^{-1}.

Figure 78 shows the extended Raman spectra from two polycrystalline diamond films. No peak or band at 1355 cm^{-1} or 1590 cm^{-1} is observed. The large background in the lower plot in Figure 78 is due to photoluminescence.

[9] Double SPEC monochromator with an amplified photocurrent photon counter.

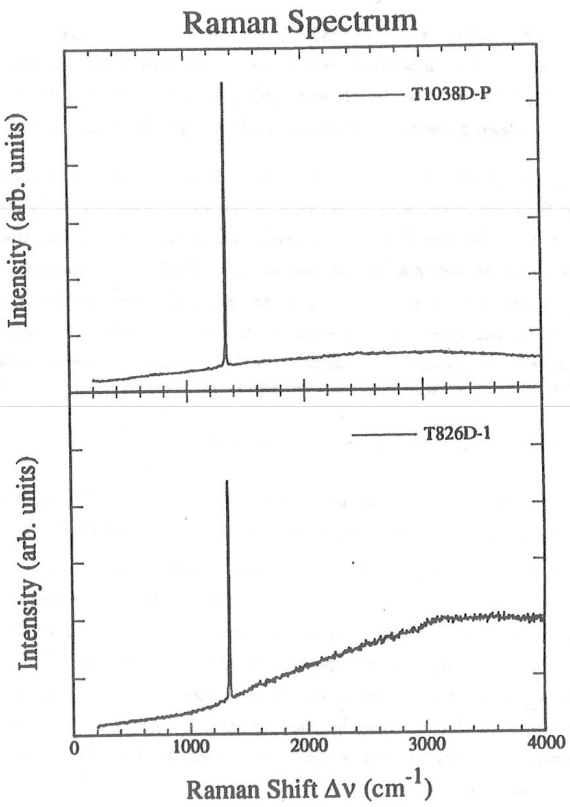

Figure 78: Raman spectrum for two polycrystalline diamond films. The diamond Raman line at 1333 cm^{-1} can be seen. The luminescence background can be also seen.

4.4.3 Experimental Results and Analysis

To obtain the position for diamond Raman line ($\Delta\nu$) and the line width (Γ), a Lorentzian function was used to fit the experimental Raman line shape [24]:

$$I(\nu) \propto \frac{1}{(\nu - \Delta\nu)^2 + \left(\frac{\Gamma}{2}\right)^2} \tag{4.24}$$

Thus, both $\Delta\nu$ and Γ can be determined. Figure 79 illustrates the fitting results for two polycrystalline diamond films. Raman spectroscopy of both natural IIa diamond and polycrystalline diamonds have been studied. For a natural IIa diamond (4 mm$\times$ 4 mm$\times$ 250 μm), the diamond spectrum exhibits the Raman shift $\Delta\nu = 1332.6$ cm^{-1} and line width, $\Gamma = 2.4$ cm^{-1}. The line width for polycrystalline diamond films range from 2.8 cm^{-1} $\sim$ 10 cm^{-1} indicating the different quality of the films. Table 13 summarizes some of the Raman measurements.

The Raman shift $\Delta\nu$ for all samples measured is plotted in a histogram in Figure 80. This figure shows that the deviation from a mean value is 0.4 cm^{-1} which is less than the experimental resolution. In other words, no shift of diamond Raman line was observed for any sample. Also, all the line shape can be fitted by a symmetric Lorentzian function. Thus, no grain size effect was observed.

4.4.4 Correlation with X-ray Diffraction Studies

A correlation between Raman line width (Γ) and x-ray diffraction peak width (FWHM) is found as shown in Figure 81. Both the Raman line width and the x-ray diffraction peak width indicate the film quality. The sharper peaks from either measurements exhibits higher film quality.

Raman line width is plotted against lattice constant of polycrystalline diamond in Figure 82. Samples with broader Raman line width exhibit smaller lattice constant.

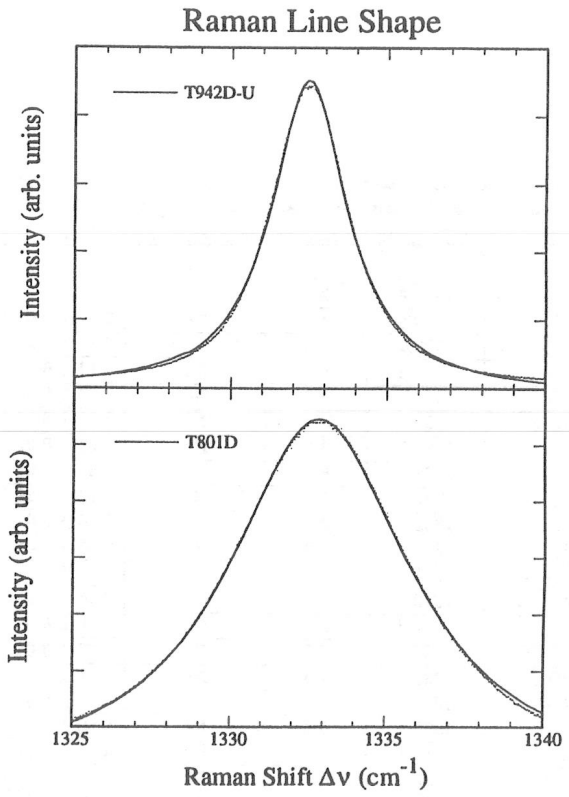

Figure 79: The diamond Raman line shape: dots are the experimental data and the solid lines are from a Lorentzian fit. Different line width due to the different film quality can be noticed.

Table 13: Results of Raman measurements. η is the ratio of the photoluminescence background near 3000 cm^{-1} to diamond Raman peak height at 1333 cm^{-1}.

Sample	$\Delta\nu$ (cm^{-1})	Γ (cm^{-1})	Non-diamond Band	η
Natural 4×4	1332.6	2.4	—	—
4K440	1333.0	4.9	No	0.34 ± 0.01
BS-508	1333.1	11.5	1560 cm^{-1}	0.82 ± 0.05
T789D-1	1331.2	4.9	No	0.19 ± 0.02
T789D-2	1331.8	3.3	No	0.18 ± 0.02
T789D-3	1331.8	10.2	No	0.41 ± 0.04
T801D	1332.8	7.0	No	0.28 ± 0.01
T826D-1	1332.5	8.4	No	0.49 ± 0.02
T826D-U	1332.3	2.8	No	0.12 ± 0.01
T826D-P	1332.4	2.9	No	0.09 ± 0.01
T826D-PA1	1331.6	2.9	No	0.09 ± 0.01
T834D-U1	1331.9	3.4	No	0.08 ± 0.01
T834D-U2	1332.5	3.4	No	0.08 ± 0.01
T939D-P	1332.8	2.9	No	0.09 ± 0.01
T942D-U	1332.5	2.8	No	0.12 ± 0.01
T942D-P	1332.5	2.8	No	0.11 ± 0.01
T949D	1333.1	3.5	No	0.21 ± 0.03
T950D	1333.1	3.3	No	0.22 ± 0.03
T1038D-P	1332.8	2.9	No	0.12 ± 0.01
T1093D	1333.0	4.0	No	0.40 ± 0.08
T1097D	1333.0	3.4	No	0.22 ± 0.04
T1119D	1333.1	3.4	No	0.12 ± 0.03

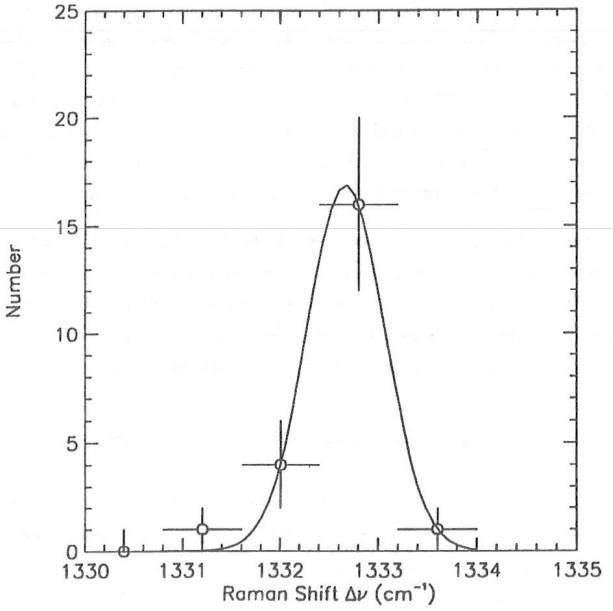

Figure 80: The change of diamond Raman shift for all samples used is less than the experimental resolution. No spectrum shift was observed.

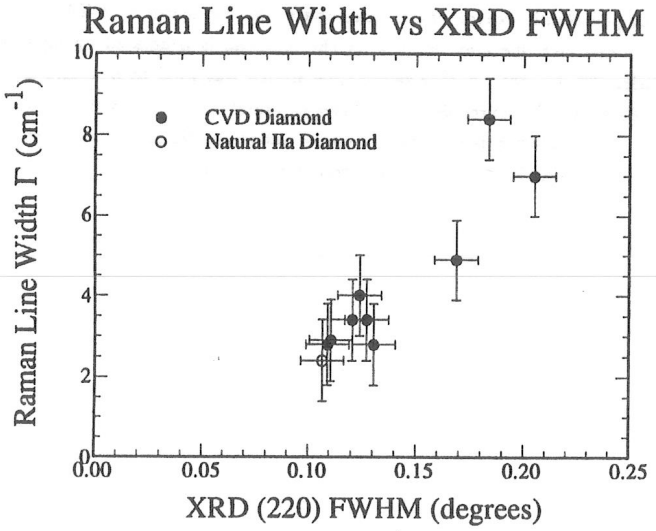

Figure 81: The correlation between Raman line width (Γ) and the (220) x-ray diffraction peak width (FWHM).

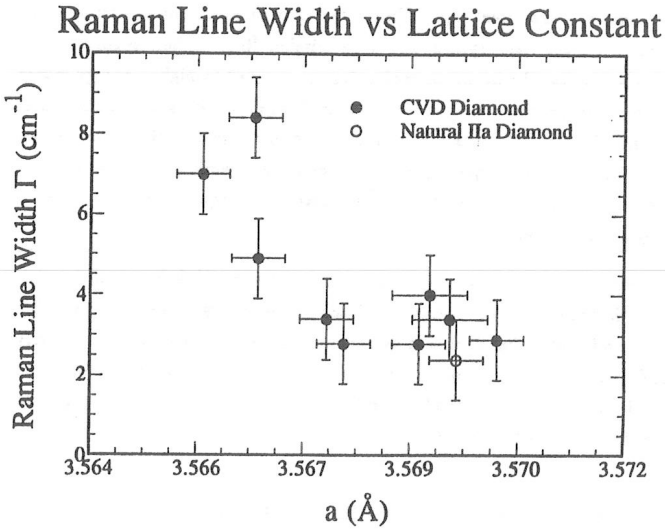

Figure 82: Raman line width as function of lattice constant.

4.5 PHOTOLUMINESCENCE

4.5.1 PHOTO-INDUCED LUMINESCENCE

Photo-induced luminescence or photoluminescence is produced by the absorption of infra-red, visible or ultra-violet light. Unlike the Raman effect, photoluminescence involves two processes: absorption and transmission [62]. When absorbing the energy of a photon $h\nu$, the atoms or molecules are excited to higher energy states from ground state; when the excited atoms or molecules are back to ground state, the energy may be released in the form of luminescence. In addition, the Raman shift is independent of the frequency of the incident light while photoluminescence can only be observed for the photons with particular frequencies which can be absorbed by atoms or molecules.

Photoluminescence can provide information about structural defects and impurities because the luminescence energy is related to the energy level difference between band-band, defect-band, defect-defect, or impurity-band impurity-impurity states [63, 64]. From the background photoluminescence due to lattice defects, the lattice disorder can be examined [57]. A high luminescence background is reported for low quality CVD diamonds [57].

4.5.2 EXPERIMENTAL TECHNIQUE AND RESULTS

A laser excitation of 4880 Å (20491.7 cm^{-1}) from an Ar^+ laser was used. Using the same setup for the Raman measurement, the difference between the wave number of the scattered light and the incident light, $\Delta\nu$, was recorded. The photoluminescence energy, $h\nu'$, can be obtained using the Raman shift (the Stokes line) deduced from the wave number of the incident photon ($\nu_0 = 20491.7$ cm^{-1}):

$$h\nu' = (hc) \times 20491.7 \text{ cm}^{-1} - \Delta\nu \qquad (4.25)$$

$\Delta\nu$ was measured from 200 cm^{-1} to 4000 cm^{-1}. Therefore, the energy levels from 2.0 eV to 2.5 eV were probed. A difference in luminescence background

can been noticed in Figure 78 near 3000 cm^{-1}. The ratio of the height of the photoluminescence background near 3000 cm^{-1} to the diamond Raman peak height at 1333 cm^{-1}, η, is calculated and shown in Table 13. Figure 83 illustrates a correlation between η and diamond Raman line width Γ. It can be noticed that the samples with larger η exhibit wider line width.

An important photoluminescence line in diamond is the H3 center at 2.464 eV. This photoluminescence line may occur after the diamond is irradiated by high energy particles [62, 65, 66]. A ^{90}Sr radioactive source was used to irradiate a sample over 50 hours. This provided a low level of radiation ($\leq$ 1 Krad). After the exposure, the photoluminescence H3 line was searched for. No H3 centers were found. Higher level radiation exposures are presently in progress.

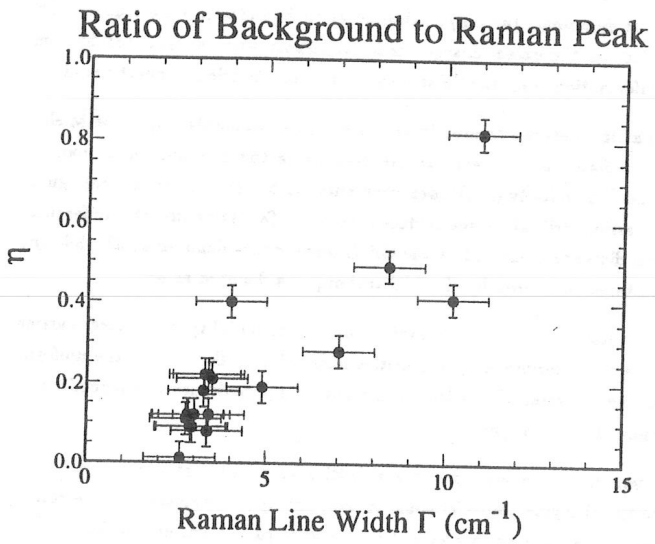

Figure 83: The ratio of the photoluminescence background to the diamond Raman peak height is plotted. The larger the ratio is, the wider line width the sample exhibits.

CHAPTER V

Summary and Conclusions

5.1 Correlation between the Electrical Properties and the Material Characterizations

To improve the electronic quality of polycrystalline diamond films and the performance of diamond radiation detectors, correlations between the electrical properties and the material characterizations have been studied.

5.1.1 Correlation with Visual Observations

For a given range of collection distance, the relationship between transparency and film thickness was observed. For the samples with large collection distance (25 μm $< d <$ 35 μm at an electric field of 10 kV cm^{-1}), transparency is high and slightly dependent with film thickness (Figure 84). For the samples with small collection distance ($d <$ 5 μm at an electric field of 10 kV cm^{-1}), transparency decreases with film thickness (Figure 84).

From Figure 85, the correlation between collection distance and transparency is shown. The polycrystalline diamond films with high transparency has excellent electrical properties ($d_{\mathrm{CPIC}} >$ 15 μm). However, this rule is not sufficient for high quality in electrical properties, not all polycrystalline diamonds with high

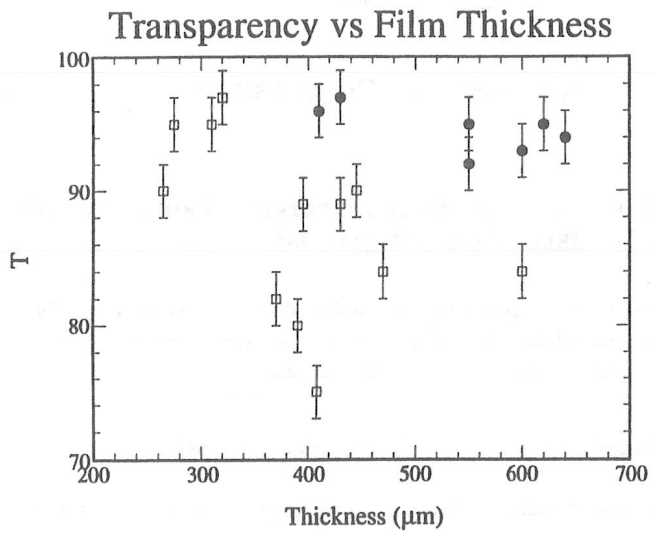

Figure 84: Transparency as function of film thickness. The solid marks are for the samples with large collection distance (25 μm $< d <$ 35 μm at an electric field of 10 kV cm^{-1}). The open marks for the samples with small collection distance ($d <$ 5 μm at an electric field of 10 kV cm^{-1})

transparency exhibit high quality of electrical properties.

5.1.2 Correlation with SEM Studies

From the SEM observations and measurements of the grain size in both lateral and transverse directions, the polycrystalline grain boundaries were studied. The boundary effect on the excess charge carrier transport were investigated by combining the information from the SEM results and the electrical property studies.

In charged particle-induced conductivity (CPIC) measurements, with a MIM electric contact configuration, excess carriers drift along the columnar direction. In photo-induced conductivity (PIC) measurements, with a planar contact configuration, excess carriers drift along the surface direction. To distinguish this difference, the collection distance measured by the CPIC technique is denoted as $d^{\parallel}$ while the collection distance measured by the PIC technique is denoted as $d^{\perp}$.

In a single crystal diamond, the limitation of carrier mobility and excess carrier lifetime is mainly determined by impurities and defects. Because of the uniform nature of a single crystal, the collection distance is approximately independent of drift direction: $d^{\parallel}(x) \approx d^{\perp}(x)$.

In a polycrystalline diamond, the crystal lattice terminates at grain boundaries causing additional crystal imperfections. A relationship between the bulk collection distance (d_{CPIC}) and the surface collection distance (d_{PIC}) was established in our experiments and analysis:

$$d_{\mathrm{CPIC}} = \frac{d_{\mathrm{PIC}}}{2} \qquad (d_s = 0) \tag{5.1}$$

This relationship was found to be independent of sample thickness. However, it was demonstrated from the lateral grain size depth profile studies that the polycrystalline grain size and grain boundaries are thickness dependent. This implies that grain boundaries have no influence on the excess carrier drift processes for the samples which show the relationship in Eq. 5.1.

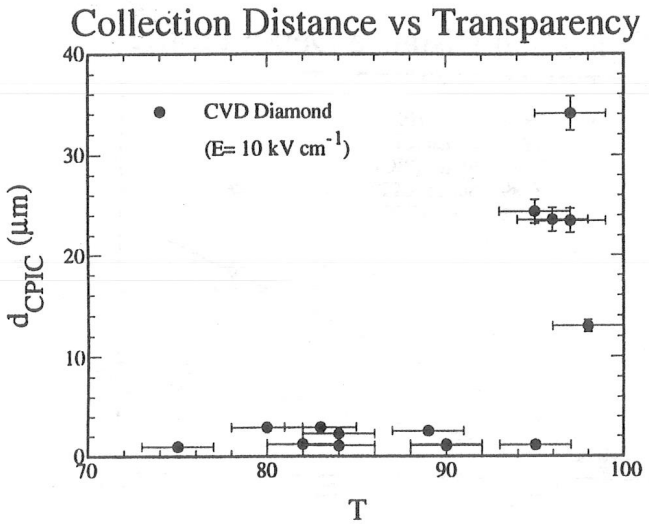

Figure 85: Correlation between collection distance and transparency.

As the quality of polycrystalline diamond films improves, the collection distance may be comparable to the lateral grain size: $d^{\perp} \sim g^{\perp}$. From Figure 86, $d_{CPIC} \approx \frac{1}{2} d_{PIC}$ implies that boundaries have no significant influence on carrier transport in both directions even though the collection distance is close to the lateral grain size ($20 \sim 30$ μm).

When the effect of the grain boundaries is not important, the collection distance is determined by the local densities of impurities and defects. Thus, for a given depth x into a polycrystalline diamond film, the collection distance is independent of drift direction: $d^{\parallel}(x) \approx d^{\perp}(x)$. This result allows us to compare the measured surface collection distance using the PIC technique with the derived surface collection distance from the CPIC measurement. In Figure 87, both measured surface collection distance and derived collection distance are plotted and the agreement is shown: $d_s^{\parallel} \approx d_s^{\perp}$ and $d_g^{\parallel} \approx d_g^{\perp}$. Finally, the increase in collection distance with film thickness implies that the defect density decreases as the film grows because the impurity level should not change significantly during the film growth process.

5.1.3 Correlation with X-ray Diffraction Studies

A correlation between collection distance and lattice constant is demonstrated in Figure 88. An increase of collection distance with lattice constant can be observed. The samples with large collection distance ($d_{CPIC} > 15$ μm) exhibit large lattice constant (~ 3.570 Å); the samples with small lattice constant (< 3.568 Å) show smaller collection distance ($d_{CPIC} < 5$ μm). In Figure 88, the results for a (110) single crystal type IIa diamond ($a_{IIa} = 3.5695$ Å, $d_{CPIC} \approx 26$ μm) are on the correlation curve for polycrystalline diamond.

Figure 89 shows a correlation between collection distance and diffraction width (FWHM). The resolution of the diffraction peak width measurement is limited by the instrumental width $\beta_{inst} \sim 0.1°$. The samples with an excellent electrical properties ($d_{CPIC} > 15$ μm) exhibit narrower diffraction peaks ($\sim 0.1°$). The samples whose diffraction peaks are broad ($> 0.15°$) show small collection distance

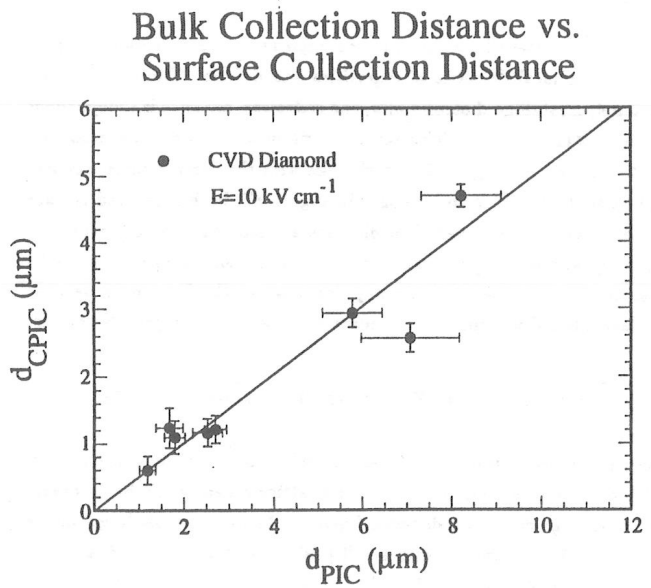

Figure 86: CPIC measurements vs PIC measurements.

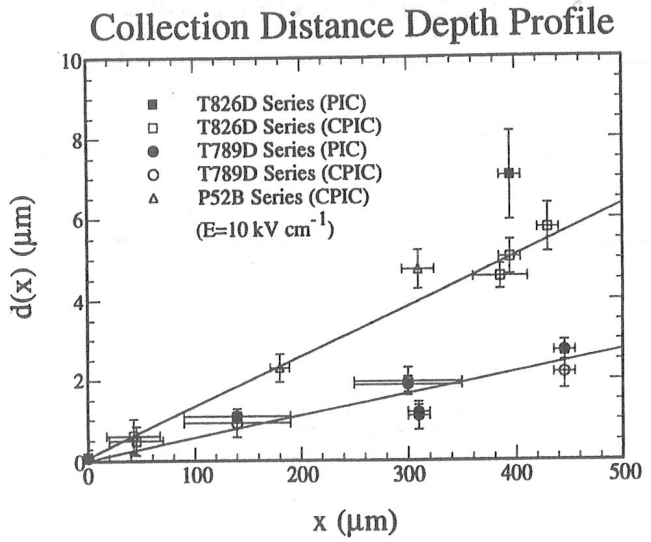

Figure 87: The solid marks are the surface values obtained directly from the PIC measurements. The open marks are the surface values derived from the bulk values d_{CPIC} based on the experimental results and analysis.

($d_{CPIC} < 5$ μm).

5.1.4 Correlation with Raman Studies

As a characteristic, the Raman line width indicates the overall film quality. The existence of point defects, single or aggregate impurities, isotope atoms and crystal boundaries may cause scattering of phonons. This process is called phonon relaxation process [68]. As a result, Raman lines are broadened. A correlation study between collection distance (d_{CPIC}) and Raman line width (Γ) was performed. In Figure 90, the samples with an excellent electrical properties ($d_{CPIC} > 15$ μm) demonstrate narrower Raman line width ($\Gamma \sim 2.5$ cm^{-1}); the samples with broader Raman line width ($\Gamma > 5$ cm^{-1}) exhibit poor electrical properties ($d_{CPIC} < 5$ μm). The Raman line width was found not to be sufficient for excellent electrical properties. The reason may be a result of a limited spectrum resolution for this technique and the setting used (200 μm slit). Further research is needed at low temperature, and/or with smaller entrance slit (20 $\sim$ 50 μm), or using Brillouin scattering to increase the inherent resolution.

5.1.5 Correlation with Film Growth Rate

It was found that the film grown with slower rate exhibits larger collection distance as shown in Figure 91. The impurity density can not be likely changed with film growth rate. However, the defect density and overall crystal quality may significantly depend on growth rate. The crystal defects which may limit collection distance includes the charged scattering centers and recombination centers formed by lattice imperfections. Figure 91 suggests that crystal defects in diamond have strong influence on the electrical properties. The scatter of the experimental results in Figure 91 for fixed growth rate are due to other growth parameters.

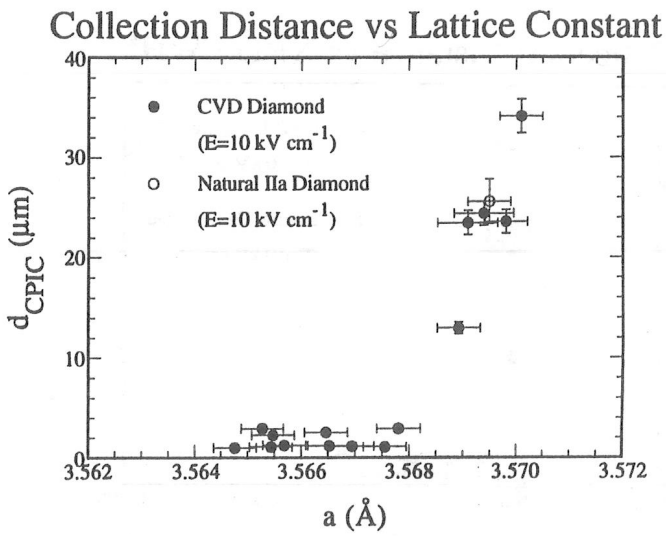

Figure 88: Correlation between collection distance and lattice constant.

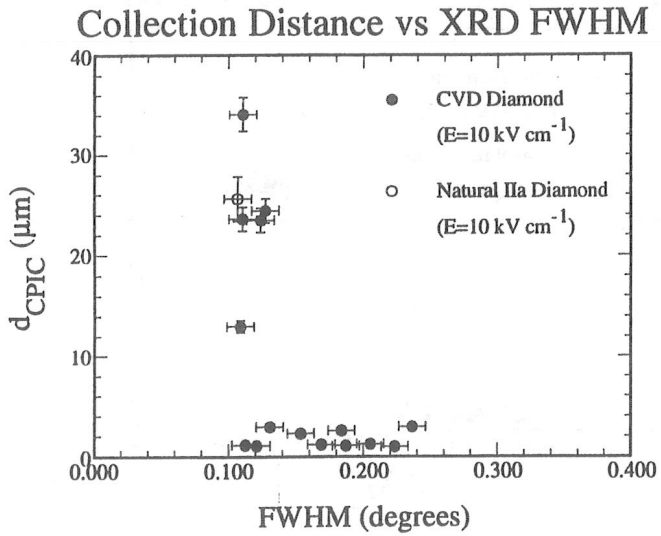

Figure 89: Correlation between collection distance and XRD peak width.

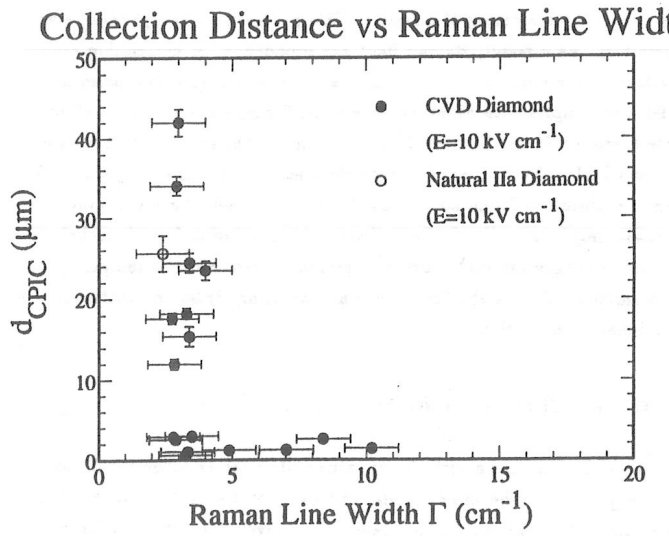

Figure 90: Correlation between collection distance at 10 kV cm^{-1} and Raman line width. Samples which exhibit broader line width have smaller collection distances.

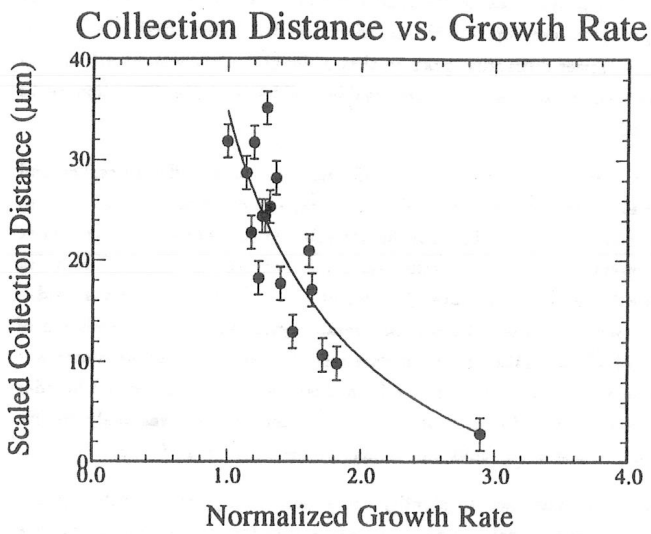

Figure 91: The correlation between collection distance and the relative film growth rate. The slower the film growth rate, the larger the collection distance. The scaled collection distance represents the collection distance at an electric field of 10 kV cm^{-1} for 400 μm thick films.

5.2 Summary of Work Performed

5.2.1 Electrical Properties

The electrical properties of polycrystalline diamond films were studied using charged particle-induced conductivity (CPIC). Accelerator test beam and radioactive source were used as the excitation sources producing charged particles with different species and energies. The signal generated by a charged particle traversing diamond provides integrated bulk information. Therefore, the collection distance measured by the CPIC technique is the average value over the bulk of the material. The results from the bulk measurements (CPIC) were compared with photo-induced conductivity (PIC) measurements which yields surface information because the electron-hole pair generation occurs near the diamond surface.

From the CPIC measurements, the excess carrier density generated by a minimum ionizing particle in both diamond and silicon was determined. These results were verified by calculations using Bethe-Bloch theory and restricted energy loss in material. Signals from polycrystalline diamond detectors were observed and the experimental results were analyzed using a detector model. The collection distance has been used to characterize the electrical property of diamond samples and the electronic performance of diamond detectors. The collection distance is associated with fundamental physical properties including carrier mobility and excess carrier lifetime.

For a comparison, the collection distance of single crystal natural type IIa diamond was studied using both the TRIUMF beam test and radioactive sources. For single crystal material, the bulk collection distance from the CPIC measurement was found to be equal to the surface collection distance from the PIC measurement. However, for polycrystalline diamond, the bulk collection distance and the surface collection distance were found to be different for all samples studied. The collection distance at the growth side of a polycrystalline diamond film is approximately twice as high as the averaged collection distance in the bulk; the collection distance at the substrate side of a film is less than 0.1 μm. This suggests that a gradient of the

electrical properties exists between the two surfaces of a diamond film. A collection distance depth profile study demonstrated the existence of a constant gradient in polycrystalline diamond film along the film growth direction. A theoretical analysis based on the rate equations for excess charge carriers in diamond also reveals the relationship between the collection distance at the surface and the integrated value in the bulk.

The collection distance of recent polycrystalline diamond films is comparable with or even larger than natural IIa diamond. Large area diamond wafers (3 cm×3 cm) were tested and good spacial uniformity was observed.

5.2.2 Material Properties

To improve the material quality of polycrystalline diamond films and to investigate the factors limiting the electronic performance of the diamond based detectors, material characterizations were performed. The experimental approaches include visual observations, electron microscopy, x-ray diffraction, Raman spectroscopy and photoluminescence.

A visual observation provides a quantatitive information of film quality using a transparency measurement. High transparency was found to be necessary for an excellent performance of a diamond detector but not a sufficient condition. Also, visual observation on the flatness of a film provides the information of the film stress which may cause the lattice deformation.

Scanning electron microscope (SEM) image provides the possibility to observe the surface of diamond samples in microscopic scale. The grain size and grain uniformity at both sides and cross section of polycrystalline films were measured and examined. A linear increase of lateral grain size with film thickness was found. This result is consistent with the cone shaped columnar grain structure along the film growth direction observed from the cross-sectional SEM experiment.

X-ray diffraction (XRD) delivers the information on lattice constant, crystal quality and crystal texturing. This measurement was classified as a surface measurement by an estimation of absorption in diamond for the x-ray used the XRD studies. At the growth side of films, (110) texturing occurs than at the substrate side indicating the growth rate of crystallites with (110) orientation is faster than others. The lattice constant was measured for both single crystal natural IIa diamond and CVD polycrystalline diamond samples. The width (FWHM) of x-ray diffraction peaks was developed to characterize material quality. High quality samples exhibit narrower diffraction peak so that a doublet x-ray wavelength can be resolved; low quality samples show unresolvable doublet since the diffraction peaks are very broad.

Laser Raman spectroscopy studies were performed to identify different carbon and impurity phases. No spectrum or band due to graphite or amorphous carbon was found in the high quality samples. The diamond line width was used to characterize the overall crystal quality. A correction was found between the Raman line width and the x-ray diffraction peak width. This result demonstrates that the peak width from both experiments characterizes the overall crystal quality. A correlation of Raman line width and lattice constant determined from XRD measurements was found. The samples with large deviation from ideal diamond lattice exhibit broader Raman line width. In addition, Raman line shape and position was analyzed. No grain size effect causing line shift and change of line shape were found.

Photoluminescence was used to identify characteristic impurity or defect levels. No radiation induced photoluminescence centers were found when polycrystalline diamond was irradiated by ^{90}Sr radioactive source. The luminescence background of polycrystalline diamond was used to characterize film quality. A correlation between Raman line width and the luminescence background level was found. A sample which shows higher luminescence background exhibits a broader Raman line.

5.3 Conclusions

During the course of this thesis work, a signal was observed for the first time from particle detectors made of polycrystalline diamond films. Signal noise ratio (S/N) has improved by a factor of three over the past two years. The collection distance for CVD polycrystalline diamond films is now exceeds natural single crystal (type IIa) diamond.

The collection distance d, a product of carrier mobility μ and carrier lifetime τ, has been used to describe the electrical properties. Charged particle-induced conductivity (CPIC) and photo-induced conductivity (PIC) have been used compared. The correlation between the bulk information measured by the CPIC technique and the information measured by the PIC technique indicates a gradient of electrical properties in all polycrystalline diamond.

Using different material characterizations, impurities and defects in natural single crystalline diamond and CVD polycrystalline diamond films have been studied. All material characterizations has been focused to correlate with the electrical property studies. Correlations have been found between crystal qualities and the characteristics of the electrical properties. From the correlation studies between collection distance and the material characterizations, we conclude that defects in the polycrystalline diamond films have significant influence on the electrical properties.

5.4 Outlook

The development of diamond based detectors for calorimetry and position sensitive detectors is underway. The prospect of the application of polycrystalline diamond films on electronic devices looks bright.

Appendix A

Classification of Diamond

- ◇ Type Ia Diamond

  Contains nitrogen as an impurity in fairly substantial amounts (of the order 0.1%), and which appears to have segregated into small aggregates. Also contains platelets associated with the nitrogen impurity. Most of natural diamonds are of this type.

- ◇ Type Ib Diamond

  Also contains nitrogen as an impurity but in dispersed substitutional form. Almost all synthetic (high temperature, high pressure) diamonds are of this type.

- ◇ Type IIa Diamond

  Contains less nitrogen impurity. Very rare in nature. These diamonds have enhanced optical and thermal properties.

- ◇ Type IIb Diamond

  A very pure type of diamond which has semiconducting properties. Generally blue in color. Extremely rare in nature. Semiconducting properties can be introduced to man-made diamond by the incorporation of boron atoms.

The classification of diamond according to both optical absorption and resistivity [16] is shown in Table 14:

Table 14: Classification of diamond.

Notation	Characteristic	Optical Transparency	Resistivity †
Ia	Aggregated Nitrogen	340 nm ~ 2.5 μm	$> 10^{15}$ Ω cm
Ib	Substitutional Nitrogen	340 nm ~ 2.5 μm	$> 10^{15}$ Ω cm
IIa	Less Nitrogen	225 nm ~ 2.5 μm	$> 10^{13}$ Ω cm
IIb	p-type semiconductor	225 nm	$10 \sim 10^{4}$ Ω cm

† Only apply in the dark since there is considerable photo-induced conductivity when ultra-violet light is present.

Appendix B

Charge Induction Process

B.1 Energy Conservation

In order to prove the relation of:

$$dQ_{\text{collected}} = \frac{Q_{\text{ionized}}}{L}\, dx \tag{B.1}$$

energy conservation was used. In a parallel plate capacitor (Figure 13), when Q_{ionized} moves a distance of dx in an electric field E, the energy which the charge has gained is equal to: $Q_{\text{ionized}} \times Edx$. This energy provided by the power supply in the external circuit to lift $dQ_{\text{collected}}$ from the negative end of the power supply to the positive end is equal to the product of the charge induced on the electrode, $dQ_{\text{collected}}$, and the voltage V. Since $V = E \times L$, we have:

$$dQ_{\text{collected}} \times L = Q_{\text{ionized}} \times dx \tag{B.2}$$

This derivation bases on an assumption that V is a constant. Because the induced charge on the electric contacts may cause a change of the potential on the contacts when Q_{ionized} moves. However, for a capacitance of 10 pF with 1 V on it, the original charge on the electric contacts is about 10^6 electrons which is much larger than $dQ_{\text{collected}}$. Therefore, the potential on the electric contacts can be approximated as a constant.

B.2 Image Method, a Diversion of Green's Theorem

When a charge q is placed at x (Figure 13), using the "image method" from the Green's theorem [21], the charge density σ on electrode at $x = 0$ is equal to:

$$\sigma(x) = \frac{q}{4\pi} \sum_{n=-\infty}^{\infty} \left\{ \frac{2nL - x}{[(2nL - x)^2 + \rho^2]^{3/2}} - \frac{2nL + x}{[(2nL + x)^2 + \rho^2]^{3/2}} \right\} \tag{B.3}$$

where ρ is the radius of the electric contact. The charge density on the other electrode from the equation can be derived by replacing x with $(L - x)$.

The total charge on the electrode is equal to:

$$\int_0^{\infty} \sigma(x)\, 2\pi\rho\, d\rho = \frac{x}{L} q \tag{B.4}$$

By using a numerical calculation, the charge induced on the electric contacts is given by:

$$Q_{\text{collected}} = \frac{x}{L} q$$

$$\text{or} \tag{B.5}$$

$$dQ_{\text{collected}} = \frac{q}{L} dx$$

Appendix C

Carrier Gradient and Current Density Divergence

C.1 Carrier Diffusion Process

In addition to the carrier drift process, another charge carrier transport process may exist. When a gradient of charge density presents, diffusion process drives charge carriers to move from the high density region to the low density region. A characteristic distance for the diffusion process is called *diffusion length* l:

$$l = \sqrt{D\tau} \tag{C.1}$$

where D is the diffusion coefficient and τ is the excess carrier lifetime. Using Einstein relation [5], the diffusion coefficient can be expressed as a function of carrier mobility μ and the absolute temperature T:

$$D = \frac{\mu k_B T}{e} \tag{C.2}$$

When a voltage, V, is applied on the electric contacts of a detector producing an electric field E, the diffusion length, l, can be written as a function of collection distance d, the contact spacing L and bias V:

$$\begin{aligned} l &= \sqrt{D\tau} \\ &= \sqrt{\frac{k_B T}{eE}}\, d \end{aligned}$$

$$= \sqrt{\left(\frac{k_B T}{eV}\right) L\, d} \tag{C.3}$$

For a bias of a few hundred volts, $\left(\frac{k_B T}{eV}\right)$ can be as small as 10^{-4}. Thus, if collection distance is equal to $\frac{L}{10}$, $l \approx 0.03\ d$. This indicates that the carrier drift process is the dominant process and the diffusion process is negligible.

C.2 Current Density Divergence

Under an electric field $\vec{E}$, the current density $\vec{J}$ consists of two parts: the drift current ($\vec{J}_{\text{drift}} = e\mu_n n\vec{E}$) and the diffusion current ($\vec{J}_{\text{diff}} = eD_n \nabla n$). Since the drift process is the dominant process in the charge transport process, the current density is given by:

$$\begin{aligned} \vec{J} &= \vec{J}_{\text{drift}} + \vec{J}_{\text{diff}} \\ &\approx e\mu_n n\vec{E} \end{aligned} \tag{C.4}$$

Recalling Eq. 2.18 in **Chapter II**, the continuity equation is equal to:

$$\frac{\partial n}{\partial t} = \frac{1}{e}\nabla \cdot \vec{J} - \frac{n}{\tau} + g(\vec{r}, t) \tag{C.5}$$

Because of a uniform excitation, the charge generation term, $g(\vec{r}, t)$, is independent of $\vec{r}$ and the charge carrier density is uniform, $\nabla n = 0$. When an isotropic material is considered, no gradient of material property occurs, $\nabla \mu = 0$. As a result, the divergence of current density does not exist, $\nabla \cdot \vec{J} = 0$. The continuity equation is reduced to:

$$\frac{\partial n}{\partial t} = -\frac{n}{\tau} + g(t) \tag{C.6}$$

In polycrystalline diamond films, a gradient of material quality exists along the columnar direction of the films, $\nabla \mu$ may not be equal to zero. The non-vanishing current divergence, $\nabla \cdot \vec{J}$, may result in an accumulation of charge in space, called the *space charge*.

C.3 Estimation of the Current Divergence

Substituting Eq. C.4 into the continuity equation Eq. C.5, the first term of the continuity equation becomes:

$$\frac{1}{e}\nabla \cdot \vec{J} \approx n\vec{E} \cdot \nabla \mu \tag{C.7}$$

Taking a polycrystalline diamond film (T826D-1) as an example, (its film thickness is 400 μm, $d^{\perp}$ is equal to 6 μm, μ is 600 $\text{cm}^2\text{V}^{-1}\text{sec}^{-1}$ and τ is 100 ps on the growth side of the film at an electric field of 10 kV cm^{-1} from the PIC measurements). The current divergence is equal to:

$$\frac{1}{e}\nabla \cdot \vec{J} \approx n\, E\, \frac{\partial \mu}{\partial x} \approx n\, E\, \frac{\Delta \mu}{\Delta x} = 1.5 \times 10^8\, n \tag{C.8}$$

Since $1/\tau$ is approximately equal to 10^{10} sec^{-1}, the current divergence becomes negligible:

$$\frac{1}{e}\nabla \cdot \vec{J} \ll \frac{n}{\tau} \tag{C.9}$$

Then, the continuity equation still yields the rate equation Eq. C.6.

Appendix D

Electric Contact Fabrication and Testing

D.1 Electric Contact Fabrication Technique

Metallic thermal evaporation technique [69] was used to fabricate electric contacts on diamond. It was performed on an evaporation stage by increasing the temperature of an evaporation tungsten filament [1] until the metal evaporated. Thus, the diamond film mounted near the source filament was covered by a thin film of the evaporating metal. A metallic shadow mask was used in contact with the diamond film to define the shape and dimension of the contact. The thickness of the depositing layer was measured by a thickness monitor [2]. A chromium layer was deposited first, and followed by a layer of gold to protect chromium from being oxidized. Also, care was taken to align the contacts on either side of the film.

Annealing process in nitrogen gas atmosphere at 600°K was performed after the deposition. The evaporation and annealing conditions are listed in Table 15. The predeposition cleaning procedures are listed in Table 16.

[1] Alumina coated evaporation source boat was used for gold evaporation to prevent from the formation of alloy with tungsten.

[2] Maxtex TM-100 thickness monitor.

Table 15: Electric contact fabrication procedures.

	Cr	Au
Vacuum (torr)	6×10^{-6}	8×10^{-6}
Current (A)	120	30
Deposition Rate ($Åsec^{-1}$)	$1 \sim 5$	$5 \sim 10$
Thickness (Å)	~ 500	~ 3000
Annealing	600°C, 20 minutes in N_2	

Table 16: Pre-deposition cleaning procedures. Each step uses fresh solution.

Procedure	Solution	Action
Step 1	$H_2O_2 : NH_4OH = 1 : 1$	70°C, 2 minutes
Step 2	Deionized water	Ultrasonic bath, 5 minutes
Step 3	Deionized water	Ultrasonic bath, 5 minutes
Step 4	Acetone	Ultrasonic bath, 5 minutes
Step 5	Acetone	Ultrasonic bath, 5 minutes
Step 6	Methanol	Ultrasonic bath, 5 minutes
Step 7	Methanol	Ultrasonic bath, 5 minutes
Step 8	Deionized water	Ultrasonic bath, 5 minutes
Step 9	—	Bake, 175°C, 15 minutes

D.2 Electric Contact Testing

Current-voltage (I-V) measurements (Figure 92) were performed to verify the linearity of I-V dependence. A symmetric I-V characteristic for different bias polarity indicates the similarity of the two contacts. A linear I-V behavior manifests that both contacts are of ohmic since one rectifying type contact may give the diamond detector a non-linear I-V characteristic.

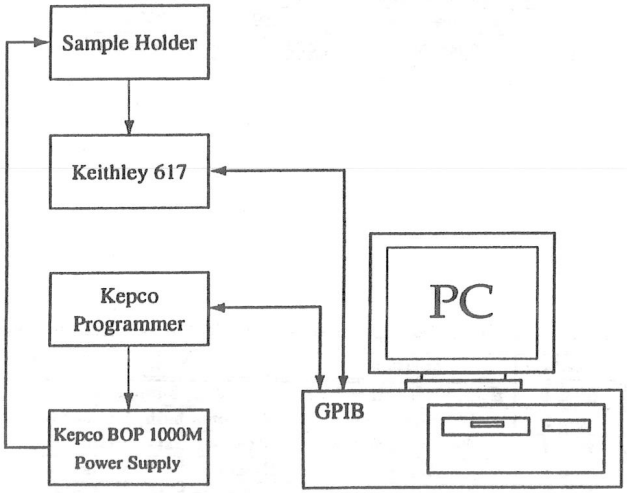

Figure 92: Current-voltage measurement setup.

Bibliography

[1] C. Kittel, *"Introduction to Solid State Physics"*, John Wiley & Sons, Inc. (1986).

[2] C. D. Clark, P. J. Dean, and P. V. Harris, Proc. Royal Soc. London, A277, 312 (1964).

[3] R. A. Roberts and W. C. Walker, Phys. Rev., 161, 730 (1967).

[4] G. S. Painter, D. E. Ellis, and A. R. Lubinsky, Phys. Rev., B4, 3610 (1971).

[5] N. W. Ashcroft and N. D. Mermin, *"State Physics"*, Saunders College – Philadelphia (1976).

[6] R.B. Leighton, *"Principles of Modern Physics"*, McGraw-Hill Book Company, 485 (1959).

[7] S. Wang, *"Fundamentals of Semiconductor Theory and Device Physics"*, Prentice Hall Series in Electrical and Computer Engineering, series edited by L. O. Chua (1989).

[8] F. J. Morin and J. P. Maita, Phys. Rev., 94, 1525 (1954).

[9] L. S. Pan, D. R. Kania, P. Pianatta, and O. L. Landen, Appl. Phys. Lett., 57, 623 (1990).

[10] F. Nava, C. Canali, C. Jacoboni, and L. Reggianni, Solid State Commun., 33, 475 (1980).

[11] B. G. Streetman, *"Solid State Electronic Device"*, Prentice-hall, Inc, 155 (1980).

[12] W. van Roosbroeck and W. Shockley, Phys. Rev., 94, 1558 (1954).

[13] V. S. Valvilov, J. Phys. Chem. Solids, 8, 223 (1959).

[14] S. M. Ryvkin, *"Photoelectric Effects in Semiconductors"*, Consultants Bureau, New York (1964).

[15] P. K. Bachmann, D. Leers, and H. Lydtin, Diamond and Related Materials, 1, 1 (1991).

[16] Drukker International, *"Properties of Diamond"*, Amsterdam 1001MC, Holland, reprinted by courtesy of De Beers Industrial Diamond Division (1992).

[17] Industrial Diamond Review, **50-52** (1992).

[18] M. A. Kumakhov and F. F. Komarov, *"Energy Loss and Ion Ranges in Solid"*, Goldon and Breach Science Publishers (1981).

[19] R. Fernow, *"Introduction to Experimental Particle Physics"*, Cambridge University Press (1986).

[20] S. P. Ahlen, Rev. of Mod. Phys., **52**, 121 (1980).

[21] J. D. Jackson *"Classical Electrodynamics"*, John Wiley & Sons, Inc. (1974).

[22] H. Bethe and J. Ashkin, *"Experimental Nuclear Physics"*, edited by E. Segre, **1**, part 2, New York Wiley (1959).

[23] U. Fano, Ann. Rev. Nucl. Sci., **13**, 1 (1963)

[24] A. Yariv, *"Quantim Electronics"*, John Wiley & Sons, Inc. – New York (1975).

[25] J. F. H. Custers and F. A. Raal, Nature, **179**, 268 (1957).

[26] H. R. Philipp and E. A. Taft, Phys. Rev., **136**, A1445 (1964).

[27] D. R. Kania, L. S. Pan, P. Bell, O. L. Landen, H. Kornblum, P. Pianetta, and M. D. Perry, J. Appl. Phys., **68**, 124 (1990).

[28] *Particle Properties Data Booklet*, Particle Data Group, 121, North-Holland (1990).

[29] W. Shockley, Czech. J. Phys., **B11**, 81 (1961).

[30] V. S. Vavilov, J. Phys. Chem. Solids, **8**, 223 (1959).

[31] C. Canali, E. Gatti, S. F. Kozlov, P. F. Manfredi, C. Manfredotti, F. Nava, and A. Quirini, Nucl. Instrum. Meth., **160**, 73 (1979).

[32] R. W. Williams, *"Methods of Experimental Physics"*, **5A**, edited by L. C. L. Yuan, Academic Press, 89 (1961).

[33] S. Ramo, Proc. of I. R. E., **27**, 584 (1939).

[34] O. D. Kellogg, *"Foundations of Potential Theory"*, Berlin Verlag Von Julis Springer, 231 (1929).

[35] L. S. Pan, *"Photoconductivity Measurements"*, Diamond Detector Meeting, Columbus, Ohio, September 20 (1991).

[36] C. H. Braden, L. Slack, and F. B. Shull, Phys. Rev. **75**, 1964 (1964).

[37] T. Taniguchi, Y. Fukushima, and Y. Yoribayashi, IEEE Transaction on Nuclear Science, **NS-36**, 657 (1989).

[38] *"DIAMAS Experimental Logbook"*, TRIUMF, 1, 124 (1991).

[39] *"DIAMAS Experimental Logbook"*, KEK, November, (1990).

[40] L. S. Pan *et al.*, J. Appl. Phys., **74**, 1086 (1993).

[41] M. A. Plano, S. Zhao *et al.*, Appl. Phys. Lett., **64**, 193 (1994).

[42] J. W. S. Hearle, J. T. Sparrow, and P. M. Cross, *"The Use of the Scanning Electron Microscope"*, Pergamon Press (1972).

[43] JCPD, *"Powder Diffraction File for Inorganic Phases*, 6-675, International Centre for Diffraction Data (1989).

[44] L. V. Azároff, *"Elements of X-ray Crystallography"*, McGraw-Hill (1968).

[45] B. L. Henke *et al.*, Atomic Data and Nucl. Data Table, **27**, 27 (1982).

[46] C. G. Darwin, Phil. Mag., **43**, 800 (1922).

[47] G. H. Stout and L. H. Jensen, *"X-ray Structural Determination"*, John Wiley & Sons, Inc. (1989).

[48] W. H. Zachariasen, Acta Cryst., **23**, 558 (1967).

[49] B. E. Warren, *"X-ray Diffraction"*, Addison-Wesley Publishing Company, (1969).

[50] B. D. Cullity, *"Elements of X-ray Diffraction"*, Addison-Wesley Publishing Company (1978).

[51] R. J. Nemanich, S. A. Solin, and R. M. Martin, Phys. Rev., **B23**, 6348 (1981).

[52] A. Smekal, Nature, **11**, 873 (1923).

[53] C. V. Raman, Nature, **121**, 619 (1928).

[54] C. V. Raman and K. S. Krishnan, Nature, **121**, 501 (1928).

[55] C. V. Raman and K. S. Krishnan, Proc. Royal Soc. London, **122A**, 23 (1928).

[56] S. A. Solin, Phys. Rev., **B1**, 1687 (1970).

[57] A. Badzian and T. Badzian, Mat. Res. Bull, **23**, 531 (1988).

[58] K. Sinha, J. Menéndez, W. J. Varhue, and B. S. Shinseki, *"Raman Scattering, Luminescence and Spectroscopic Instrumentation in Technology"*, edited by F. Adar, SPIE Proceedings, **1055**, 170 (1989).

[59] M. Yoshikawa, G. Katagiri, H. Ishida, A. Ishitani, M. Ono, and K. Matsumura, Appl. Phys. Lett., **55**, 2608 (1989).

[60] J. G. Grasselli and B. J. Bulkin, *"Analytical Raman Spectroscopy"*, John Wiley & Sons, Inc. (1987).

[61] I. H. Cambell and P. M. Fauchet, Solid State Commun., **58**, 739 (1986).

[62] T. A. Perry and C. P. Beetz, Jr., *"Raman Scattering, Luminescence and Spectroscopic Instrumentation in Technology"*, edited by F. Adar, SPIE Proceedings, **1055**, 152 (1989).

[63] C. D. Clark, R. W. Ditchburn and H. B. Dyer, Proc. Royal Soc. London, **A234**, 363, (1956).

[64] C. D. Clark, R. W. Ditchburn and H. B. Dyer, Proc. Royal Soc. London, **A237**, 75 (1956).

[65] J. C. Ager, III, *"Imaging Raman and Photoluminecence Characterization of Natural and CVD Diamond Based High Energy Detectors"*, Diamond Detector Workshop, San Ramon, California, April 14-15 (1992)

[66] J. Walker, Rep. Prog. Phys., **42**, 108 (1979).

[67] D. S. Knight and W. B. White, *"Raman Scattering, Luminescence and Spectroscopic Instrumentation in Technology"*, edited by F. Adar, SPIE Proceedings, **1055**, 144 (1989).

[68] L. A. Turk and P. G. Klements, Phys. Rev., **B9**, 4422 (1974).

[69] R. C. Jaeger, *"Introduction to Microelectronic Fabrication*, modular series on *Solid State Devices* edited by G. W. Neudeck and R. F. Pierret, Addison-Wesley Publishing Company (1988).